FFI Forsvarets forskningsinstitutt

21/00388

FFI-RAPPORT

Thermal sensor acquisition range estimation

Steinar Børve

Thermal sensor acquisition range estimation

Steinar Børve

Norwegian Defence Research Establishment (FFI) 24 June 2021

Keywords
Termiske sensorer
signatur
deteksjon
elektromagnetiske bølger

FFI report
21/00388

Project number
1580

Electronic ISBN
978-82-464-3329-5

Approvers
Halvor Ajer, *Director of Research*
Morten Huseby, *Research Manager*

The document is electronically approved and therefore has no handwritten signature.

Copyright

(U) Summary

There is a large number of factors which may influence the performance of thermal surveillance systems used in any given scenario. Some of the parameters needed for making an accurate performance prediction might be known, but many more are typically unknown or must be loosely guessed based on past experiences and information about similar systems and comparable situations. It is hardly realistic that operators will have access to a comprehensive list of parameters nor the numerical tools required to perform accurate predictions of the effective detection range during real-world operations. Simpler range estimation methods might be needed and rough guesses of system and environmental parameters might be necessary in order to get a reasonably good sense of the effective range of thermal sensors in operational settings.

This report gives an introduction to the topic of thermal acquisition range estimation. It describes two common methods for performing calculations of this kind. The first method is formulated by a very simple equation but only considers target size and the most basic sensor properties. The second method, as formulated in STANAG 4347, is originally a non-linear equation which is commonly solved geometrically. This makes the method less suited for quick and automated estimation. Therefore, this report proposes a new, parametric second-order algorithm based on the STANAG 4347 method, where range can be estimated with model uncertainties easily being taken into account.

To illustrate the use of the new algorithm, this report provides numerical examples relevant to the Norwegian Armed Forces. We look at 8 different thermal camera setups, ranging from low-weight binoculars to relatively large, vehicle-mounted systems. Since the second method takes into account atmospheric attenuation, a separate model for estimating the extinction coefficient for different climatic conditions has also been developed. The model is described in some detail. In addition, extensive tables are provided which list the extension coefficient calculated for a wide range of different weather and climate scenarios. In practical use, the idea is that an operator will have access to the tables rather than the full atmospheric model.

(U) Sammendrag

Det er mange faktorer som kan være med på å bestemme ytelsen til termiske overvåkningssystemer brukt i bestemte scenarioer. Noen av parametrene som trengs for å utføre nøyaktige prediksjoner om ytelse, vil kunne være kjent. Langt flere parametre vil likevel typisk være ukjent eller må løselig anslås basert på erfaringer og informasjon om lignende systemer og sammenlignbare situasjoner. Det er lite realistisk at operatører vil ha tilgang til fullstendige parameterlister eller de numeriske verktøy som trengs for å kunne gjennomføre nøyaktige prediksjoner av effektiv deteksjonsrekkevidde under realistiske scenarioer. Enklere metoder for overslag av rekkevidde basert på omtrentlige antagelser om system- og miljøparametre kan utgjøre nødvendige verktøy for å oppnå en god forståelse av effektiv sensorrekkevidde i en operasjonell situasjon.

Denne rapporten gir en innføring i temaet termisk rekkeviddeestimering. Den beskriver to metoder som er i vanlig bruk ved estimering av rekkevidden til termiske kameraer. Den første metoden kan uttrykkes gjennom en enkel ligning, men tar kun hensyn til målets størrelse og de mest grunnleggende sensoregenskapene. Den andre metoden, slik den er formulert i STANAG 4347, er opprinnelig en ikke-lineær ligning som vanligvis blir løst geometrisk. Dette gjør metoden mindre egnet til raske og automatiserte estimater. Av den grunn, blir det i denne rapporten foreslått en ny parametrisk, andre-ordens algoritme basert på metoden fra STANAG 4347, der sensorrekkevidde estimeres på en slik måte at modellusikkerheter enkelt kan tas med i betraktning.

For å illustrere bruken av den nye algoritmen gir rapporten numeriske eksempler relevante for det norske Forsvaret. Vi tar for oss 8 ulike termiske kameraoppsett, fra lette kikkerter til større, kjøretøymonterte systemer. Siden den andre beregningsmetoden tar hensyn til atmosfærisk dempning, har også en separat modell for utregning av dempningskoeffisient ved ulike klimatiske forhold blitt utviklet. Denne modellen er relativt detaljert beskrevet i rapporten. I tillegg er det utarbeidet omfattende tabeller som lister opp dempningskoeffisienten ved et stort spekter av ulike vær- og klimatyper. I praktisk bruk er tanken at en operatør vil ha tilgang til disse tabellene heller enn den fullstendige atmosfæriske modellen.

Contents

Appendix

1 Introduction

Target acquisition, the detection, identification, and location of a target, is an essential part of any military operation. For this reason, it is of vital importance to have a realistic view of the capabilities of the electro-optical equipment involved in a given scenario. Often, this boils down to answering the questions:

- How far can we/the enemy see?
- What will we/the enemy be able to see/detect on a given distance?

There are many factors that play a role in determining the range capability of a camera. Some of these factors are of course determined by the technical specifications of the camera in question, such as the focal length, the view angle, the pixel pitch, resolution and noise level. It is also quite obvious that the range capability will be affected by weather and atmospheric conditions (e.g. atmospheric turbulence, humidity, rain, fog, or snow). In addition to this, the characteristics of the observed scene should be taken into account. The first of the two posed questions logically requires an answer which only provides information about a specific distance. It does not consider the scene at all. The latter question, at least expects an answer which specifies a target (with a known size and shape) at a specific distance. Still, this is only a small fraction of the information that characterises a scene. What is the contrast between a potential target and the background? Is the target moving or is it static? What is the orientation of the target? Is the target partially covered by other constituents of the scene (for instance vegetation). These are all examples of relevant questions regarding the scene which might affect the detectability of a specific target at a given distance. And last but not least, detection is not made by the camera itself and isolated from any tactical scenario. There must be a human operator or an automatic detection software (virtual operator) which makes the actual detection based on the images captured by the camera. How well a system performs will inevitably depend on the properties of this operator, whether the aim is to *detect*, *recognise*, or *identify* the target, and in the case of a human operator, how the physical and mental state of the operator is at time of observation.

1.1 The electromagnetic spectrum

Camera properties will also depend strongly on what part of the electromagnetic spectrum the sensors are designed to detect. We have all seen the x-ray images which expose bone structures buried underneath a layer of tissue. In contrast, cameras based on reflected ultraviolet light can reveal surface features not detectable in other parts of the spectrum. Cameras sensitive to visible light (corresponding to wavelength range of $0.4 - 0.7\mu$m) is obviously the most common. Apart from reproducing what we can observe with the naked eye, they benefit from what is normally a fairly high atmospheric transmission rate in this part of the spectrum. But sensors operating in visible or near-infrared (corresponding to wavelength range of $0.7 - 1.4\mu$m) light, depend on reflected light to detect the surroundings. This limits the use to scenarios where a proper light source is available, either natural (e.g. daylight or moonlight) or artificial (e.g. streetlights or IR light source). Thermal sensors on the other hand, utilise the fact that any object with a temperature above absolute zero emits electromagnetic radiation. The reason why this radiation cannot be utilised by cameras operating in the visible and near-infrared sections of the spectrum, is easily explained from physics.

First, we assume that the radiation can be described sufficiently accurate using the black-body approximation, which means that the radiation spectrum is only dependent on the surface temperature. According to **Planck's law**, the spectral radiance as a function of the wavelength, λ, from a black-body with a temperature T (in units of Kelvin) is given as

$$B(\lambda, T) = \frac{2hc^2}{\lambda^5}\frac{1}{\exp(\frac{hc}{\lambda kT}) - 1}, \tag{1.1}$$

where $h = 6.626 \cdot 10^{-34}$ Js is the Planck constant, $k = 1.38 \cdot 10^{-23}$ J/K is the Boltzmann constant and c is the speed of light (which is $3.00 \cdot 10^8$ in vacuum). The total radiated power from the black-body is obtained by integrating over all wavelengths. **Stefan-Boltzmann's law** is given as

$$P = \sigma T^4, \tag{1.2}$$

where the Stefan-Boltzmann constant, σ, equals roughly $5.67 \cdot 10^{-8}$ $\mathrm{Js^{-1}m^{-2}K^{-4}}$, and shows the strong temperature-dependence of the radiated power. By taking the derivative of Eq. 1.1 rather than integrating the function, we obtain what is known as **Wien's displacement law** which states that the peak spectral radiance is located at a wavelength, λ_m, inversely proportional to the temperature as

$$\lambda_m = \frac{b}{T}, \tag{1.3}$$

where Wien's displacement constant, b, equals roughly $2900 \mu\mathrm{m} \cdot \mathrm{K}$.

John W. Draper in 1847 concluded that most solid materials start emitting light visible to the human eye once the temperature rise above roughly 800 K. This has since been known as the **Draper point**. For temperatures closer to typical ambient temperature levels, most thermal radiation is emitted in the range 3-20 μm. Fig. 1.1 shows the spectral radiance as a function of wavelength from a black-body with a temperature equal to 200 K (red), 300 K (green), 400 K (turquoise), 500 K (blue), and 600 K (black). We see that thermal radiation from an object with a temperature of around 300 K is best picked up by a camera operating in the mid-wave infrared (MWIR) range of 3-8 μm or the long-wave infrared (LWIR) range of 8-20 μm. When nothing else is specified, we will in this report limit the discussion to electromagnetic waves in the MWIR and LWIR ranges when we use the term **thermal radiation**. Due to atmospheric absorption, the practical operating ranges for thermal cameras are reduced to 3-4 μm (MWIR) and 8-14 μm (LWIR).

1.2 Emissivity (ε)

A black-body represents an ideal, upper limit to the thermal radiance from an object, and for some materials the deviation from the black-body spectrum is substantial. The ratio of the thermal radiation from a material surface and a black-body surface at a given wavelength, is known as the *emissivity*, denoted $\varepsilon(\lambda)$[1], and the material surface radiance is then given as

$$L(\lambda, T) = \varepsilon(\lambda) B(\lambda, T), \tag{1.4}$$

where $B(\lambda, T)$ is the black-body radiance given in Eq. 1.1. If $0 < \varepsilon < 1$ is independent of wavelength, we have what is known as a *grey-body*. This again is only an approximation to real materials, but useful when considering sensor's operating in a relatively small interval of the

---

[1] In the current context, we neglect the small, but non-zero temperature-dependence of ε.

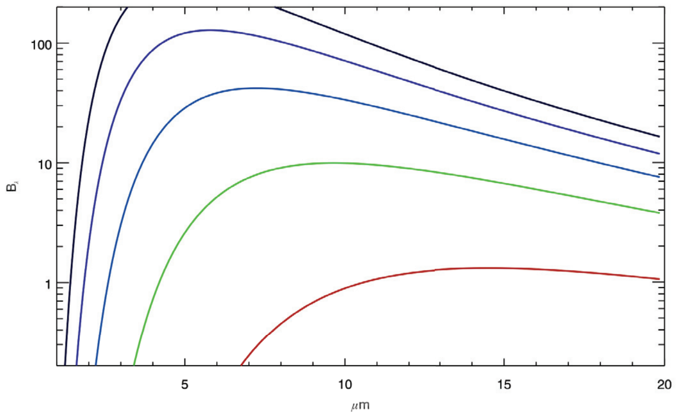

Figure 1.1 Spectral radiance (in units of $W/m^2\mu m$) as a function of wavelength (in units of μm) from a black-body with a temperature equal to 200 K (red), 300 K (green), 400 K (turquoise), 500 K (blue), and 600 K (black).

spectrum. Polished metals have often very low emissivity (< 0.1) while organic materials, soil and water typically has emissivity close to or above 0.9 (Brewster, 1992). If we combine Eqs. 1.1, 1.3, and 1.4, we find that the peak radiance, L_m, from a material surface with temperature T is

$$L_m = \varepsilon(\lambda_m)B(\lambda_m, T) \equiv C\varepsilon_m T^5, \tag{1.5}$$

where C is merely a constant. The thermal sensors under consideration in this work measures the thermal radiation coming from a surface in a spectral interval close to the radiance peak for most relevant temperatures. And since sensors typically assume the radiation to be that of a black-body ($\varepsilon = 1$), an emissivity smaller than 1 will usually cause the sensor to underestimate the temperature. The apparent or measured temperature, T_a, would then become

$$T_a = \varepsilon^{1/5} T. \tag{1.6}$$

Note that temperature, as always, must be given in Kelvin and that we here refer to wavelength-averaged emissivity for the material. As an example: if the surface temperature is 50 °C and the emissivity is 0.61, a sensor will most likely measure the surface temperature to be around 20 °C. Also, this expression for the difference between the true and measured surface temperature does not include atmospheric attenuation, which also can affect the measured temperature. This is described in more detail in section 5.

1.3 Report structure

The fact that thermal sensors can operate without an external light source, makes them particularly interesting from a target acquisition point-of-view. But the distinct differences between infrared and visible radiation, both when it comes to emission and atmospheric absorption, make it even more challenging to assess the effective range of a thermal camera system compared to a system based on visible light. Although there are many works found in the literature that discuss the effectiveness of thermal sensor systems (Borcan & Spulber, 2013; Chrzanowski, 2010; Howe, 1993; Johnson, 1958;

Perić et al., 2019), we thought it useful to write a review of two of the simpler methods available for producing range estimates. Based on the second method, described in STANAG 4347 (NATO STANAG 4347, 1995), we propose a new parametric range estimate algorithm. In addition, this report provides examples where the two methods are applied to scenarios relevant to the Norwegian Armed Forces, both in terms of sensor systems and in terms of weather conditions.

First, we define in section 2 some basic concepts helpful in the following discussions, as well as a description of the specific camera systems to be used as examples in section 3. Then in section 4, we go through the simpler of the two methods for estimating the range of thermal camera, the **Pixels-on-target** method. Section 5 gives a necessary introduction to atmospheric attenuation before we in section 6 can focus on the main part of this work, **MRTD-based** range estimation. Section 7 provides practical examples where the two methods are compared. Finally, in section 8, we make some conclusive remarks about the usefulness of each method. Appendix A gives a detailed description of the model used for calculating the atmospheric extinction coefficient, while Appendix B provides tables of ready-to-use extinction coefficients for a wide selection of weather and climatic conditions calculated using the extinction model.

2 Camera-enabled target acquisition concepts

Before we start discussing specific methods to estimate the effective range of thermal cameras, we need to introduce some fundamental concepts related to camera-based target acquisition. First, we go through some basic properties of cameras, before introducing the **Johnson Criteria**.

2.1 Basic camera properties

In order to make any meaningful comparison of different camera systems, we need to know a minimum of parameters for the systems in question. Some parameters are coupled, so that unknown parameters can in some cases be calculated on the basis of known parameters. We will make a few assumptions in order to simplify the equations that describe the relation between these parameters. Fig. 2.1 illustrates some of the optical parameters assuming **the thin lens approximation** which states that the thickness of the lens is negligible to the radii of the lens surfaces. In the sketch, we have indicated **the sensor width** (d), **the field of view** (α), **the focal length** (f), **the image distance** (R), and **the image width** (D).

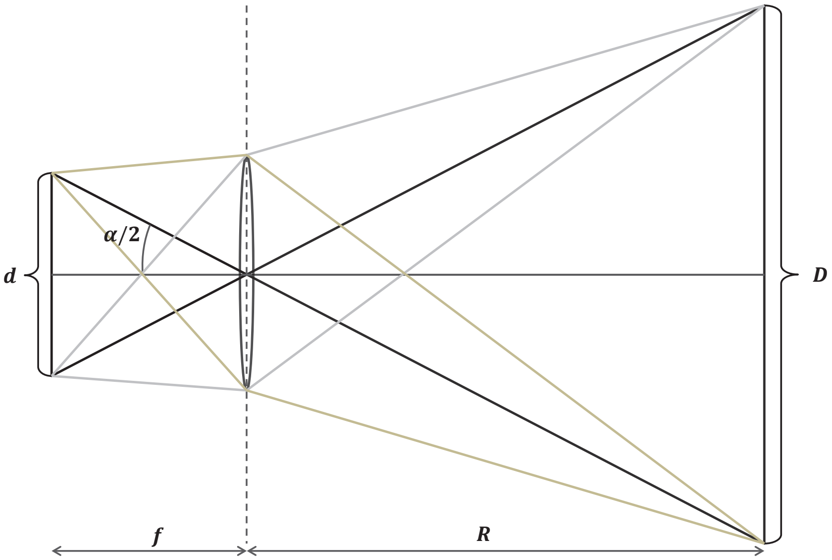

Figure 2.1 Sketch of a camera lens according to the thin lens approximation with annotations indicating the sensor width (d), the field of view (α), the focal length (f), the image distance (R), and the image width (D).

The sensor width, d, is related to α and f by the simple trigonometric expression

$$d = 2f \tan\frac{\alpha}{2}. \tag{2.1}$$

Due to geometric similarity, we also have that

$$D = \frac{dR}{f}. \tag{2.2}$$

To simplify Eq. 2.1, we can assume **the small-angle approximation** which states that for sufficient small angles θ given in radians, $\tan\theta \approx \theta$. The error in applying this approximation is roughly 0.25%, 1.0%, and 1.6% when θ equals 10°, 20°, and 25°, respectively. Applying the small-angle approximation gives us the following simple relation between d, f, and α (in radians):

$$d = f\alpha. \tag{2.3}$$

Since the sensors are digital, we have to consider **the pixel size** of the sensor in question, denoted by $N_x \times N_y$. The pixel pitch (δ) of the sensor is the spatial distance, center-to-center, between adjacent pixels and is typically given in micrometer (μm). Let $N \equiv N_x$, the pixel pitch is then given as

$$\delta = \frac{d}{N}. \tag{2.4}$$

Each pixel is said to have a certain field of view, so-called **instantaneous field of view** (IFOV), which will be denoted by ϵ and can be expressed as

$$\epsilon = \frac{\delta}{f}. \tag{2.5}$$

If, as often is the case, δ is given in units of μm and f in units of mm, we get ϵ in units of milliradians (mrad). By eliminating f using Eq. 2.3 and δ using Eq. 2.4, we can also express ϵ simply as

$$\epsilon = \frac{\alpha}{N}. \tag{2.6}$$

Hence we see that:

- ϵ decreases when the number of pixels (N) increases.
- ϵ decreases with reduced field of view (ϵ).
- Lower ϵ means higher increased target resolution i.e. higher “camera performance”.

In short, camera performance will increase when the number of pixels increases or the field of view is reduced (or both).

2.2 The Nyquist frequency

The Nyquist frequency is a concept originally introduced in electrical engineering but which has an equally important role in other discrete signal processing systems. The quantity, which in this report will be deonted by ν_N, can in general terms be defined as half the sampling rate of the discrete signal. In the context of image processing the signal is spatial rather than temporal and the sampling rate is the inverse of the instantaneous field of view, which means that the Nyquist frequency can be expressed as

$$\nu_N = \frac{1}{2\epsilon}. \tag{2.7}$$

To illustrate the importance of the Nyquist frequency, we first look at the most obvious example, a discretised sinusoidal wave. In Fig. 2.2 we see two periods of a continuous sinusoidal wave, drawn with black, solid lines. The wave is here reproduced with two different sampling rates where the discrete signals are indicated by the red, dashed lines. On the left hand side (panel **a**), the sampling rate is 14 times the wave frequency, which corresponds to 7 times the Nyquist frequency. On the right hand side (panel **b**), the sampling rate is exactly equal to the Nyquist frequency. Above the wave curves, we also see the discrete signals visualised as greyscale images. We see how the higher sampling rate gives a better approximation to the original wave shape and much more accurate amplitude. At the Nyquist frequency, the signal just switches between two values. Still, the correct signal frequency is maintained. If we were to decrease the sampling rate below the Nyquist frequency, however, we would not be able to reproduce the correct signal frequency. We would then experience the effect known as *aliasing*. In addition, the amplitude of the discrete signal would decrease until the sampling rate is equal to the continuous wave frequency. At which point, the discrete amplitude becomes exactly zero.

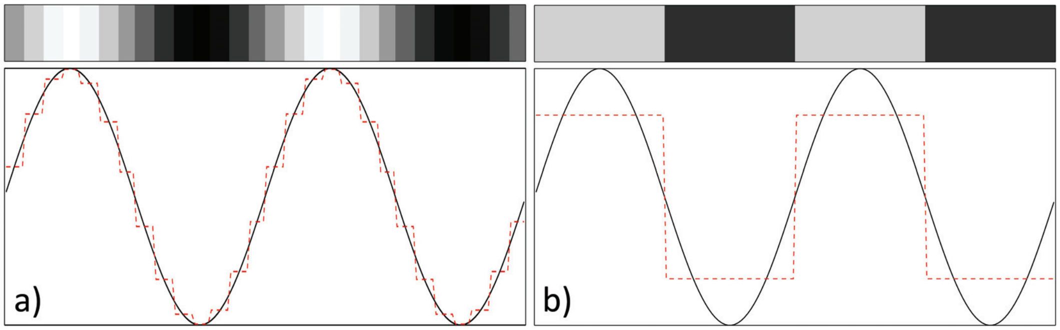

*Figure 2.2 Continous sinusoidal wave (black solid lines) reproduced discretely (red dashed lines) with a samling rate of 14 (**a**) and 2 (**b**) times the wave frequency. The latter sampling rate corresponds to the Nyquist frequency. The discrete signals are also visualised as grayscale images.*

Often, the relevant continuous signal is nowhere near a sinusoidal. Still, the concept of the Nyquist frequency is important. An example more relevant to the analysis of spatial images, is shown in Fig. 2.3. The figure combines 4 small images where each image in turn shows a series of 4 snapshots of a bright square object moving from the lower left to the upper right corner. Superimposed on the images, one can discern a blue grid which indicates the pixel size in each image. Looking at either the start or end position of the bright squares, we see that the size of the square is 4×4 pixels (panel **a**), 2×2 pixels (panel **b**), 1×1 pixels (panel **c**) and 0.5×0.5 pixels (panel **d**). For each snapshot (within each image), the true size of the objects is also indicated by a green, open square.

The start and end orientations and positions of the square objects were chosen to give optimal representations on the discrete grid. This means that the object edges were aligned with the grid cell edges for the first and last snapshots. For the two intermediate snapshots in each image, such alignment is not achieved. As a consequence, a certain level of smearing occurs. In panel **a**, the 4×4 square affects a 5×5 region in the intermediate snapshots. Also, the edge brightness appears to be reduced relative to the true brightness exhibited in the start and end snapshots. When the object size is reduced to 2×2, we see from panel **b** that the apparent object size is changed to 2×3 in the intermediate snapshots, where the true brightness is reproduced in less than half this area. We are not dealing with a periodic signal in this case, but if we did, panel **c** would correspond to the Nyquist frequency. Here the bright square object has the same size as a pixel. Because of the optimised start and end positions, the object is perfectly reproduced in the first and last snapshots. In the intermediate snapshots however, the radiation from the object is spread out in 2×2 regions, 4 times its true size. The brightness is reduced accordingly. In the last image, panel **d**, the object

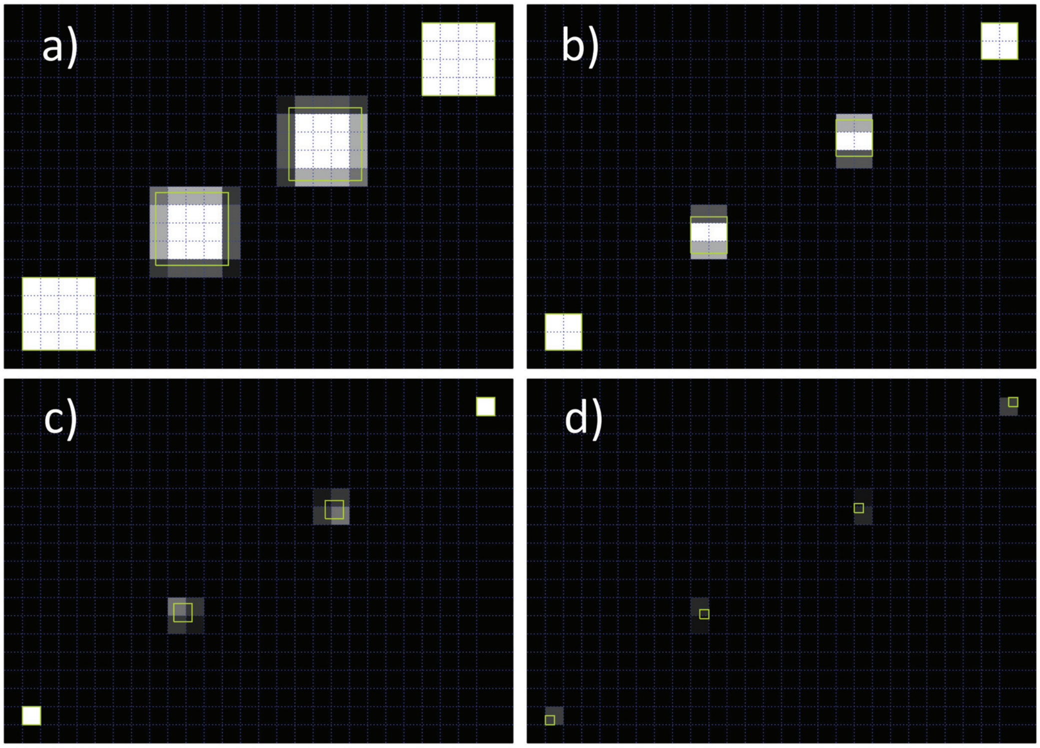

Figure 2.3 *Four snapshots of four bright squares moving from lower left to upper right. The size of the squares are* 4×4 *pixels (panel* **a***),* 2×2 *pixels (panel* **b***),* 1×1 *pixels (panel* **c***) and* 0.5×0.5 *pixels (panel* **d***). The pixel size is indicated by the blue grid superimposed on the images, and the true object size in each image is shown by the green, open squares.*

is only half a pixel wide. This means that even at the start and end positions, the size will be overestimated and the brightness underestimated. If the true brightness of the object is sufficiently large, the object might still be detected, but this will be increasingly hard if the object-to-grid size ratio is decreased further.

2.3 The Johnson Criteria concept

In the late 1950's, John Johnson of the US Army Night Vision and Electronic Sensors Directorate proposed an important method designed to determine the resolution needed for an operator to obtain a specified level of information about a given target with a certain statistical success rate (Johnson, 1958). Three distinct tasks or levels of information collection were formulated. The simplest task, **detection**, is the act of determining that a (possible) target is located in the scene. The intermediate level task is to **recognise** which class the target belongs to; whether it is a person, a vehicle, or something else. Finally, the task of **identification** requires the operator to be able to separate this particular target from other targets of the same class (e.g. type of animal, distinguish armed forces personnel from civilians, or class of vehicle).

Task	P = 50%	P = 70%	P = 90%	Uncertainty
Detection	1.00	1.25	1.75	±0.25
Recognition	4.0	5.2	7.2	±0.8
Identification	6.4	8.3	11.5	±1.5

Table 2.1 Number of bar cycles required across a target's critical dimension for each of the three main discrimination tasks (detection, recognititon and identification) with success rates of 50%, 70%, and 90% and an uncertainty given by the last coloumn (Howe, 1993).

Johnson claimed that for the purpose of determining resolution requirements any target could be replaced by an **equivalent target**, a square with sides equal to what is known as the **critical dimension** of the target. The critical dimension according to the Jonhson Criteria should be the geometric mean of the target height and width. Others use the height as the critical dimension (Howe, 1993), or something closer to the minimum of the two (FLIR Systems Inc., 2019). Johnson's point was that the probability of successful task accomplishment correlates with the number of bars in a target bar pattern which is resolvable across the equivalent target. It also depends on the acquisition task in question. The optical contrast between target and background, which obviously plays a role in target acquisition, is not considered by the Johnson Criteria.

The target bar pattern consists of alternating bright and dark bars, either horizontally or vertically orientated. Each bar is one pixel wide meaning that a bar cycle, a single pair of a bright and a dark bar, is two pixels wide. With increased resolution (or decreased target distance), the number of bar cycles fitting across the critical dimension of a target increases as well. The number of bar cycles required in order to obtain a certain success rate for a given task, will vary according to which publication you refer to. Table 2.1 lists numbers according to Howe (1993). Each row focuses on one of the three specified tasks, detection, recognition, or identification. Columns 2 to 4 give the number of bar cycles required within the target critical dimension to obtain a success rate of 50%, 70%, and 90%, respectively. The last column indicates the level of uncertainty associated with the bar cycle count for that specific task.

In practice, it is useful to express the Johnson Criteria as a **pixels-per-meter** ($\mathrm{n}_{\mathrm{ppm}}$) requirement at the target distance. Mathematically this requirement can be formulated as

$$\mathrm{n}_{\mathrm{ppm}} = \frac{2J_{\mathrm{bcc}}}{L}, \tag{2.8}$$

where J_{bcc} is the Johnson bar cycle criteria and L is the critical dimension of the target. The inverse of $\mathrm{n}_{\mathrm{ppm}}$ tells us how many meters per pixels we can accept at the target distance if we are to meet the Johnson Criteria.

2.3.1 The Johnson Criteria applied to concrete examples

Often, only the required bar cycle numbers at 50% success rate (denoted by N50 and listed in coloumn 2 of Table 2.1) will be listed. The bar cycle numbers at any other success rate (between 0 and 1) will be given by what is known as the **target transform probability function (TTPF)**. The TTPF is plotted in Fig. 2.4, although the argument and function has switched roles relative to what is shown in Howe (1993). The graph shows the required cycle bars for any possible success rate relative to the requirement for 50% success (N50). From Table 2.1, we know that N50 is 1.00 for detection, 4.0 for recognition, and 6.4 for identification. With this in mind, Figure 2.4 can be used for all 3 discrimination tasks. The dashed lines indicate the result for the three success rate cases given in Table 2.1, 50%, 70% and 90%.

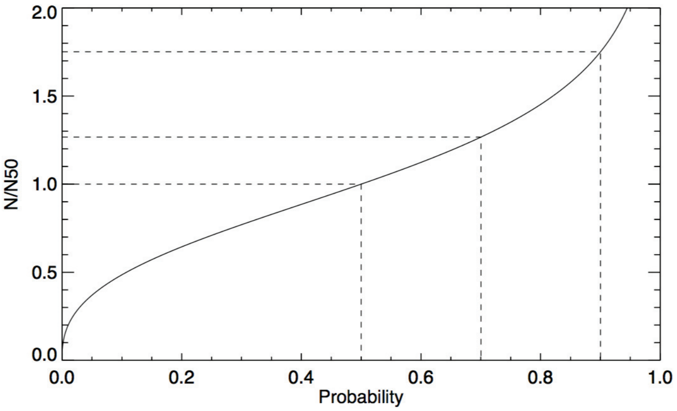

Figure 2.4 Required ratio of cycle bars to the 50% cycle bar as a function of the success probability.

In order to demonstrate the Johnson Criteria, we examine three different examples. First, we look at a human model, 1.8 m tall and 0.5 m wide, with a critical dimension just under 1 m. The model is shown in Fig. 2.5d with a green square representing the equivalent target. Let's say we want to operate with a success rate of 80%. By combining the information from Table 2.1 and Fig. 2.1, we find that we need to resolve 1.5 bar cycles (corresponding to 3 pixels) across the critical dimension to achieve detection with the prescribed probability. This is illustrated in Fig. 2.5a by the red-toned, vertical bars covering the equivalent target shape. At this minimum resolution, the human shape itself has been reduced to a 1-by-6 pixels large, half-lit rectangle. At this point, it is not possible to recognise the shape as human. To be able to that, we need approximately 6 bar cycles across the critical dimension. With this resolution, one should have a fairly good chance at recognising arms and legs, indications that the observed target is indeed a human. This case is shown in Fig. 2.5b. Finally, to be able to identify a human with a probability of 80%, you will need about 10 bar cycles across the critical dimension. This might still not be enough to identify a specific individual, as Fig. 2.5c indicates, but should make you capable of obtaining additional information about the target.

The next example, taken from FLIR Systems Inc. (2019), is also a human with roughly the same size as in the previous case. In this case, we look at thermal images of a man holding a rifle. This time, the probability of task success is set to 50%. From table 2.1, we find that the required number of bar cycles across the critical dimension for detection, recognition, and identification is 1, 4, and 6.4, respectively. Fig. 2.6 shows how the target will appear through a thermal camera with the given resolution levels. The man is detected when a single pixel covers roughly the width of the man. With 4 pixels spanning the man's width, we start to realise this is a human being, and when the resolution has increased to 6-7 pixels across the man's width, we can even start to identify the rifle he is pointing upwards to his right.

The final example is of a vehicle, namely a tank. In Perić et al. (2019) where this example is taken from, they assume the critical target dimension is 2.3 m, although this is not important to illustrate the Johnson Criteria. Again, the probability of success is set to 50%. The required number

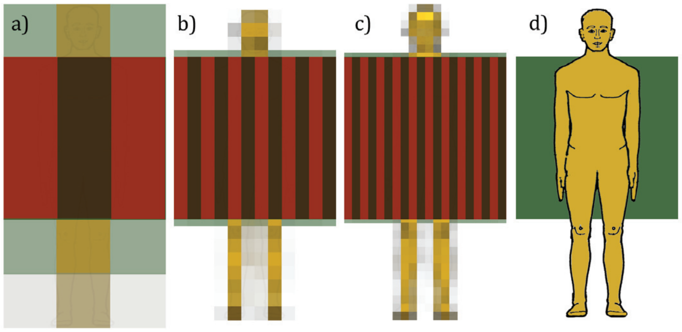

Figure 2.5 Johnson Criteria demonstrated on a 1.8 m tall and 0.5 m wide human model reproduced in panel **d**. *The green squares represent the equivalent target, and the red/brown stripes indicates the bar cycles. Panel* **a**, **b**, *and* **c** *show the minimum resolution required for detection, recognition, and identification at 80% probability.*

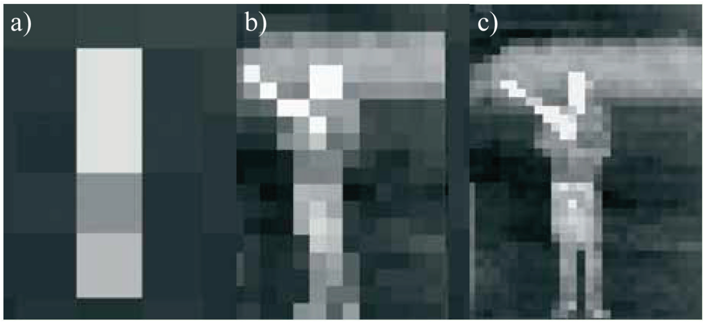

Figure 2.6 Another example of the Johnson Criteria applied to a 1.8 m tall and 0.5 m wide human, this time holding a rifle. Panel **a**, **b**, *and* **c** *show the minimum resolution required for detection, recognition, and identification at 50% probability. Taken from FLIR Systems Inc. (2019).*

of bar cycles for a given task is therefore the same as in the previous example, despite the fact that the target is completely different from that of the previous case. This illustrates a key point of the Johnson methodology, that the resolution requirement can be formulated independently from the target shape, through the introduction of the equivalent target shape. Fig. 2.7 reproduces one of the figures from Perić et al. (2019) which illustrates the Johnson Criteria applied to a generic tank.

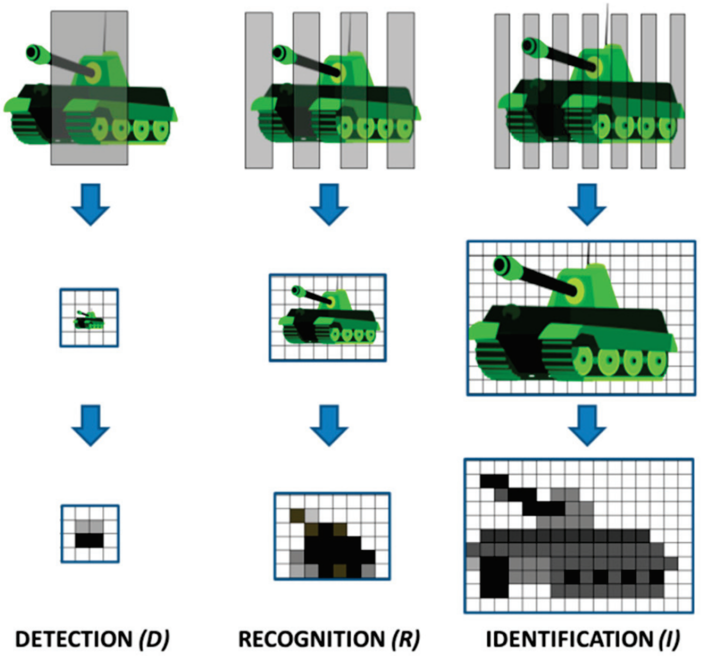

Figure 2.7 Johnson Criteria demonstrated on a tank with a 50% success rate (Perić et al., 2019).

3 Examples of thermal camera systems

The technical specifications of the thermal camera system is obviously one of the factors that influences the maximum distance at which relevant target information can be obtained. We have selected 6 different thermal cameras to use as examples when calculating detection range using the two methods described in this report. The two most relevant cameras, the FLIR A655SC camera and the Jim Compact binocular, are considered in two different configurations, both in a narrow angle and a wide angle setup. Since we treat them here as separate systems, we are in total considering 8 different camera systems. The other systems included are chosen both because the required technical specifications for these systems are easily available and because they in combination make up a fairly representative selection of thermal camera systems available on the market. A complete list of the camera systems is given in Table 3.1 with the technical specifications used in this report.

FLIR A655SC/A655MAG

FLIR A655SC is a fairly compact (216 mm long) uncooled microbolometer which operates in the LWIR spectral range with a temperature resolution of 30 mK. It can stream 16-bit data at 50 Hz (up to 200 Hz with windowing). In its base configuration, the field of view is 25° which makes it more suitable to surveilling a larger area rather than tracking smaller targets. However, the camera can be fitted with a compatible lens which reduces the field of view to 7°. This latter configuration will in this work be referred to as A655MAG. The FLIR A655SC is shown in Fig. 3.1d.

Safran Jim Compact

Jim Compact is a pair of light-weight (less than 2 kg), long-range multifunction binoculars acquired by the Norwegian Army in 2018. The thermal (MWIR) sensor is provided by Sofradir (which in 2019 merged with a subsidiary to form Lynred). It boasts a powerful zoom which can deliver a field of view ranging from 4.5° to 13.5°. In this work, we consider the two extreme zoom settings as two separate systems. The Jim Compact binoculars are shown in Fig. 3.1a.

Hensoldt Z:NightOwl®ZM

Z:NightOwl®ZM is a much larger system then the first two. It was designed for remote-controlled, standalone or network operation. It is suited for stationary solutions or for vehicle integration and has a full 360° observation sector. The system weighs 59 kg and has a power consumption of up to 100 W. Like the Jim Compact binoculars, this system uses an MWIR sensor. A continuous 12.9x optical zoom allows the horizontal field of view to be increased from 0.95° to 12.2°. In our range discussion of the system, we look at the smallest field of view, 0.95°. Z:NightOwl®ZM is seen in Fig. 3.1b.

Vlatacom systems 1 & 2

The next two systems are similar in size and design to the Z:NightOwl®ZM system. They are solely included because they are reasonably well documented in the work of Perić et al. (2019), not because they are expected to be directly relevant to the Norwegian Armed Forces. Both systems were developed by Vlatacom Institute in Belgrade, Serbia, and have a spectral range of 3.6-4.2μm, and both systems have a fixed field of view. System 2 has twice the pixel size of the previous systems in Table 3.1. The two systems are seen in Figs. 3.1e and 3.1f, respectively.

Vayu HD

The last thermal camera to be considered, shown in Fig. 3.1c, is an example of a modern, small-pixel, uncooled LWIR microbolometer. Vayu HD is produced by Sierra-Olympic (Oregon, USA) and is the only camera on the list with a pixel pitch as small as 12μm. The number of pixels, on the other hand, is the largest found on the list, with 7.5 times more pixels than that found on the FLIR camera and the Jim Compact binoculars. It also has the largest field of view, over 52°, of the camera systems considered here. The weight is comparable to Jim Compact, only 2.7 kg.

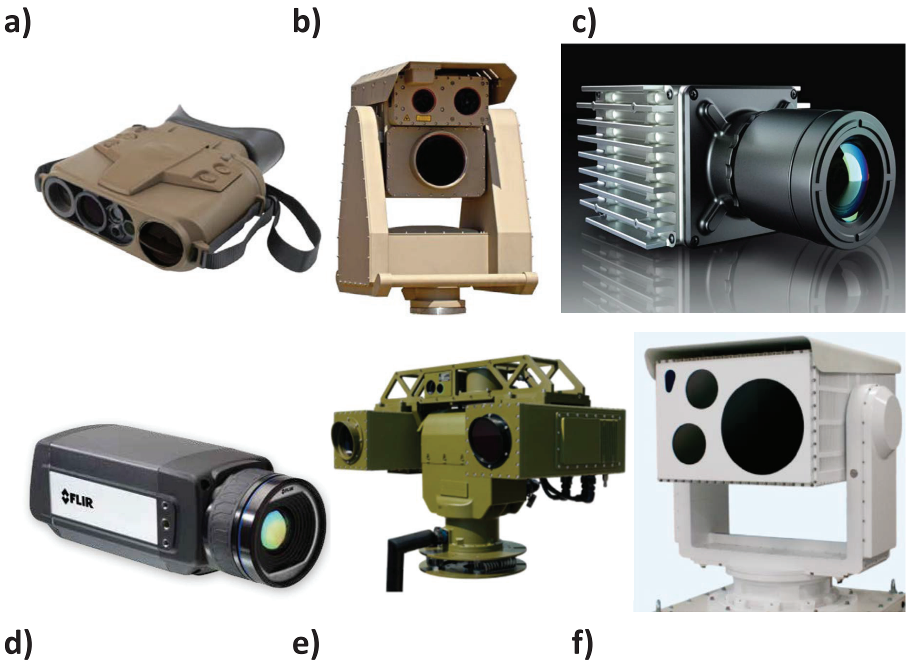

*Figure 3.1 Images of thermal cameras used as examples in this report: Jim Compact binocular (**a**), Z:NightOwl® ZM (**b**), Vayu HD (**c**), FLIR A655SC (**d**), Vlatacom system 1 (**e**), and Vlatacom system 2 (**f**).*

Brand	Model	Spectrum (μm)	$N_x \times N_y$	δ (μm)	d (mm)	α (°)	f (mm)	ϵ (mrad)
FLIR	A655SC	7.5-14	640×480	17	11	25	25	0.68
FLIR	A655MAG	7.5-14	640×480	17	11	7	89	0.19
Safran	Jim Compact WFOV	3-5	640×480	15	11	13.5	41	0.37
Safran	Jim Compact NFOV	3-5	640×480	15	11	4.5	122	0.12
Hensoldt	Z:NightOwl® ZM	3-5	640×512	15	9.6	0.95	580	$2.6 \cdot 10^{-2}$
Vlatacom Institute	System 1	3.6-4.2	640×512	15	9.6	1.7	330	$4.5 \cdot 10^{-2}$
Vlatacom Institute	System 2	3.6-4.2	1280×1024	15	19	0.92	1200	$1.3 \cdot 10^{-2}$
Sierra-Olympic	Vayu HD	8-14	1920×1200	12	23	51.3	25	0.47

Table 3.1 *List of camera system used as examples in this report with information about brand, model, spectral range, number of pixels, pixel pitch (δ), sensor width (d), field of view (α), and instant field of view (ϵ). The list is sorted according to decreasing pixel pitch and increasing pixel size.*

4 Method 1: Pixels-on-target (POT)

We want to estimate the maximum range at which we can expect to successfully accomplish a specific acquisition task on a given target. The first and simplest method that we will explore, which we will be referring to as the **pixels-on-target** (POT) method, is based solely on the Johnson Criteria in combination with expressions of the basic camera properties. Being the simplest range estimation method also implies that is relies on the most simplifying assumptions. The most important of these assumptions are:

1. The temperature difference between the target and the background is large. If the target is sufficiently resolved, it will easily be distinguished from the background.
2. The atmospheric attenuation is negligible. In other words, the weather is optimal.
3. The detector noise is negligible, the camera optics have an optimal design, and the display is perfect.
4. No image processing, which could sharpen images, enhance contrast, or suppress noise, is considered.
5. The performance of the human observer (assuming manual and not automated detection) does not deviated significantly from the observer model in the Johnson Criteria.

We start by rewriting Eq. 2.2 to get an expression for the target distance:

$$R = \frac{D}{d} f. \tag{4.1}$$

Since D is the real width of the entire image with pixel width N, and the inverse of $\mathrm{n}_{\mathrm{ppm}}$, given in Eq. 2.8, is equal to image meters per pixels, we get D in meters as

$$D = \frac{N}{\mathrm{n}_{\mathrm{ppm}}}. \tag{4.2}$$

From Eq. 2.4 we can express the sensor width d in terms of N and the pixel pitch δ, and from Eq. 2.5 we can replace the focal length f with the ratio of δ to the instantaneous field of view ϵ. If we do this, we can rewrite Eq. 4.1 as

$$R = \frac{L}{2 J_{\mathrm{bcc}} \epsilon}. \tag{4.3}$$

Eq. 4.3 is the mathematical formulation of the POT method. We see that according to this estimation method, the effect of camera properties on the acquisition range can be expressed by a single parameter, the instantaneous field of view. If we replace ϵ with the Nyquist frequency, we get

$$R = \frac{L}{J_{\mathrm{bcc}}} \nu_N. \tag{4.4}$$

The range is also proportional to the Johnson bar cycle count, which in turn depends on the specific acquisition task as well as the desired probability of success, and the critical target dimension.

4.1 POT-estimated acquisition range

Using Eq. 4.3, we estimate the acquisition range according to the Pixels-on-target method for all 8 systems listed in Table 3.1. We estimate effective range for all 3 tasks (detection, recognition, and identification) and with varying probability of success. We also look at varying target size. In particular, we will look at 3 specific targets, a hypothetical object the size of an A3 paper, a human, and a CV90 tank. The width and height of the A3 target is 0.42 m by 0.30 m resulting in a critical dimension of 0.35 m, while we assume the same human model as before with height 1.8 m and height 0.50 m by 1.8 m giving a critical dimension of 0.95 m. As for the CV90, the length, width, and height is 6.8 m, 3.2 m and 2.8 m, respectively. If the CV90 is observed from the front, the critical dimension becomes 3.0 m. If instead, the vehicle is observed from the side, the critical dimension increases to 4.4 m. Assuming the orientation is likely to vary in time, we choose the arithmetic average between the length and width as target's effective width. This gives the CV90 an average critical dimension of 3.7 m.

First, we focus on simple detection with the two most relevant camera systems, the FLIR bolometer and the Jim Compact binoculars. In Fig. 4.1, the detection range according to the POT method as a function of a target size ranging from 10 cm to 10 m is plotted. Estimates are shown for FLIR A655SC (panel **a**), FLIR A655MAG (panel **b**), Jim Compact WFOV (panel **c**), and Jim Compact NFOV (panel **d**). The black, blue and green lines correspond to a probability of success of 50%, 70%, and 90%, respectively. As given by Eq. 4.1, we see that the estimated range is proportional to the target size (both axis are logarithmic). The plotted lines also illustrate how the estimated range drops by 20% and 42%, when the rate of success is increased from 50% to 70% and 90%, respectively. The best range according to the POT-estimate, is achieved with Jim Compact NFOV. An A3-sized target should be identified with 70% probability at a distance of over 1000 m. In comparison, equipped with a FLIR A655SC camera, you would have to get closer than 600 m to detect a human with the same chance of success.

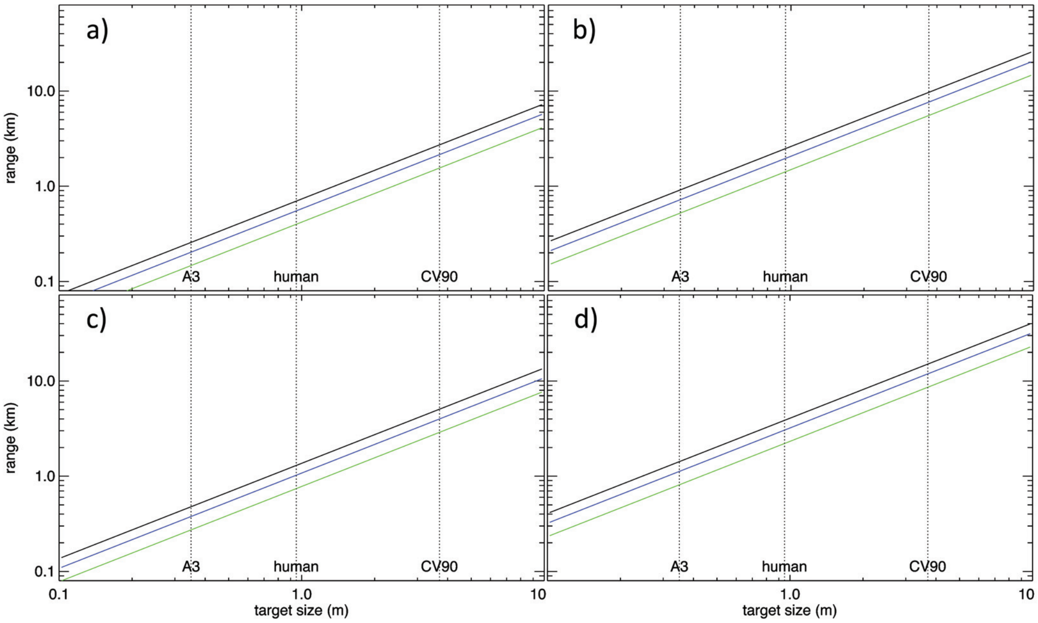

*Figure 4.1 Detection range according to the POT method plotted as a function of target size with the probability of success set to 50% (black lines), 70% (blue lines), and 90% (green lines). Estimates are shown for FLIR A655SC (***a***), FLIR A655MAG (***b***), Jim Compact WFOV (***c***), and Jim Compact NFOV (***d***).*

Fig. 4.2 shows plots of similar type, this time for all 8 camera systems considered in this report. Panels **a**, **b**, and **c**, show estimated range for detection, recognition, and identification, respectively, and all the estimated ranges refer to 70% probability. 5 of the 8 systems are compact and can be hand held, while the remaining 3 are larger systems, either stationary or vehicle mounted. Not surprising, the large systems provide the longest acquisition ranges, but bear in mind that long range usually comes at the expense of a small field of view. If we assume a observation distance of 3 km, we should, according to the POT estimate, be able to detect a 10 cm target with the Vlatacom 2 system, a 20 cm target with Z:NightOwl®, and an A3-sized target with Vlatacom 1. With any of the compact systems used at the same distance, we should be able to detect a human using the Jim Compact binoculars at maximum zoom, a 1.5 m target with FLIR A655MAG, a CV90 observed from the front using the Jim Compact binoculars at maximum field of view, an orientation-averaged CV90 with Vayu HD, and a 5.5 m target with FLIR A655SC. If we want to be able to recognize these targets, the observation distance according to the POT estimate has to be reduced to about 800 m, and if we require identification of the targets, the observation distance has to be reduced further to 500 m.

How the estimated detection range depends on the probability of success, is illustrated in Figs. 4.3 and 4.4. In the first figure, the probability of successful detection of an A3-sized target (black curves), a human (blue curves), and a CV90 vehicle (green curves) is plotted as a function of distance to target for the systems FLIR A655SC (**a**), FLIR A655MAG (**b**), Jim Compact WFOV (**c**), and Jim Compact NFOV (**d**). In the second figure, panels **a**, **b**, and **c** show the same function when the target is an A3-sized object, a human, and a CV90 vehicle, respectively, for all 8 systems listed in table 3.1. In both cases, we see that the estimated detection range is fairly insensitive to the probability of success, unless the probability is set to larger than 80% or less than 20%. Apart from this, Fig. 4.4 illustrates the differences between the different camera systems quite nicely.

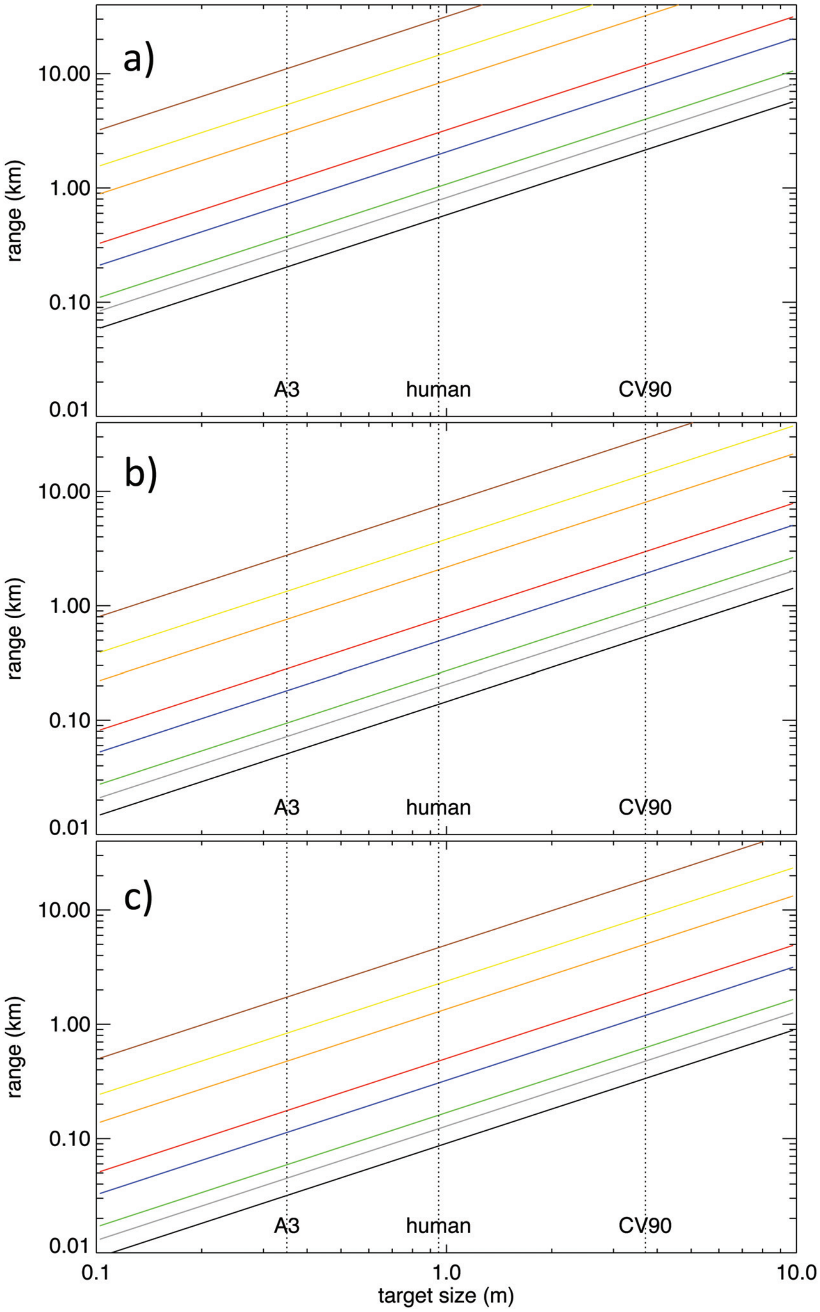

Figure 4.2 *Comparison of estimated range according to the POT method plotted as a function of target size for all 8 camera systems. The probability of success is set to 70% and the acquisition task is specified to be detection (***a***), recognition (***b***), and identification (***c***). The 8 systems are identified by the colours black (FLIR A655SC), blue (FLIR A655MAG), green (Jim Compact WFOV), red (Jim Compact NFOV), yellow (Z:NightOwl®), orange (Vlatacom 1), brown (Vlatacom 2), and grey (Vayu HD).*

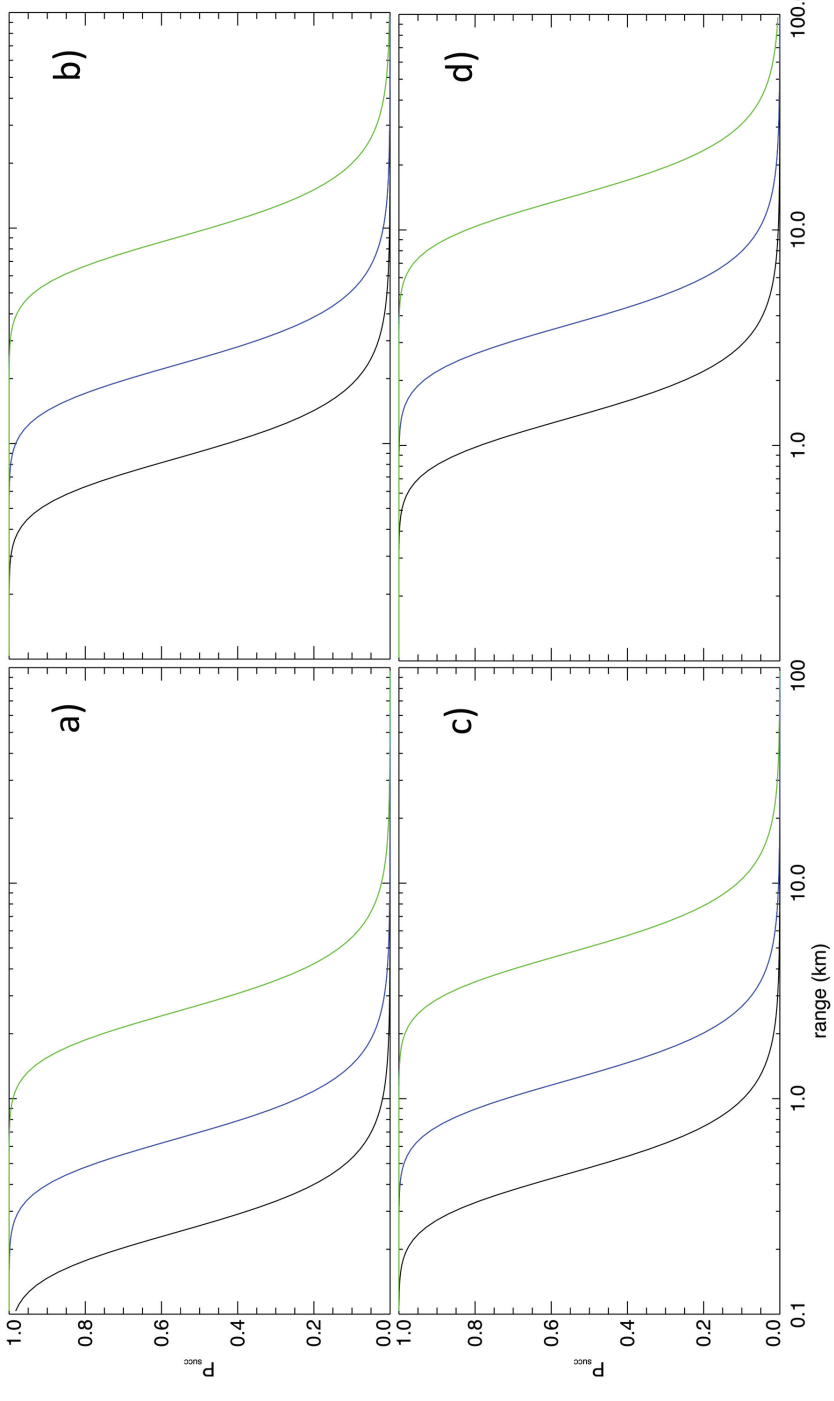

*Figure 4.3 Probability of successful detection of an A3-sized target (black curves), a human (blue curves), and a CV90 vehicle (green curves) according to the POT method as a function of target distance. Estimates are shown for FLIR A655SC (***a***), FLIR A655MAG (***b***), Jim Compact WFOV (***c***), and Jim Compact NFOV (***d***).*

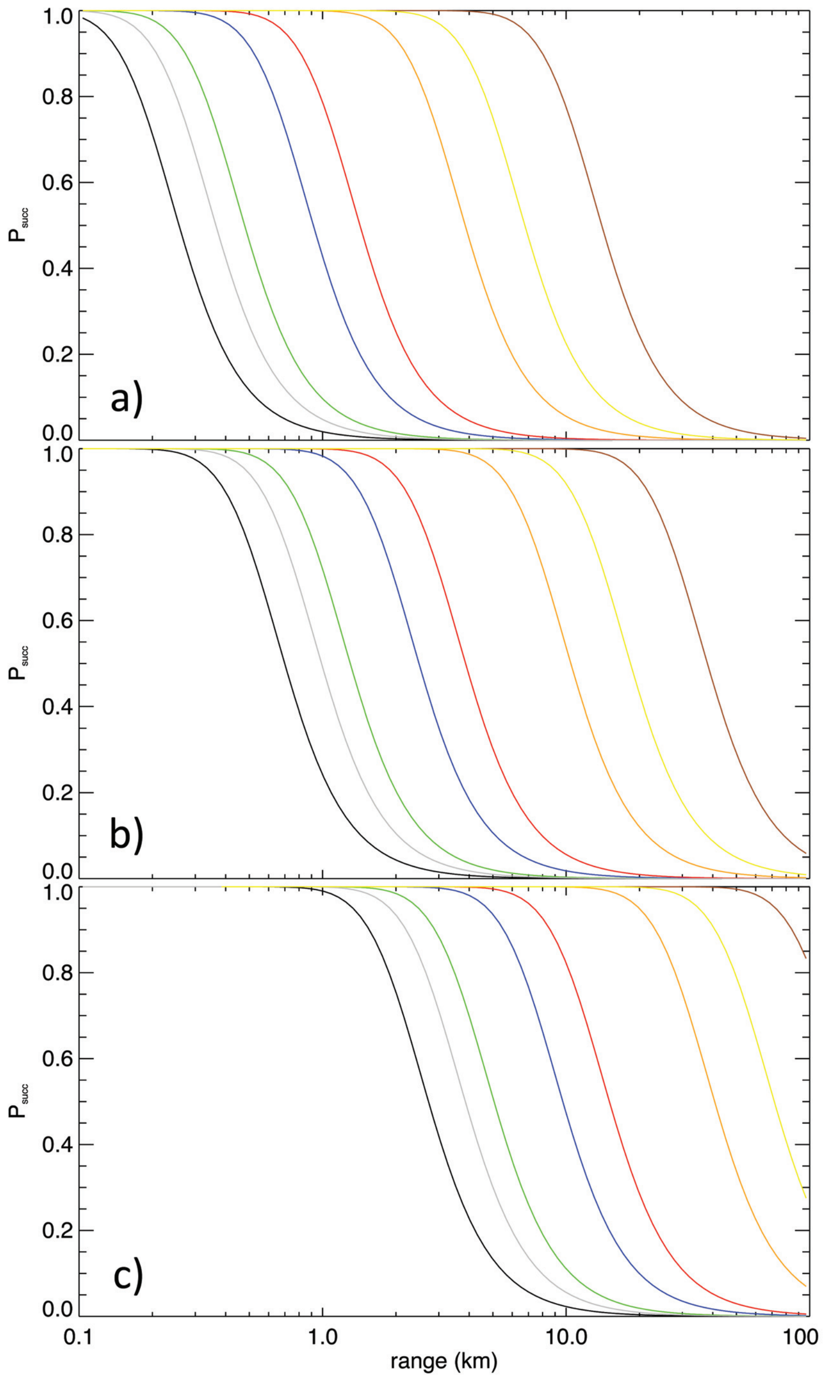

Figure 4.4 *Probability of successful detection of an A3-sized target (**a**), a human (**b**), and a CV90 vehicle (**c**) according to the POT method as a function of target distance. Estimates are shown for FLIR A655SC (black), FLIR A655MAG (blue), Jim Compact WFOV (green), Jim Compact NFOV (red), Z:NightOwl® (yellow), Vlatacom 1 (orange), Vlatacom 2 (brown), and Vayu HD (grey).*

5 Introduction to atmospheric attenuation

We all have experienced how visibility can be reduced due to non-ideal atmospheric conditions, whether it be due to natural weather conditions, such as haze, fog or snow, or due to air pollution, predominantly in high populated areas. This extinction effect, which is called atmospheric attenuation, is important to be aware of when observing in infrared just as it is in visible light. Even so, atmospheric attenuation is highly dependent on wave length and common knowledge from visible light is not directly applicable to observations in infrared. It is also important to be aware of that the net atmospheric attenuation is the combination of many attenuating effects, normally divided into the main categories absorption, scattering and refraction. It is also useful to distinguish attenuation due to atmospheric gases from attenuation caused by aerosols.

We present a brief introduction to the topic of atmospheric attenuation here. A relatively detailed model estimating the atmospheric attenuation associated with a range of common atmospheric conditions has been implemented and is described in Appendix A. The attenuation model is applied to the examples presented in section 7 and used to generate the extinction coefficient tables provided in Appendix B.

5.1 Gas attenuation

Light travelling through a media such as the atmosphere, will to some extent be absorbed, primarily due to interactions with gas molecules. How much of the light is absorbed in a given distance is dependent on the wavelength and to what degree different molecules with absorption bands covering the wavelength are present. Water vapour is by far the most important absorbing gas in the atmosphere when it comes to infrared transmission. Unfortunate from a range prediction perspective, it is also the most variable gas in the atmosphere. Together with CO_2, water vapour defines what is known as the 3-5 μm and 8-14 μm atmospheric windows. Fig. 5.1 is taken from Thomas & Duncan (1993) and shows the absorption of the seven most significant molecule absorbers in a model atmosphere as a function of wavelength. We see that in addition to H_2O and CO_2, there are important contributions to the overall absorption from especially N_2O and O_3. At the bottom, the combined absorption of all seven species is shown.

Molecules can also cause scattering which is a process where the light emitted from the target and originally directed towards the sensor is deflected due to interactions with the atmosphere. In practice, scattering will cause the amount of radiation reaching the sensor from the target to be reduced in the same way as absorption does. Gas scattering is normally due to what is known as **Rayleigh scattering**.

5.2 Aerosol attenuation

In addition to gas molecules, the atmosphere contains particles in the form of dust, sand, water droplets, ice, salt spray etc., and the main contributors are sea spray, fog, haze, dust storms and air pollution, although there are many processes that can generate a wide range of different aerosol types. Attenuation caused by aerosols is dominated by scattering where the ratio between the wavelength and size of the aerosol particles is of great importance. With potentially large temporal and spatial variation in both the aerosol size distribution and concentration, it can be very challenging to estimate the attenuation caused by particles.

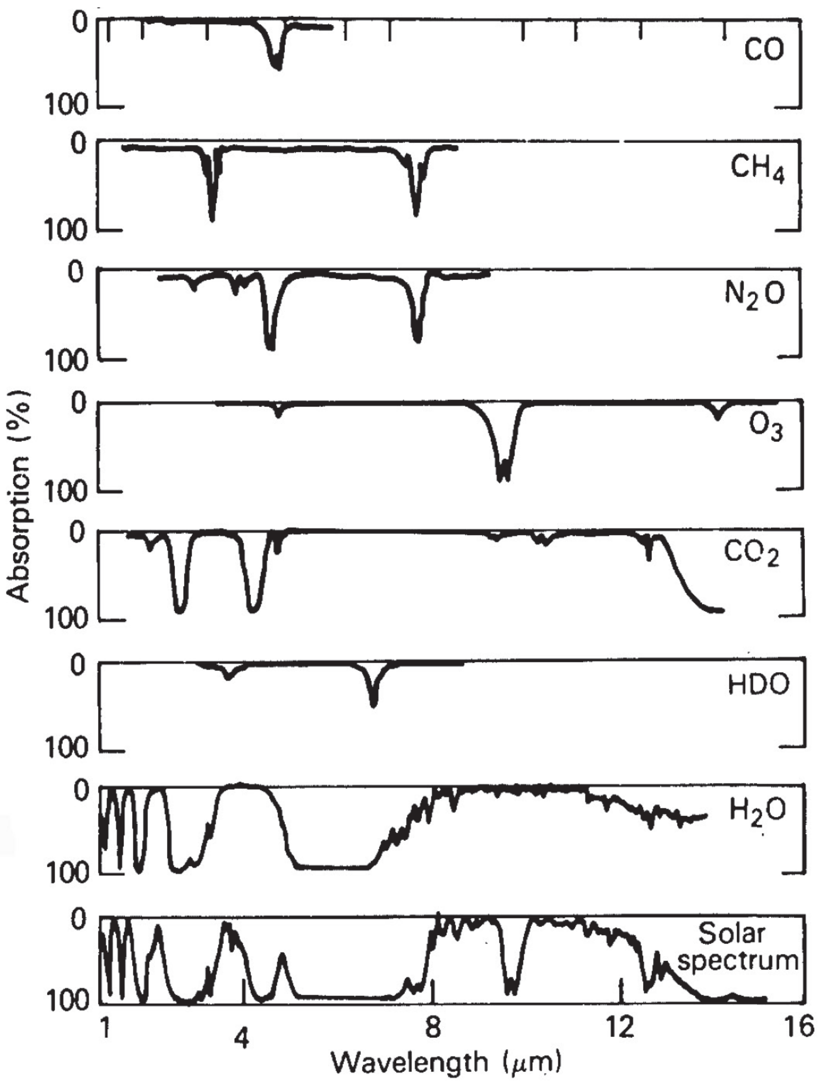

Figure 5.1 Laboratory absorption spectra of the 7 most significant molecule absorbers in the atmosphere as a function of wavelength, compared with the corresponding low-resolution solar spectrum (taken from Thomas & Duncan (1993)).

5.3 Beer’s law

If we were to properly take into account atmospheric attenuation and how this would affect the range prediction for a thermal camera system, there are a number of different factors we should include. Before even considering the atmosphere itself, we should keep in mind that radiation emitted from the target might very well deviate from the Planck radiation law (described in section 1). This deviation is normally given by the emissivity which is a dimensionless parameter. The same will apply to the background. Also, the spectral response of the sensor might not be ideal and might be more sensitive at certain wavelengths. Assuming we neglect all these non-ideal effects that are not connected with the atmosphere, we still face a challenging task in estimating the atmospheric attenuation given that it depends on so many physical processes and varies so much with wavelength.

Faced with the options of either neglecting the atmospheric attenuation altogether or having to make highly complex calculations which rely on detailed information about the state of the local atmosphere, a common solution is to resort to an approximation known as **Beer's law** where the **atmospheric transmission**, $\tau = \tau_B$, is given as

$$\tau_B(R) = e^{-\gamma R}, \tag{5.1}$$

where γ is an appropriate *extinction coefficient* and R is the distance. The approach is described in detail in Goodell & Roberts (1979). It is stressed that this approach can only be expected to be useful for very narrow spectral intervals (roughly monochromatic radiation) or in cases where the attenuation exhibits a weak dependence on wavelength. The authors claim the method to be reasonably accurate within the two main infrared observation intervals of 3-5 μm and 8-14 μm if the attenuation is dominated by aerosol particles, H_2O, and N_2O. However, since the water content in the atmosphere drops off quite rapidly with altitude, this approach also tends to be highly inaccurate if the observation path spans an altitude range of several kilometers.

Temperature differences, which is what a thermal sensor is meant to detect, will appear smaller when observed from a distance if the atmospheric transmission is not ideal. For practical use in range estimation, it is therefore desirable to translate atmospheric transmission into **apparent temperature difference (ATD)** as a function of observation distance. Several different methods for estimating ATD are evaluated in Vinson et al. (1998). The simplest approach estimates ATD, denoted ΔT_a, by

$$\Delta T_a(R) = \Delta T_0 \tau(R), \tag{5.2}$$

where ΔT_0 is the true temperature difference between the target and the background. If we assume Beer's law, we arrive at the much used (and some claim abused) expression for ATD:

$$\Delta T_a(R) = \Delta T_0 e^{-\gamma R}. \tag{5.3}$$

Vinson et al. (1998) investigates the errors associated with different ATD estimates for the 3-5 μm and 8-12μm bands. According to their results, the errors associated with the use of Beer's law to estimate $\tau(R)$ instead of integrating the transmission along the observation path are much larger than the errors incurred by assuming the coupling between apparent temperature and broadband transmission (as given by Eq. 5.2). This is especially true in the 3-5 μm band. It is also worth noting that the errors in estimating ATD using Eq. 5.3 is larger in their summer atmosphere model than in their winter atmosphere model due to the higher ground level humidity. The reported errors in ATD are up to 12% per km range and 8% per km range for the 3-5 μm summer and winter models, respectively. The corresponding errors for the 8-12μm band is 4% per km range for the summer model and only 1.2% per km range for the winter model. A positive error means that the estimated ATD drops faster with distance than in reality. However, it does not state anything specific about the inclination of the observation path, although a vertical observation path in this case appears to be likely. Despite the inaccuracy, we will use Beer's law in the method to be presented in section 6. Partly, becuase this allows us to formulate simple algebraic range estimates. Also, we will primarily limit ourselves to low altitude, more or less horizontal observation paths. This to some extent justifies using atmosphere-averaged extinction. As an example, if a sensor is placed at an elevation of 30 m above sea level and directed towards the horizon, the observation path will not exceed its original altitude unless the path length is larger than 40 km.

6 Method 2: MRTD-based estimation

Predicting the effective range of thermal sensors is difficult due to the many factors that can affect the real-world range. The Pixel-on-target (POT) method, described in section 4, dealt with this by neglecting most of these factors, at the expense of accuracy. In the current section, we will describe a method aimed at providing slightly more realistic range predictions. For example, the method takes into account the finite temperature difference between target and background and the weather dependent atmospheric attenuation (although in a simplified manner). Factors such as detector noise, image processing in the camera and human observer performance (assuming manual detection) are all assumed to be incorporated in the experimental data which the method relies on and has received its name from.

6.1 Performance measures for thermal sensor systems

Several related performance measures for thermal sensor systems have been defined to help predict the effective range of the systems and a good overview is given in Ratches (1976).

6.1.1 Noise equivalent temperature difference (NETD)

A quantity which is fairly often referred to is the **noise equivalent temperature difference (NETD)**. NETD is defined as the temperature difference above 300 K between a sufficiently large target and its background giving rise to a peak signal to nose ratio (SNR) equal to unity at the detector output. Of the camera systems described in section 3, A655SC, Z:NightOwl®ZM and Vayu HD all have NETD levels in the range 30-35 mK. We do not know the NETD value for Jim Compact. However, as it is a modern, commercial system, it is reasonable to believe that its NETD value is similar to the other commercial systems. The two Vlatacom systems, on the other hand, appear to have NETD values around 100 mK based on the MRTD curve provided, although this is not explicitly stated (Perić et al., 2019).

6.1.2 Minimum detectable temperature difference (MDTD)

NETD is strictly a measure of system sensitivity and does not include display or observer characteristics. More specifically, the quantity does not reflect the performance of a human observer. **Minimum detectable temperature difference (MDTD)**, which is assumed to be proportional to NETD, is a laboratory measure of thermal systems which also include the effect of the human observer. The quantity is defined as the temperature difference between a square target and a uniform background required for a trained observer to detect the target using a given thermal imaging system. As we saw in section 2.2, a small target might appear larger but cooler than it really is due to spatial aliasing. This effect increases with decreasing target size. The apparent cooling causes the MDTD to increase with decreasing target area. As the radiation from the target is averaged over minimum one pixel, there is however no limit to how small a detectable target might be assuming the target is sufficiently hot.

With this in mind, one might conclude that there is no lower limit to the size of detectable targets if one assumes sufficiently large target temperatures. In practise, this is not so. First of all, there are limits to how large the temperature difference can become in real-world scenarios. Also, the background will not be completely thermally uniform, as specified by the MDTD definition.

Given a non-negligible temperature variation in the background, also known as **thermal clutter**, a small target can become impossible to distinguish from the background if the target-background temperature difference is not large enough. Even if the task is to merely detect the target, one might depend on a certain level of recognition in order to distinguish a static target from the background. This leads us back to the Johnson Criteria introduced in section 2.3 which is also used by the pixel-on-target range prediction method.

6.1.3 Minimum resolvable temperature difference (MRTD)

In order to couple the concepts of Johnson with an appropriate performance measure, the parameter called **minimum resolvable temperature difference (MRTD)** was introduced. Like MDTD, this parameter is a subjective measure of image quality. MRTD is defined as the minimum temperature difference above 300 K required for an observer viewing through the tested imaging system to resolve a four-bar pattern from the background. It is important to emphasise that the observer must be able to see 4 distinctive bars at the MRTD. The bars should have an aspect ratio of 7:1 and be vertically aligned[2]. MRTD, like MDTD, is defined as an laboratory measurement which should ideally be determined experimentally for all imaging systems where range predictions are desired.

Unfortunately, it has been difficult to obtain good quality, reproducible data. This is because the results depend not only on the sensor system itself, but also on the training, motivation, and visual capacity of the observer. For this reason, determining the MRTD experimentally requires averaging the results from many different observers. Variation in the measured MRTD for a given system is said to be as high as 50% from laboratory to laboratory, and as high as 20% within any one laboratory (Holst, 1993). According to Krapels et al. (2002), test results often suffer from a lack of rigorous test procedures as well fundamental under-sampling issues related to focal-plane array (FPA) sensors, the category to which most modern-day sensors belong. By moving the sensor relative to the target, one can eliminate issues related to phase-related variability (Krapels et al., 2002). This can in turn reduce the tendency of experimentally obtained MRTD-curves to exhibit a flattening in the frequency range of roughly 0.6-1.0 times the Nyquist frequency (Holst, 1993; Krapels et al., 2002; van Rheenen et al., 2018).

Although, the MRTD-curve should ideally be obtained experimentally, a theoretical model of MRTD also exists (Ratches, 1976). It depends on a number of other parameters, e.g. the NETD parameter. Unfortunately, most of these parameters are not easily obtained for a given system. But there are general remarks that can be made regarding MRTD. The MRTD-curve should be a monotonically increasing function of the spatial bar cycle frequency. The low-frequency limit is mostly determined by the low-frequency sensor noise and is expected to lie between 0.3 and 0.7 times the NETD value (Holst, 1993). In the high-frequency domain, the MRTD response is largely determined by phase error effects, as described in section 2.2. At around 0.6-0.8 times the Nyquist frequency, ν_N, these errors normally present themselves (Holst, 1993). As a consequence, the bars no longer appear equal in width and intensity. Experience shows that observers often can identify four bars at frequencies as high as 10% above ν_N. However, an absolute cut-off must exist at sampling rate frequency, $2\nu_n$, as the bar pattern would then be perceived as a uniform 4-by-7 rectangle.

---

[2] An extension to include horizontally aligned patterns exists (Krapels et al., 2002).

6.2 STANAG 4347

A method of MRTD-based range estimation is described in STANAG 4347. It is proposed as a standardised criteria for comparing the static range performance of different thermal imaging systems (NATO STANAG 4347, 1995). It is said to be applicable to ground targets "seen from the surface or from slightly elevated positions" for the spectral ranges 3-5 μm or 8-14 μm or parts of these ranges. What is referred to as the **nominal range performance** of a system is calculated for a target 2.3 m × 2.3 m in size with a 2 K temperature difference relative to the background. It uses a graphic-based solving technique which combines the Johnson Criteria, the MRTD-curve for the sensor system being tested, and Beer's law as stated in Eq. 5.3. The number of bar cycles required for detection, recognition, and identification is assumed to be 1, 3, and 6, respectively. Two different extinction coefficients, γ, are included. To simulate good transmission conditions γ is set 0.2 km^{-1}, while $\gamma = 1.0$ km^{-1} corresponds to "limited" transmission conditions.

First, the method requires the orientation averaged MRTD-curve (the method for obtaining the average of the horizontal and vertical MRTD-curves are given in the STANAG). Secondly, the curve must be transformed into 3 different functions, one for each of the 3 discrimination tasks, by making a change of variable from frequency (ν) to distance (R). By replacing the fixed Nyquist frequency (ν_N) in Eq. 4.4 with a variable ν, we get the following relation between distance and frequency:

$$R(\nu) = \frac{L}{J_{\text{bcc}}}\nu, \tag{6.1}$$

where in this particular case $L = 2.3$ m and J_{bcc} is 1, 3 or 6 depending on task. By the help of Eq. 6.1, we can now plot the MRTD-curve as a function of distance. Finally, the apparent temperature difference ($\Delta T_a(R)$), as specified by Eq. 5.3, is plotted in the same graph as the MRTD-curve. The estimated range for the specified task, is given by the intersection of $\Delta T_a(R)$ and MRTD(R). It is common practice to make this plot with a logarithmic temperature scale, in which case the function expressing the apparent temperature becomes a straight line.

The graphical range prediction method described in STANAG 4347 is illustrated in Fig. 6.1. In addition to the monotonically increasing MRTD curve for an unspecified sensor system, there are two straight lines in the graph; one for each of the two extinction coefficients specified by the standard. The grey, dashed line shows the apparent temperature difference as a function of distance when $\gamma = 0.2\text{km}^{-1}$, while the black, solid line gives the corresponding result for $\gamma = 1.0\text{km}^{-1}$. In the former case, intersection with the MRTD-curve is achieved at a distance of roughly 7 km when the apparent temperature difference is about 0.5 K. In the latter case, the detection range is estimated to be only around 3.5 km with an apparent temperature difference of about 0.06 K.

6.3 Parameterised MRTD (PMRTD)

The graphical approach is useful in that it can be applied directly to an experimentally obtained MRTD-curve. However, this requires that MRTD values have been found for a sufficiently large frequency range. Also, the method does not provide a simple algebraic expression with which to estimate sensor range and is therefore unsuited for automatic range estimation. To derive an expression for the sensor range, we want to use a parametric MRTD-curve that approximates the experimental MRTD-curve and which can also be used to estimate the MRTD-curve outside the frequency interval for which there exist experimental data.

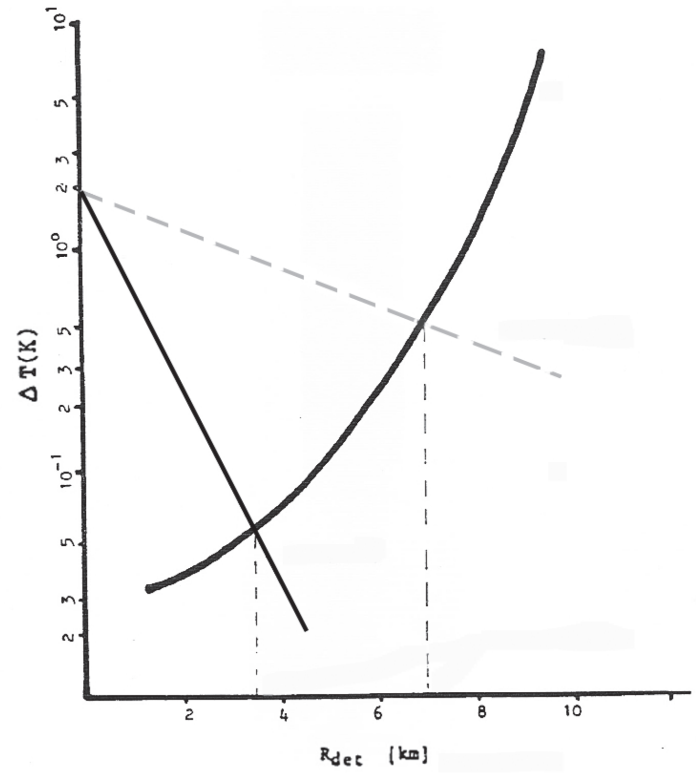

Figure 6.1 *Graphically determined detection range for a given MRTD-curve, target size 2.3 m, and extinction coefficient equal to* $0.2km^{-1}$ *(grey dashed line) and* $1.0km^{-1}$ *(black solid line). The graph is reproduced from NATO STANAG 4347 (1995).*

Based on the general characteristics of MRTD-curves, we propose the following parameterised MRTD form

$$y = y_{\text{min}} + D_y \frac{x_c - 1}{x_c - x} x, \tag{6.2}$$

where we have defined the logarithmic minimum resolvable temperature difference, $y = \log(\Delta T)$, to be a function of the normalised frequency $x = \nu/\nu_N$. The model parameter $y_{\text{min}} = \log(\Delta T_{\text{min}})$ is the logarithmic MRTD at zero frequency, while $D_y = y_N - y_{\text{min}}$, where $y_N = \log(\Delta T_N)$ is the logarithmic MRTD at the Nyquist frequency (corresponding to $x = 1$). The final model parameter, x_c, indicates the asymptotic frequency where the MRTD value becomes infinite. In Fig. 6.2, we see two examples where MRTD curves are approximated by parameterised curves. The left-hand panel refers to the Vlatacom 2 system (Perić et al., 2019), while the right-hand panel uses the same example MRTD curve as STANAG 4347. In both cases, the original MRTD curves are plotted using filled, black circles. The dashed horizontal and vertical lines indicate the zero frequency minimum resolvable temperature and the (normalised) Nyquist frequency, respectively. The three solid curves in each panel represent parametric MRTD curves, with a functional form given by Eq. 6.2, which to a varying degree fits the experimental MRTD curves.

In panel **a**, $\Delta T_{\text{min}} = 0.05$ K and $\Delta T_N = 4$ K is chosen for all three approximations. For this reason, all three curves coincide with the original MRTD curve at these two points. The only

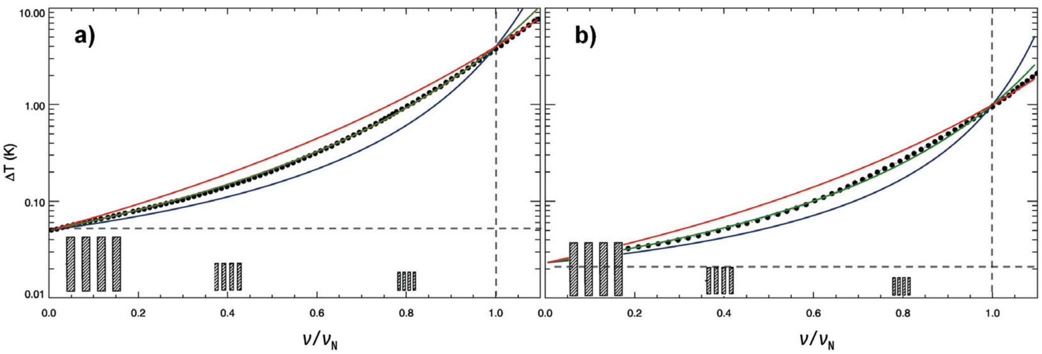

Figure 6.2 Two MRTD-curves as functions of spatial frequency normalised by the Nyquist frequency (ν_N). $\Delta T(0)$ and $\nu/\nu_N = 1$ is indicated by the dashed, horizontal and vertical lines, respectively. The filled, black circles show the original MRTD-curve as taken from Perić et al. (2019) (panel **a***) and NATO STANAG 4347 (1995) (panel* **b***). The solid red, green, and blue lines are parametric MRTD-models with varying asymptote frequency, ν_c.*

difference between the three approximations, which results in the difference in curvature, is the chosen critical frequency, x_c. The blue curve, which has the greater curvature, has a critical frequency which is only 1.5 times the Nyquist frequency. The red curve has the smaller curvature, resulting from choosing $x_c = 3.0$. In comparison, the green curve, which fits the original MRTD curve the best in the frequency range $x \leq 1$, has $x_c = 2.0$. Recall that in section 6.1.3 an absolute cut-off was identified at exactly twice the Nyquist frequency. Similarly to that of panel **a**, a triplet of MRTD approximations are shown in panel **b**. This time $\Delta T_{\text{min}} = 0.023$ K and $\Delta T_N = 1$ K was chosen for all three approximation, while x_c once again was set differently between the three. The blue, green, and red curves has x_c set to 1.4, 1.75, and 2.3, respectively, where the middle value once again gives the better fit in the range $x \leq 1$.

6.4 Range prediction using PMRTD

In order to calculate predicited range, we need to estimate apparent temperature difference as a function of distance. Despite its short-comings (as described in section 5.3), we use Beer's law as proposed in STANAG 4347. We start by taking the logarithm of Eq. 5.3 to obtain the logarithmic apparent temperature difference as function of the observation distance R:

$$y_a \equiv \log(\Delta T_a) = y_0 - \gamma \log(e) R, \tag{6.3}$$

where $y_0 = \log(\Delta T_0)$ is the logarithm of the true temperature difference between the target and the background. The relation between the observation distance and spatial frequency is given by Eq. 6.1. The distance associated with the Nyquist frequency, which is identical to the range estimate according to the pixels-on-target method and which we now will denote by R_N, is given by Eq. 4.4. Combining these two equations, we see that

$$x = \nu/\nu_N = R/R_N, \tag{6.4}$$

and with this relation established, we can rewrite Eq. 6.3 as

$$y_a = y_0 - \Gamma x, \tag{6.5}$$

where $\Gamma = \gamma \log(e) R_N$.

Since we are interested in the *largest* acquisition range, we set the apparent temperature difference, given by Eq. 6.5, equal to the minimum resolvable temperature difference, given by Eq. 6.2. After some rearrangement, this gives us the easily solvable second-order equation:

$$\Gamma x^2 - [\Gamma x_c + E_y + D_y(x_c - 1)]x + E_y x_c = 0, \tag{6.6}$$

where $E_y = y_0 - y_{\text{min}}$. If there is no atmospheric attenuation, $\Gamma = 0$, the predicted normalised range becomes

$$x = \frac{E_y x_c}{E_y + D_y(x_c - 1)}. \tag{6.7}$$

If on the hand, $\Gamma > 0$, Eq. 6.6 is solved through standard methods. This will provide exactly one solution in the range $0 \leq x \leq x_c$ provided $T_0 \geq T_{\text{min}}$. For convenience, we define a new quantity β as

$$\beta \equiv \Gamma x_c + E_y + D_y(x_c - 1). \tag{6.8}$$

Then the predicted normalised range is given as

$$x = \frac{\beta - \sqrt{\beta^2 - 4\Gamma E_y x_c}}{2\Gamma}. \tag{6.9}$$

The physical range according to the parameterised MRTD method is then

$$R = R_N x. \tag{6.10}$$

6.4.1 Characteristics of the PMRTD range solution

A relevant question is how much will range estimation based on the PMRTD method vary with varying instantaneous field of view (IFOV), MRTD parameters, target-background temperature difference, target size, and extinction coefficient. The main properties of the thermal acquisition range estimate given by Eqs. 6.9 and 6.10 will therefore be illustrated in the following. Again, we primarily use the FLIR A655 camera and the Safran Jim Compact binoculars as example systems. To further simplify the discussion, the only acquisition task considered here is detection with a success rate of 50%.

First, we investigate the uncertainty in range estimates which arise from uncertainties in MRTD parameters. In principle, we could perform experiments with a sufficiently large number of test persons to accurately determine the MRTD curve. If so, we would be able to approximate the experimental MRTD curve with a parameterised MRTD curve with a well-defined accuracy. In practice, however, the idealised conditions of an MRTD experiment may not be fully relevant to a real-time acquisition scenario (Krapels et al., 2002).

Another major source of uncertainty is the choice of the extinction coefficient, γ, describing the effect of the atmospheric on the observed temperature differences. Usually, the range estimate will be associated with specific weather and atmospheric conditions. A model for estimating the extinction coefficient based on easily observable weather parameters is presented in Appendix A.

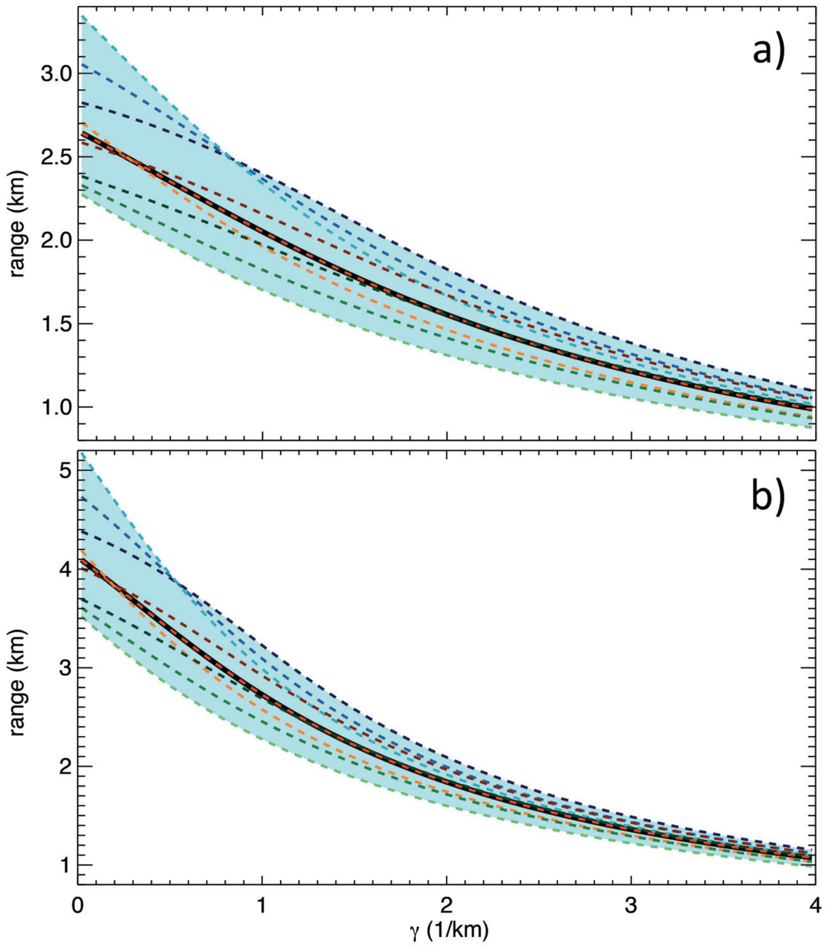

Figure 6.3 PMRTD-estimated range for 50% successful human detection as a function of the extinction coefficient (γ) using the FLIR A655MAG system (panel **a***) and Jim Compact binoculars on maximum zoom (panel* **b***). The target-background difference, ΔT_0 is 2 K, while $\Delta T_{min} = 0.015$ K. For the two remaining MRTD parameters, ΔT_N is 0.25 K (blue curves), 1.0 K (orange/red curves), and 4.0 K (green curves), while x_c is chosen to be 1.4 (darkest shade), 1.8 (medium shade), and 2.6 (brightest shade).*

There will be uncertainties relating how accurately the weather conditions can be characterised and in the models translating this into a given extinction coefficient. There will also be errors related to the attenuation method, as described in section 5.3. Fig. 6.3 illustrates variation in estimated detection range for a human target due to variations in assumed MRTD parameters and γ. Results are shown for the FLIR A655MAG system (panel **a**) and Jim Compact binoculars on maximum zoom (panel **b**). The target-background difference, ΔT_0 is set to 2 K, while the zero-frequency MRTD is fixed to $\Delta T_{\text{min}} = 0.015$ K since it is reasonable to relate this parameter to specified NETD values. Since we have no data from MRTD experiments on these two systems, the two remaining

MRTD parameters, the Nyquist frequency MRTD, ΔT_N, and the normalised critical frequency, x_c, are more uncertain. Based on information given in van Rheenen et al. (2018), Perić et al. (2019) and NATO STANAG 4347 (1995), we have chosen to consider $\Delta T_N = 0.25$ K (plotted in Fig. 6.3 with blue curves), $\Delta T_N = 1.0$ K (orange/red curves), and $\Delta T_N = 4.0$ K (green curves). Based on the discussion in section 6.1.3, x_c is chosen to be 1.4 (darkest shade), 1.8 (medium shade), and 2.6 (brightest shade).

The extinction coefficient is varied from 0 km^{-1}, meaning no attenuation at all, to 4 km^{-1}. In comparison, STANAG 4347 uses 0.2 km^{-1} as good conditions, while $\gamma = 1.0$ km^{-1} corresponds to "limited" transmission conditions. With even more challenging conditions, such as heavy rain or snow, one could expect γ up to 4 or more to be relevant. For FLIRA655MAG, we see from Fig. 6.3**a** that the estimated range using the "median" MRTD model (indicated by the thick, black curves) is about 2.6 km in idealised weather conditions, 1.6 km when $\gamma = 2$ km^{-1} and about 1 km if $\gamma = 4$ km^{-1}. The dashed curves show the variation in the results when the MRTD parameters are varied. We see that ΔT_N is more important to the outcome than x_c, as one might expect. The overall variation in estimates for a given value of γ but varying MRTD parameters is illustrated by the thickness of the light blue region. Comparing the graphs in panels **a** and **b**, we see that the Jim Compact binoculars with maximum zoom is likely give a 60% increase in the human detection range in perfect weather conditions relative to FLIR A644MAG. Considering the uncertainites in MRTD parameters, the range with no attenuation is expected to be in the interval 3.5-5.2 km, which correspond to a range uncertainty of ±20%. As the extinction coefficient increases, both the range uncertainty and the difference in estimated range between the two systems is predicted to decrease to about 10%.

Fig. 6.4 shows the PMRTD detection range with 50% success rate for the FLIR A655SC (panel **a**), FLIR A655MAG (panel **b**), Jim Compact WFOV (panel **c**), and Jim Compact NFOV (panel **d**) as a function of target size. Results are shown for 5 different atmospheric conditions, γ equals 0.2 (black), 0.7 (blue), 1.2 (green), 2.3 (red), and 3.0 (brown). Uncertainty in estimates due to uncertainties in MRTD parameters (as in Fig. 6.3) is indicated by the thickness of the shaded regions. The first observation to be made is that the uncertainties in MRTD parameters are less important than the target size. Secondly, we note that the estimated range is largely insensitive to γ for small targets where the detection range is small in any case. For larger targets, the detection range is expected to drop significantly with increasing atmospheric extinction.

The results in Fig. 6.4 can also be directly compared to the black lines plotted in Fig. 4.1 for the simpler POT method which doesn't take atmospheric attenuation into account at all. Again, the deviation between the two methods is small for small targets. For targets with a critical dimension of 10 m, the PMRTD estimate can in some cases be substantially smaller than the POT estimates. For FLIR A655SC, the PMRTD estimate is only about 4.2% smaller than the POT estimate if the γ is assumed to be 0.2. If instead $\gamma = 1.2$, the PMRTD estimate is less than half the POT estimate. For the other 3 systems, FLIR A655MAG, Jim Compact WFOV and Jim Compact NFOV, the detection range for a 10 m-sized target is predicted to be 36%, 17%, and 53% smaller, respectively, than the POT estimate if $\gamma = 0.2$. For the considerably poorer atmospheric condition of $\gamma = 1.2$, the predicted range for the 3 systems is reduced by between 72% (Jim Compact WFOV) and 90% (Jim Compact NFOV) relative to the POT detection range estimate.

In addition to taking into account atmospheric attenuation, the PMRTD estimate expands on the POT estimate by considering a finite target-background temperature difference. Fig. 6.5 illustrates how the estimated detection range for a human target changes as the target-background temperature difference, ΔT, increases from 0.1 K to 10 K. Results are shown for FLIR A655MAG (panel **a**) and

Jim Compact NFOV (panel **b**), and for 3 different atmospheric conditions, $\gamma = 0.2$ (black curves), $\gamma = 1.0$ (blue curves), and $\gamma = 3.0$ (green curves). Although the temperature difference changes by 2 orders of magnitude, the effect on the estimated detection range is not dramatic. If we use the $\Delta T = 1$ K as reference, we see that the estimated detection range decreases by about 40-50% if ΔT is reduced by a factor 10. If the temperature difference instead is increased by a factor 10, the relative change in detection range is more dependent on the atmospheric conditions. In good weather conditions ($\gamma = 0.2$), the relative increase in detection range is only about 15-20% for the two systems we are considering here. With $\gamma = 1.0$, the detection range is seen to increase by 33-35% following a factor 10 increase in ΔT, and for $\gamma = 3.0$, the detection range is roughly doubled for $\Delta T = 10$ K compared to the case $\Delta T = 1$ K.

Finally, we compare all 8 systems listed in Table 3.1 in the context of parameterised range estimation. We will assume that the MRTD-curve presented in Fig. 6.2a is roughly correct for both the two Vlatacom systems and can be parameterised with $\Delta T_{\mathrm{min}} = 0.05$ K, $\Delta T_N = 4$ K and $x_c = 2.0$. For Vayu HD, we assume the same MRTD parameters as previously used for the two FLIR systems and the two Jim Compact versions, with $\Delta T_{\mathrm{min}} = 0.015$ K, $\Delta T_N = 1$ K and $x_c = 1.8$. For the last system, the Z:NightOwl® ZM, only ΔT_{min} is slightly higher than the assumed parameters for the other commercial systems, increasing from 0.015 K to 0.018 K. In Fig. 6.6, the MRTD estimated detection range of a human (panel **a**) and a CV90 (panel **b**) with 50% success rate is once again plotted as a function of the atmospheric attenuation. There is one curve for each of the 8 systems, but in this case, the 8 systems can be identified only through their IFOV values. The colour of the curves indicate the IFOV on a decibel scale. From bright yellow to black, the 8 curves represent FLIR A655SC, Vayu HD, Jim Compact WFOV, FLIR A655MAG, Jim Compact NFOV, Vlatacom 1, Z:NightOwl® ZM, and Vlatacom 2.

For large atmospheric attenuation, the difference between the different systems becomes less important. This is consistent with what we saw in Fig. 6.4, where the uncertainties in the MRTD parameters were less important for large γ than for small γ. From Fig. 6.6, we see that the estimated range for a human target increases by a factor 2, from about 500 m to just over 1 km, when replacing FLIR A655SC with the Vlatacom 2 system if $\gamma = 4$. On the other hand, if $\gamma = 0$ the relative increase in estimated range is about 50, from around 700 m to some 35 km. The same trend is seen with the bigger target. For $\gamma = 4$, all systems are predicted to deliver about 1 km detection range, with a system-to-system variation of only 10%. Assuming perfect weather conditions however, the CV90 should ideally be detectable at distances ranging from 3 km (FLIR A655SC) to 90 km (Vlatacom 2).

6.4.2 Effect of overestimating the size of hotspots

We also want to consider the effect of target size on estimated detection range from a slightly different perspective. Let us assume that a target has a very inhomogeneous temperature distribution; most of the target surface has only a small or negligible temperature difference relative to the background. One or more hotspots, however, have a temperature which is considerably higher than the surroundings. If a hotspot is small, there will be a tendency of smearing the effect of the hotspot over a larger area than the actual hotpot area, especially if the hotspot is irregularly shaped. This will cause the effective hotspot area to increase and the observed temperature difference to drop. For frequencies close to or above the Nyquist frequency this will be an optical effect, illustrated in Fig. 2.3, which is incorporated in the MRTD curves. For larger hotspots, optical smearing should be negligible. However, during range estimation based on thermal images taken at relatively short ranges, not during an actual detection situation, it might be tempting (or necessary) to simplify the assumed hotspot shape and thereby overestimate the hotspot area. Let us for instance assume that we want to estimate the detection range due to a thermal hotspot on a vehicle. The hotspot-background temperature difference is ΔT_H and the true critical size of the hotspot is L_H. In assessing the characteristics of the hotspot, either manually or through some automatic algorithm, the hotspot area is estimated to have the critical size $L_s > L_H$. The ratio of the estimated and true hotspot critical size is defined as

$$z = \frac{L_S}{L_H} > 1. \tag{6.11}$$

Fig. 6.7 illustrates this for the idealised case of a square hotspot, although estimating the hotspot area in case should be fairly easy. To compensate for the increased hotspot area, we replace the true hotspot temperature difference with an estimated temperature difference, ΔT_S, given as

$$\Delta T_S = \frac{\Delta T_H}{z^2}. \tag{6.12}$$

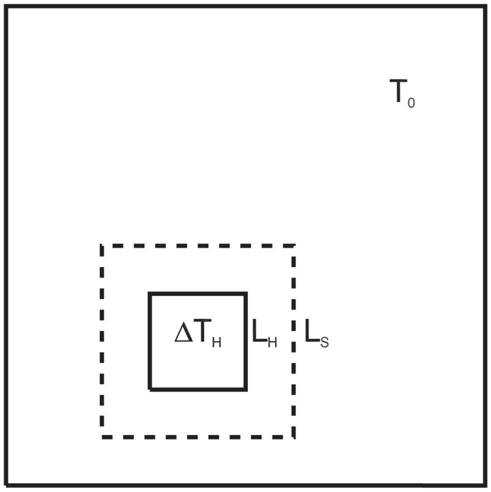

Figure 6.7 *Sketch of a square, thermal hotspot with temperature* $T_0 + \Delta T_H$ *and size* L_H^2. *The box evaluated by the sensor includes the hotspot with size* $L_s^2 > L_H^2$.

The assumed hotspot area increases as z^2, while the estimated temperature difference relative to the background decreases at the same rate. The question is how the PMRTD-estimated detection range will vary with increasing z. As indicated by the previous plots presented in this section, the answer to this question depends on several parameters. Fig. 6.8 shows the detection range as a function z, normalised by the detection range at $z = 1$. The Jim Compact WFOV camera properties are assumed in combination with MRTD parameters $\Delta T_{\text{min}} = 0.015$ K, $\Delta T_N = 0.25$ K, $x_c = 1.8$, and the extinction coefficient is assumed to be 0.5 (panel **a**) or 4.0 (panel **b**). Results are shown for L_H equal to 0.2 m (dark shading) and 5.0 m (bright shading), and for ΔT_H equal to 4 K (blue curves), 15 K (red curves) and 40 K (green curves). For small to medium atmospheric extinction levels, the estimated detection range for the smaller target increases (almost) linearly with increasing z. This is in particularly true when the hotspot temperature difference is large. The corresponding results for the larger target shows only a weak dependence on z. This means that unless the extinction is sufficiently large, the primary parameter which restricts the detection range is the target size.

If instead the atmospheric extinction is large, the PMRTD-estimated detection range is less prone to increase with increasing estimated hotspot area. As shown in panel **b** of Fig. 6.8, the estimate detection range actually decreases with increasing z for the case of the larger hotspot (dark shaded curves). If the hotspot temperature difference is 4 K, the estimate detection range drops by almost 50% if the hotspot critical size is estimated to be 20 m instead of the correct size of 5 m. Considering the smaller target, the estimated detection range still increases with increasing z. For example, the calculated detection range is doubled if the hotspot critical size is assumed to be

0.8 m rather than 0.2 m and the hotspot temperature difference is 15 K. If on the other hand, the temperature difference is merely 4 K, the estimated detection range is only 60% higher if $z = 4$ compared to the $z = 1$ case.

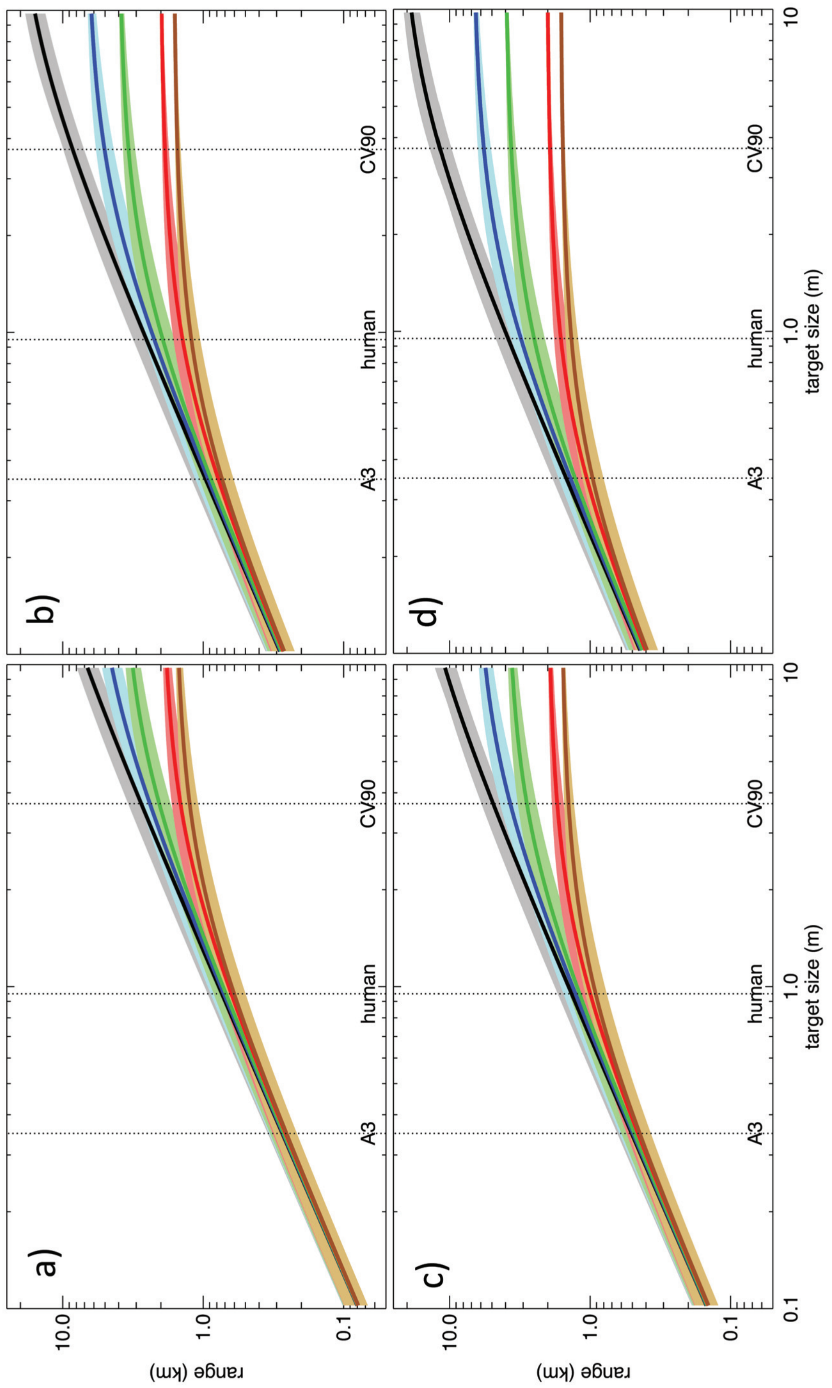

Figure 6.4 PMRTD-estimated range for 50% successful detection as a function of target size when $\Delta T_0 = 2$ K. Panels **a**, **b**, **c**, *and* **d** *show results using the FLIR A655SC, FLIR A655MAG, Jim Compact WFOV, and Jim Compact NFOV, respectively. The extinction coefficient (γ) is assumed to be 0.2 (black), 0.7 (blue), 1.2 (green), 2.3 (red), and 3.0 (brown). Uncertainty in estimates due to uncertainties in MRTD parameters (as in Fig. 6.3) is indicated by the thickness of the shaded regions.*

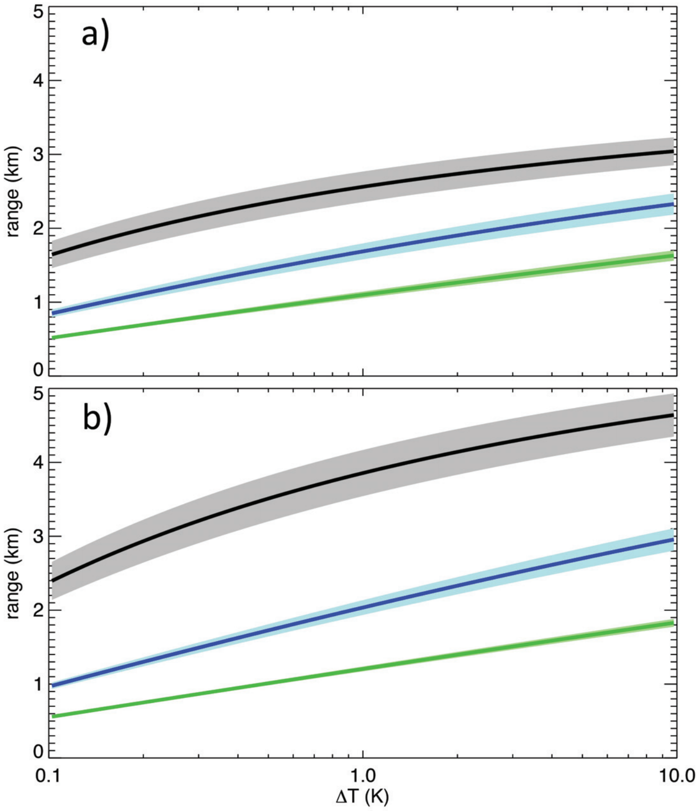

Figure 6.5 PMRTD-estimated range for 50% successful human detection as a function of target-background temperature difference using the FLIR A655MAG system (panel **a***) and Jim Compact binoculars on maximum zoom (panel* **b***). MRTD parameters are $\Delta T_{min} = 0.015$ K, $\Delta T_N = 0.25 - 1.0$ K, and $x_c = 1.8$. The extinction coefficient (γ) is assumed to be 0.2 (black), 1.0 (blue), 3.0 (green).*

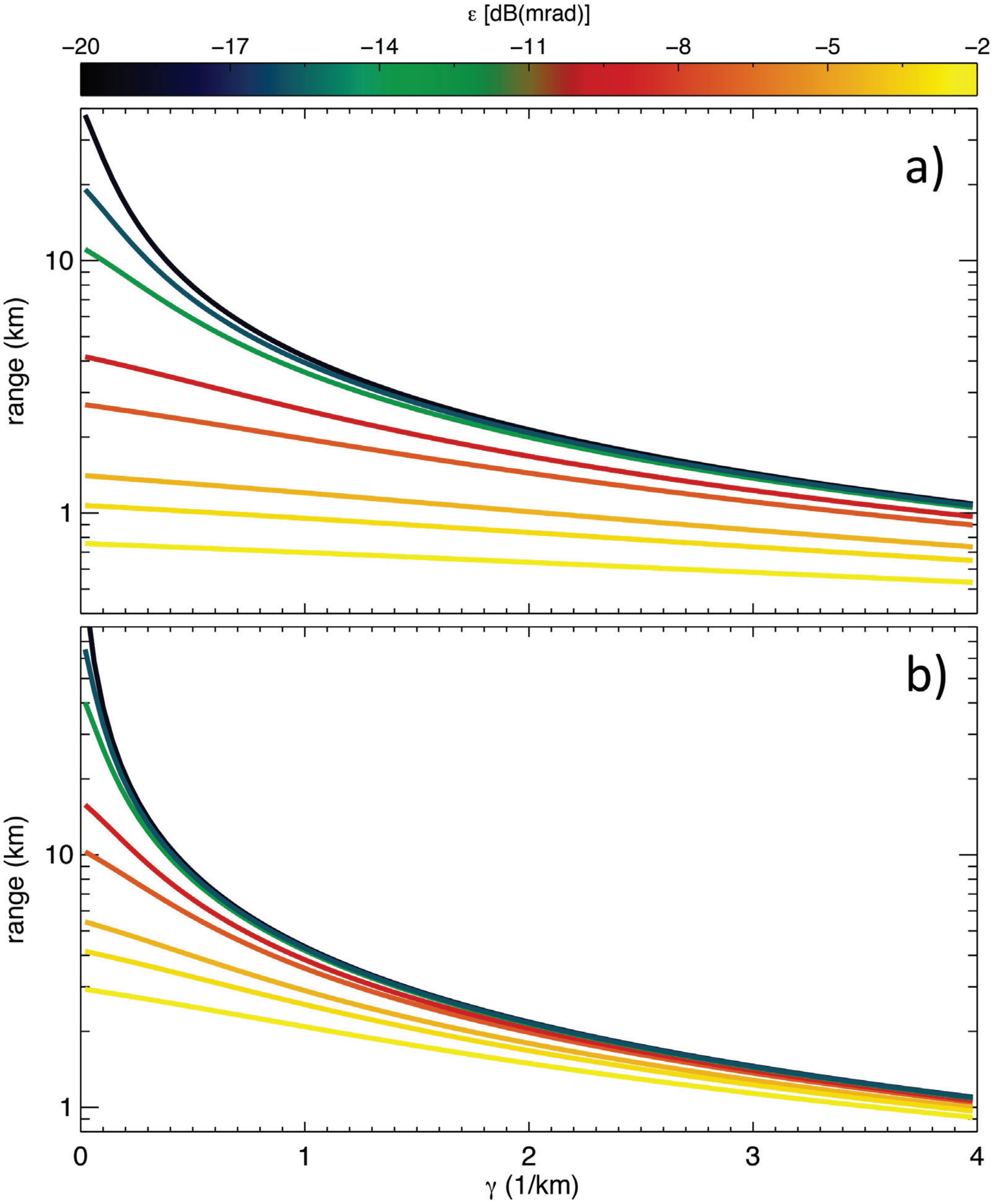

Figure 6.6 PMRTD-estimated range for the detection of a human (panel **a***) and a CV90 (panel* **b***) with* $\Delta T_0 = 2$ *K and a success rate of 50% plotted as a function of the extinction coefficient (*γ*). With one curve for each of the systems listed in Table 3.1, the colour indicates the IFOV on a dB(mrad) scale. MRTD parameters are* $\Delta T_{min} = 0.025$ *K,* $\Delta T_N = 1.0$ *K, and* $x_c = 2.0$*.*

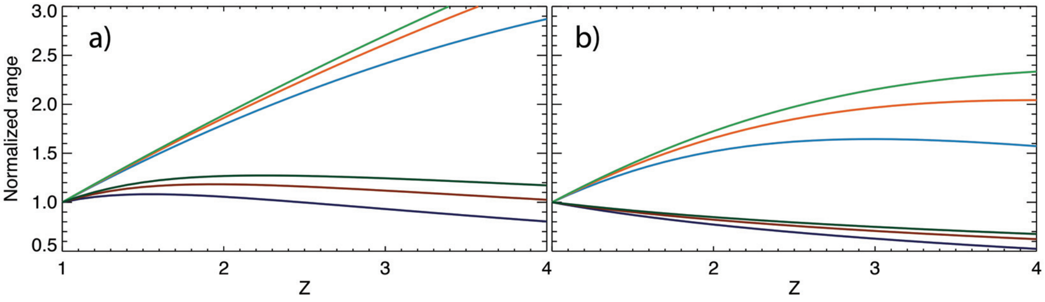

Figure 6.8 *Normalized PMRTD range for 50% successful hotspot detection as a function of the estimated-to-actual hotspot area ratio. Results are shown for* γ *equal to 0.5 (panel* **a***) and 4.0 (panel* **b***). Curves are shown for* L_H *equal to 0.2 m (dark shading) and 5.0 m (bright shading), and* ΔT_H *equal to 4 K (blue curves), 15 K (red curves) and 40 K (green curves).*

7 Practical examples of thermal acquisition range estimation

We have, in sections 4 and 6.3, described two different methods for estimating the acquisition range of thermal sensors. The first method, the pixels-on-target (POT) method, neglects atmospheric attenuation and assumes that the sensor limitations can be described by the Nyquist frequency alone. The acquisition range according to the POT method is given by Eq. 4.4. The second method, parameterised MRTD (PMRTD), incorporates atmospheric attenuation, albeit using a simplified atmospheric transmission model. In addition, PMRTD requires information (determined either from experiments or through an educated guess) regarding the detectable temperature difference as a function of target frequency. For all 3 sensors considered in this section, we will assume the following PMRTD parameters: $\Delta T_{\text{min}} = 0.015$ K, $\Delta T_N = 0.25 - 1.0$ K, and $x_c = 1.6 - 2.0$. The PMRTD estimated acquisition range normalised by the corresponding POT range estimate is given by Eq. 6.9 (or Eq. 6.7 if zero atmospheric attenuation is assumed). The thickness of the graphs showing PMRTD estimates reflects the uncertainty in the MRTD parameters. In this section, we will illustrate the use of the two methods on a handful of real-world scenarios. We will highlight the differences in estimated range between the two methods under varying conditions. A detailed explanation on how atmospheric parameters such as temperature, relative humidity, aerosol model, meteorological visibility and precipitation affects the atmospheric extinction is found in Appendix A.

7.1 Detection of a single, static person in rural, winter conditions

First, we revisit the classic task of detecting an isolated, static person with 50 % probability. We will restrict ourselves to winter conditions and assume that the person is completely separated from other heat sources so that the background temperature is uniform and equal to the air temperature. Just as in section 2.3, we will assume the person to be roughly 1.8 m tall and 0.5 m wide, resulting in a critical size of about 1 m. The person is otherwise assumed to wear relevant winter clothing (retail or military outfit). In addition to considering a full length person as a target, we will make a separate evaluation of a scenario where only the face is visible. Based on anthropometric data in Dreyfuss (1967), we assume the critical length of the exposed part of an average face to be about 15 cm. Despite being a much smaller target than a full length body, this configuration, unlike in the first case, is assumed to expose uncovered skin which indicates a much higher temperature difference than the full length target.

From Gavhed et al. (2000), we have that observed facial skin temperature relative to the surroundings increases from about 12 °C at ambient temperature 20 °C to about 28 °C at ambient temperatures below -5 °C. By fitting this data to a simple second order polynomial, we can for instance estimate the temperature difference between facial skin and the surroundings to be roughly 17 °C, 25 °C, and 27 °C when the ambient temperature is 10 °C, 5 °C, and 0 °C, respectively. In comparison, experimental data has shown that the temperature difference between a body covered by suitable winter clothing and its surroundings can be expected to be about 5 °C at ambient temperature -25 °C. We will furthermore assume that the temperature difference between the clothes and the background is more or less zero at ambient temperature 10 °C or higher.

We assume that the relative humidity is at 80% and that the atmospheric aerosol mixture is given by the rural aerosol model described in section A.2.1. We will look at two different cases when it comes to precipitation: one scenario without any precipitation and one scenario where the precipitation rate is set to 1.0 mm/hr. Furthermore, we assume that the precipitation comes in the form of rain when the ambient temperature is positive and in the form of snow when the ambient temperature is negative. The attenuation models in the two cases are described in sections A.3.1 and A.3.2, respectively. Snow results in much higher extinction than rain assuming the same precipitation rate, as can be seen by comparing Figs. A.8 and A.9. This will cause the total atmospheric extinction in these scenarios to drop markedly when the temperature goes from negative to positive. The aerosol concentration is in all cases set so that the visibility is limited to 20 km in the zero precipitation case. With a precipitation rate of 1.0 mm/hr, Tables B.6 and B.31 show that the extinction due to rain will be roughly 0.4 1/km in the MWIR and slightly bigger in the LWIR bands. Using Eq. A.20, we find that this should result in a combined visibility of around 6.5 km. In case of a 1 mm/hr rate of snowfall, the atmospheric extinction will be completely dominated by the precipitation. According to Fig. A.9, the extinction will be a little over 2 1/km in the MWIR band and just over 3 1/km in the LWIR band.

Fig. 7.1 shows the estimated detection range for the two configuration of the target as a function of the ambient temperature, for 3 different sensor systems: FLIR A655MAG (**a**), Safran Jim Compact NFOV (**b**), and Hensoldt Z:NightOwl® (**c**). The dashed lines show the POT estimate for the two configurations, which does not depend on atmospheric conditions or target-bakcground temperature differences. The red and blue curves represent the detection range for the full length person target in dry weather and with 1 mm/hr precipitation, respectively. Since the precipitation is assumed to be snow only for sub-zero temperatures, the detection range increases sharply at 0 °C ambient temperature in the precipitation case, but not in the dry weather case. The detection range for configuration 2, where the target is only a face, is mostly about 10 times smaller in dry weather than the corresponding detection range for the full length configuration. The only dry weather deviations from this is if the ambient temperature increases to nearly 10 °C, at which point the target-background temperature difference in configuration 1 approaches zero. The difference in estimated detection range between the dry and wet atmospheric case is much less for configuration 1 than it is for configuration 2. This is particularly evident for the Z:NightOwl® sensor, which has the longest detection range of the 3 sensors compared. This is consistent with the general rule that the target-sensor combination which provides the longest detection range, will also be most affected by non-ideal atmospheric conditions such as rain or snow.

7.2 Drone detection

Drone detection has become a highly relevant issue in recent years. We will consider detecting a drone with 70 % probability under different atmospheric conditions but with fixed relative humidity to 80%. It should be stressed that the detection range strictly speaking only applies to a static drone being detected under the condition of no observation time limit. Detection is done using the Safran Jim Compact sensor and we start out by assuming maximum zoom has been applied, as this gives the highest theoretical range but also the range most sensitive to atmospheric conditions. It will, however, be difficult to detect a drone which approaches from an unknown direction on full zoom without combining a large number of such sensors in order to achieve sufficient sensor coverage of the sky. In practise, it is therefore likely that an intermediate zoom needs to be chosen and that the practical detection range therefore will be considerably smaller than that reported in this section.

We will consider two different drone sizes; a medium-sized drone, with a critical length of about 35 cm, and a larger drone, with a critical length of 100 cm. A commercial example of the first kind is the popular DJI Phantom 4 (SZ DJI Tech. , 2020), while an example of the second type is the Griff 135 from Griff Aviation (Griff Aviation, 2020). The ambient temperature is set to 10 °C and the temperature difference between the targets and the background i assumed to be 20°C. Detection range for the two targets is plotted as a function of rain rate in Fig. 7.2. The red and green curves show the PMRTD estimate for the larger drone assuming the urban and maritime aerosol models, respectively. The corresponding range for a 35 cm-sized drone is shown in brown (urban) and blue (maritime). Referring to the zero precipitation case, the meteorological visibility is either 20 km (panel **a**) or 2 km (panel **b**). The dashed lines, black and grey, show the POT estimate for the two drone sizes, large and medium, respectively. Because the POT estimate does not take into account atmospheric conditions, these estimates are identical in the two panels.

The detection range for the larger drone is between 2 and 4 times larger than the corresponding detection range for the smaller drone. The difference is at its largest in good atmospheric conditions; most importantly that there is negligible precipitation. Visbility also plays a role, but much less than in visible light and mostly when considering the larger drone in combination with the maritime aerosol model. In this case, the detection range can be seen to increase from around 3 km to 4 km when the visibility is increased from 2 km to 20 km. Rainfall up to 4 mm/hr causes the detection range to drop by 20-25%, and if the rain rate increases to10 mm/hr the drop relative to the zero-precipitation case has increased to 30-35% in total. For the smaller target, there is negligible effect of the atmospheric conditions on the detection range, and it is typically 10-30% larger than the POT estimate for this target.

7.3 The effect of emissivity on the detection of tents

So far, we have assumed only ideal, black-body radiation in these practical examples. Real materials exhibit deviations from black-body behaviour which normally are expressed using the concept of emissivity (ε), the ratio of the thermal radiance from a material surface and the radiance from a black-body with the exact same temperature as the material surface. While the emissivity can be expected to vary with wavelength, we argued in section 1 that a useful simplification approximates the emissivity as a constant near the wavelength of peak radiance. Eq. 1.6 relates the measured surface temperature to the emissivity of the material and the true temperature. Tents will tend to be warmer than its surroundings because of the heating mechanisms utilized by a tent, in combination with potential heating sources inside the tent. It can therefore be desirable from a signature point-of-view to use a tent material with a lower emissivity than that of the background. A detailed review of different approaches to modifying the emissivity of tent materials is found in Hall (2017). The author also presents emissivity data on woven polyester tent fabrics. Untreated fabrics exhibit an emissivity of over 0.8, while fabrics coated to a various degree with aluminium coating, have a measured emissivity of between 0.2 and 0.7.

7.3.1 Apparent temperature differences

How much smaller the tent emissivity ideally should be, really depends on the real temperature difference between the tent and the background. If the tent emissivity gets too low, the tent will appear to be noticeably colder than the background. If, for instance, the background is dominated by vegetation, the emissivity of the background will be 0.9-1.0 (Brewster, 1992). A tent emissivity of less than 0.9 would then potentially improve the tent's camouflage properties, assuming the tent is warmer than its surroundings. In Fig. 7.3, we have illustrated this problem for two temperature scenarios where the background is assumed to have a fixed emissivity of 0.9. In the first scenario, indicated by the blue curves in Fig. 7.3, the true ambient temperature is -15 °C which is equivalent to an apparent temperature of about -20 °C. The true tent temperature in this case is assumed to be 10 °C, which means that the true temperature difference between the tent and the vegetation in this scenario is 25 °C (indicated by the blue, dashed line in Fig. 7.3). Because the apparent tent temperature depends on the tent emissivity, the measured temperature difference between the tent and the background will also vary with emissivity. Inspecting the blue , solid curve in Fig. 7.3, we see that the apparent temperature difference drops as the tent emissivity drops below 0.9, until it reaches roughly 0 at $\varepsilon = 0.56$. This can according to Hall (2017) be achieved by coating the tent fabric with 9 μm at a wet weight of 5 %. That the tent can be made to blend perfectly with the background by simply tailoring the emissivity comes directly as a consequence of the simplifying *grey body* assumption. In reality though, there will always be a certain level of thermal mismatch between an artificially made target and a natural background. If the tent emissivity is decreased below 0.56, the measured temperature difference between the tent and the background starts to increase, this time with the tent being the colder component, until it reaches 30 °C when $\varepsilon = 0.3$.

In the second scenario, indicated by the red curves in Fig. 7.3, the ambient temperature is +15 °C which is equivalent to an apparent temperature of about 9 °C. The true tent temperature is assumed to be 20 °C, making the true temperature difference between the target and the background 5 °C. In this case, the two apparent temperatures become equal if the tent emissivity is about 0.82, as seen in Fig. 7.3. This corresponds to the emissivity level measured by Hall (2017) of untreated, woven polyester. If on the other hand, the tent emissivity is reduced all down to 0.3, the measured temperature difference between the tent and the background will have increased to over 50 °C. For such a scenario, the biggest risk from a signature perspective is to have a too low rather than a too high tent emissivity.

7.3.2 Detection range as function of emissivity

We have seen how the measured temperature difference between a target, in this case a tent, and the background varies with varying target emissivity for two temperature scenarios. The next question is how the detection range can be expected to be influenced by modifications to the target emissivity. To answer this, we adopt the same two temperature cases used in the previous section, now referred to as a *winter* and a *summer* scenario, and a background with the same, fixed emissivity as before of 0.9. We will consider 3 different atmospheric conditions, but the relative humidity will be set to 90 % and the *rural* aerosol model is chosen for all 3 atmospheres. We are interested in detection with a probability of success rate of 50 %, and consider data aquisition using 3 different sensors: the Safran Jim Compact WFOV, the Safran Jim Compact NFOV, and Hensoldt Z:NightOwl®, hereafter referred to as sensors 1-3.

The first case assumes good weather conditions with a meteorological visibility of $V = 20$ km and no precipitation. Fig. 7.4 shows the estimated detection range as function of tent emissivity, with the results for sensors 1, 2, and 3 identified by squares, circles, and triangles, respectively. The blue graphs correspond to the winter scenario, while the red graphs shows the results for the summer scenario. For sensors 1 and 2, the difference between the winter and summer scenarios is small, with the winter detection range being about 2 % and 9 % larger, respectively. The emissivity-averaged detection range is estimated to be just under 5 km for sensor 1 and 14-15 km for sensor 2. For the last sensor, the difference between the detection range in the two scenarios is larger, almost 30 %, with an emissivity-averaged detection range of 40 km in the summer scenario and almost 65 km in the winter scenario. The reason why the winter scenario results in a larger detection range is not primarily because the true temperature difference is 4 times larger in the winter scenario, but because the atmospheric attenuation in a high-humidity atmosphere is noticeably smaller when the ambient temperature is 30 degrees lower.

Just as the measured temperature difference was shown in Fig. 7.3 to reach a minimum at $\varepsilon = 0.56$ for the winter scenario and $\varepsilon = 0.82$ for the summer scenario, the detection range graphs in Fig. 7.4 exhibit dips at the appropriate emissivity values. According to the model, the sensor 3 detection range can be expected to drop to 40 km in the winter scenario and 12 km in the summer scenario if the emissivity is tailored to the scenario. For sensor 2, the corresponding detection ranges are 10 km and 5 km. Although this result should be qualitative correct, the quantitative strength of these dips depends on how much the emissivity varies with frequency within the sensor wave bands.

In the second atmospheric case, there is still no precipitation but the visibility is assumed to have dropped to 2 km. The detection range for this case is shown in Fig. 7.5. For sensor 1, the change of visibility has almost no effect on the detection range. This is because the sensor optics is the primary limiting factor. Even for sensor 2, the changing atmosphere does not have a big impact, giving ony about 30 % reduction in the estimated detection range. For sensor 3, on the other hand, the reduction in the meteorological visibility causes a major drop in estimated detection range, dropping from 65 km (winter) and 40 km (summer) to 23 km (winter) and 18 km (summer). For the last calculations, we return to an atmosphere with $V = 20$ km. This is assuming no precipitation. Then, we add 1 mm/hr precipitation, which falls as rain in the summer scenario and as snow in the winter scenario. As is shown in Fig. 7.6, the snow in winter has a considerably stronger effect on the detection range than the rain in summer. In the winter scenario, there is almost no difference in the performance between the three sensors, with a detection range of around 2.5 km. For the summer scenario, there is still some difference in the performance of the three. Sensor 1 is almost unaffected by the light rain since the detection range is so small even in dry weather. For sensor 2, the detection range is about 10 km on average, slightly smaller than the corresponding detection range in the previous atmospheric case. The same is more or less true for sensor 3, where the emissivity-averaged detection range in this case is just under 15 km.

7.4 Comparison of detection range for compact ICE and BEV cars

The last example explores a new vehicle trend and how it might affect thermal detection. The power train transition from internal combustion engine (ICE) to battery electric vehicles (BEV). BEVs is gradually making an inroad in some markets and is expected to accelerate in the next 5-10 years. So far, BEVs are virtually non-existing in military applications, but they are expected to play a role in future military operations, in particular if you include plug-in hybrids (PHEVs) which can operate completely on the electric motor for a meaningful period of time. An example of the latter is the Scarabee presented by Arquus Defence in 2019 (Arquus, 2019), a light armoured 4X4 vehicle designed for reconnaissance, scouting and support. Apart from innovative modes of movement due to separate motors on each wheel, the electric operation should offer possibilities for reduced signature. It is expected that a BEV would radiate less heat than an ICE vehicle due to a more efficient power train. This was clearly demonstrated by the Youtube channel **Fully Charged** which used a FLIR T1K HD camera to compare the thermal signature from two compact cars, a Nissan Leaf (electric) and a Ford Focus (diesel) (Czerski, 2019). The measured temperatures of various parts of the BEV is generally substantially smaller than that of the ICE vehicle. But there are also indications in the video that the low emissivity of the body of the cars will complicate this picture. Assuming the cars are observed in daytime and given the right weather conditions, reflected sunlight can make parts of a car look hotter, even when the car is not turned on. This effect can prevent the temperature difference between for instance a BEV and the surrounding vegetation from becoming very small. In nighttime or in cloudy weather, this effect should be negligible and the difference in thermal signature between a BEV and an ICE vehicle is expected to be more pronounced.

Based on the measurements in (Czerski, 2019), the following scenario is set up. Detection with a probability of 50% from the front and from the side is considered.The two cars are of roughly of the same size the Nissan Leaf and Ford Focus, and the critical length for front detection is estimated to 1.3 m, while the critical length for side detection is set to 2.0 m. The ambient temperature is set to 12 °C, the relative humidity is again set to 80%, the rural aerosol model is assumed, no precipitation is included, and the background is assumed to be dominated by vegetation and soil so that the emissivity of the background is fairly close to unity. Due to the low emissivity of the body of the cars, and since the BEV has limited heat production in itself, the BEV-background temperature difference is expected to be lower at night and low light than in broad daylight. We will therefore consider both a daytime and a nighttime scenario. This is not expected to play a role for the detection of the ICE vehicle. The BEV is estimated to have a day-time temperature difference relative to the background of about 1 °C, both in front and on the side. At night, this temperature difference is assumed to be reduced to roughly 0.1 °C (this is a loosely based estimate). The ICE vehicle exhibits a larger temperature difference with its surroundings, in particular in the front. The front temperature difference is estimated to 10 °C although parts under the hood have much higher temperatures. On the side of the car, the temperature difference is estimated to be reduced to 6 °C. The same temperature differences are assumed to apply at night.

In Fig. 7.7 we show the estimated detection range for 4 different targets: frontal BEV (red curves), frontal ICE (brown curves), sideways BEV (blue curves), and sideways ICE (green curves), all plotted as functions of the meteorological visibility. The dashed curves show the POT-estimated detection range for the frontal and sideways targets, and results are shown for the daytime (panel **a**) and nighttime (panel **b**) scenarios. For all the PMRTD estimates, the visibility plays an important role if it gets sufficiently small, below around 2 km where the fog models start to come into effect. In the high visibility regime, how much the range estimates depend on the visibility is dependent on the target characteristics. The detection of the frontal ICE vehicle is least sensitive to variation in the visibility in the medium-to-high visibility regime. This is because it exhibits the largest temperature difference relative to the background and is the smaller of two geometries. This makes the sensor resolution the most important parameter. While the detection range for the frontal ICE target increases by less than 10 % when the visibility increases from 2 km to 20 km, the corresponding increase for the sideways BEV is roughly 24 % in the daytime scenario. In this case, the temperature difference between target and background is small, in addition to the critical length being slightly larger than for the two frontal targets. In the nighttime scenario, the sideways BEV detection range increases by almost 50 % as the visibility goes from 2 km to 20 km since the temperature difference is even smaller in this case.

To summarise the results presented in Fig. 7.7, we can say that changing the detection orientation from frontal to sideways typically increases the estimated detection range with slightly less than 20

% when the visibility is as low as 1 km, while the frontal-to-sideways increase is almost 50 % when the visibility is 20 km. So how much larger is the detection range for an ICE vehicle compared to a BEV? This depends on the visibility and whether it is the day or night scenario. During the day, the ICE detection range is almost 20 % larger than the corresponding BEV detection range when we are in the high visibility regime. If the visibility is reduced to 1 km the detection range of an ICE vehicle is estimated to be about 40 % larger than the BEV detection range. Note, that this is during daytime when we expect low-emissivity effects to contribute to the apparent temperature difference between a BEV and its surroundings. In the nighttime, when we have assumed that the BEV-background temperature difference has been reduced by a factor 10, the thermal detection range for an ICE vehicle is predicted to be almost twice the detection range of the corresponding BEV target.

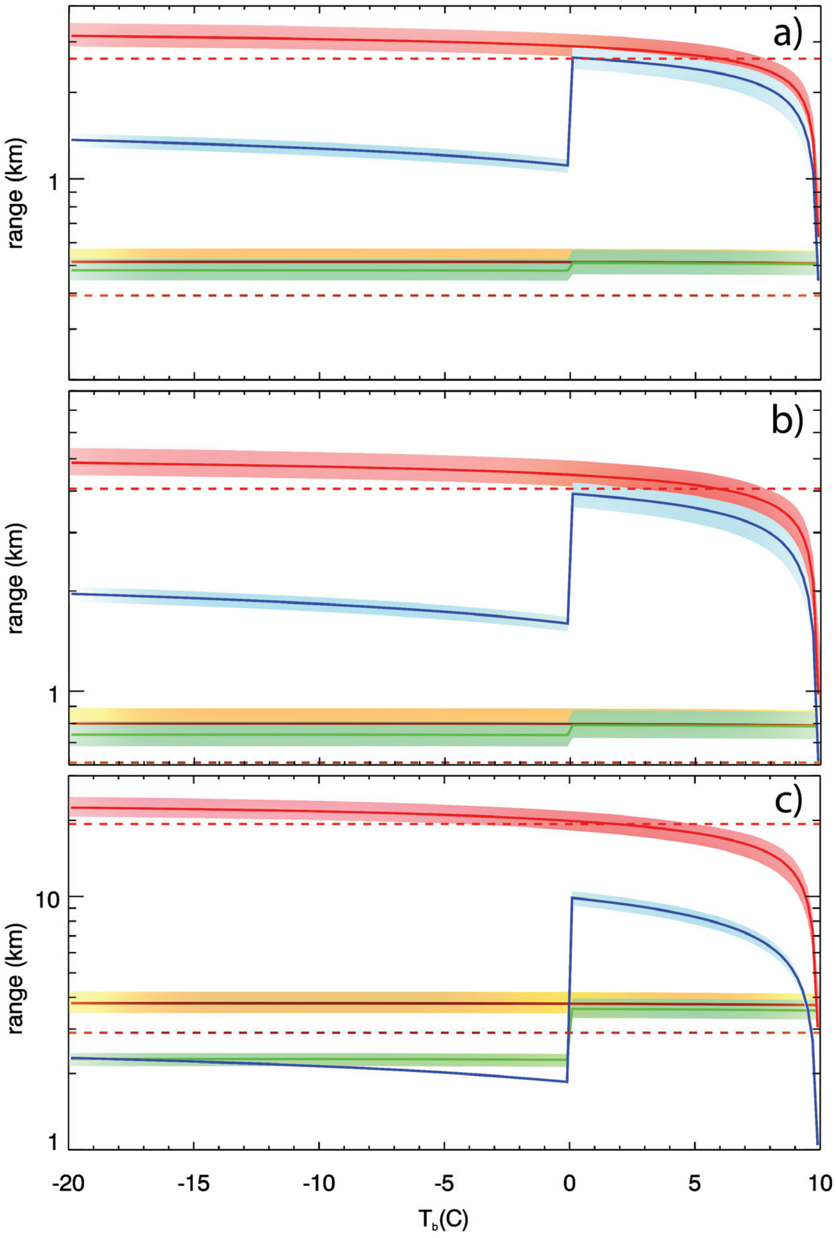

*Figure 7.1 Estimated range for 50 % probability of detecting a static person either as a full length body (configuration 1) or as a face only (configuration 2) as function of background temperature. The dashed lines show the POT estimate for the two configurations. The red and orange curves show the PMRTD estimate with no precipitation in configuration 1 and 2, respectively. The blue and green curves show the corresponding results with 1 mm/hr precipitation. Results are shown for the sensors FLIR A655MAG (**a**), Safran Jim Compact NFOV (**b**), and Hensoldt Z:NightOwl$^{®}$ (**c**).*

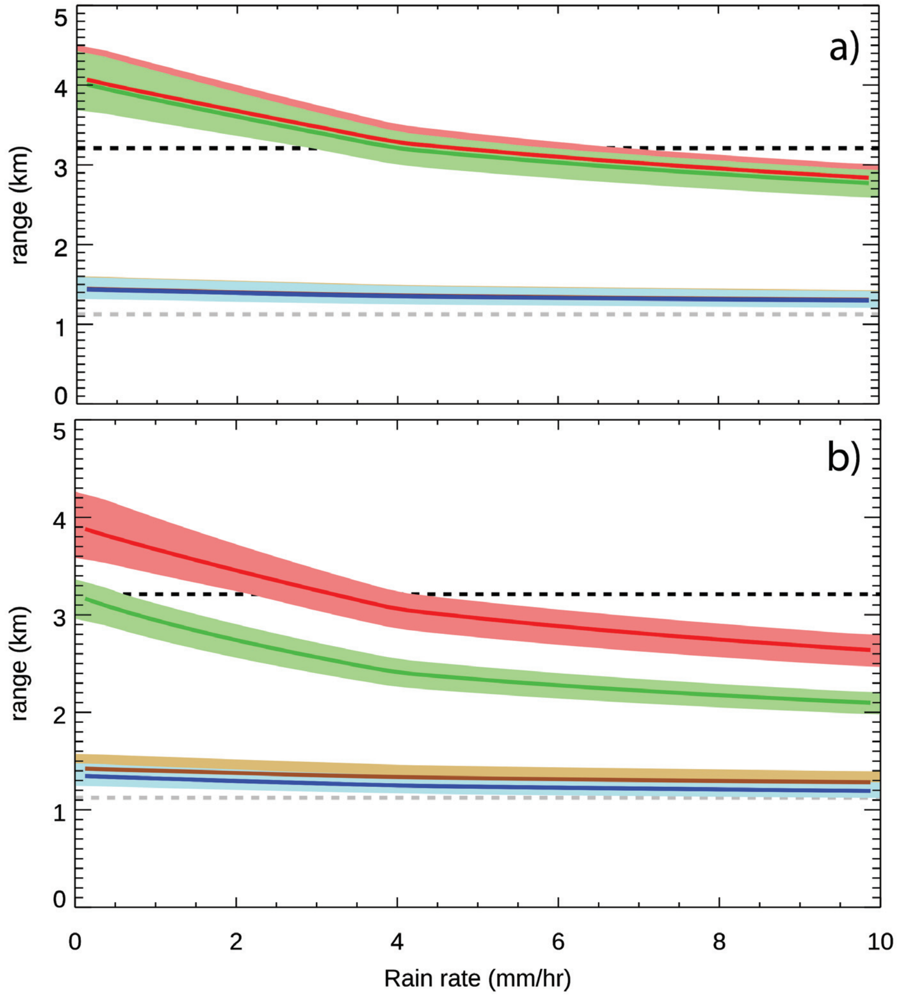

Figure 7.2 *Estimated range for 70 % probability of detecting a static drone when the meteorological visibility equals 20 km (panel* **a***) and 2 km (panel* **b***) as a function of rain rate. The red and green curves show the PMRTD estimate for the 100 cm-sized drone assuming the urban and maritime aerosol models, respectively. The corresponding range for a 35 cm-sized drone is shown in brown (urban) and blue (maritime). The dashed lines show the POT estimate for the two drone sizes and is identical in the two panels.*

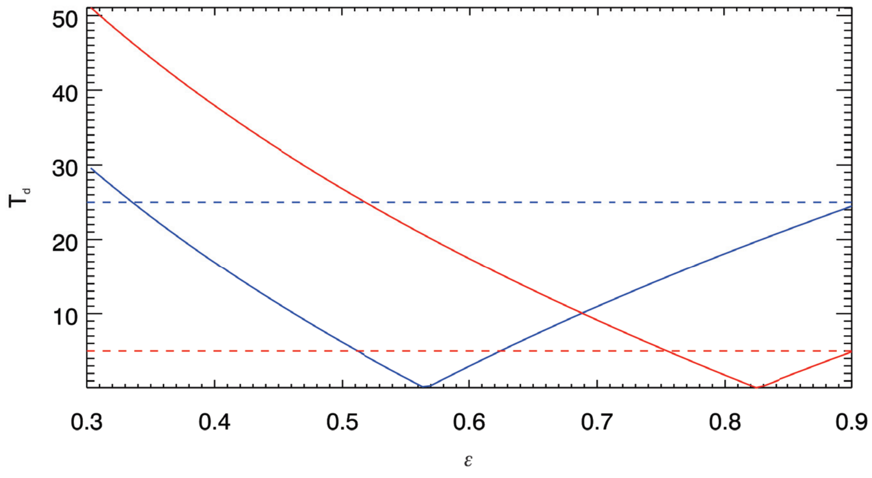

Figure 7.3 Apparent temperature difference between a tent and the background as a function of the tent emissivity in two separate scenarios, where the real tent temperature is 10 °C (blue) or 20 °C (red) and the corresponding background temperature is -15 °C (blue) or 15 °C (red).

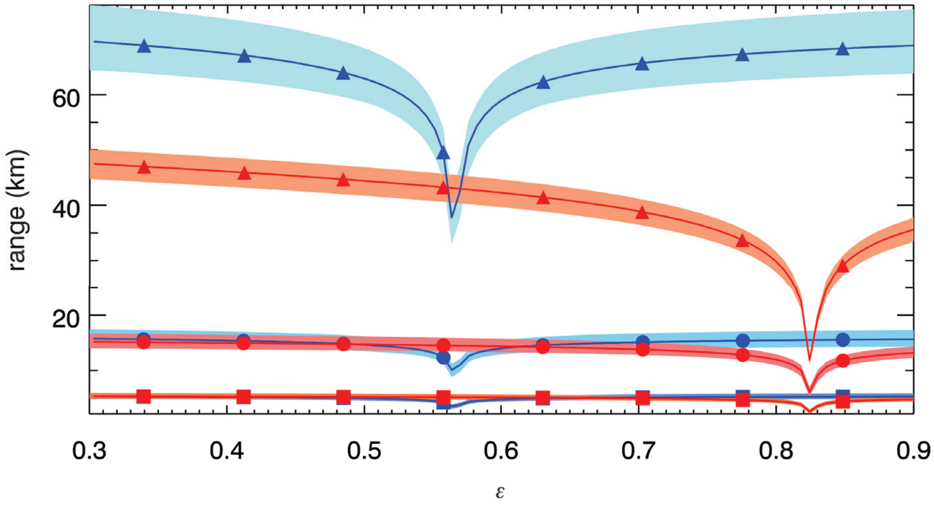

Figure 7.4 Detection range as a function of tent emissivity for the winter (blue) and summer (red) scenarios with meteorological visibility $V = 20$ km and no precipitation when using one of the 3 sensors: Safran Jim Compact WFOV (squares), Safran Jim Compact NFOV (circles), or Hensoldt Z:NightOwl® (triangles).

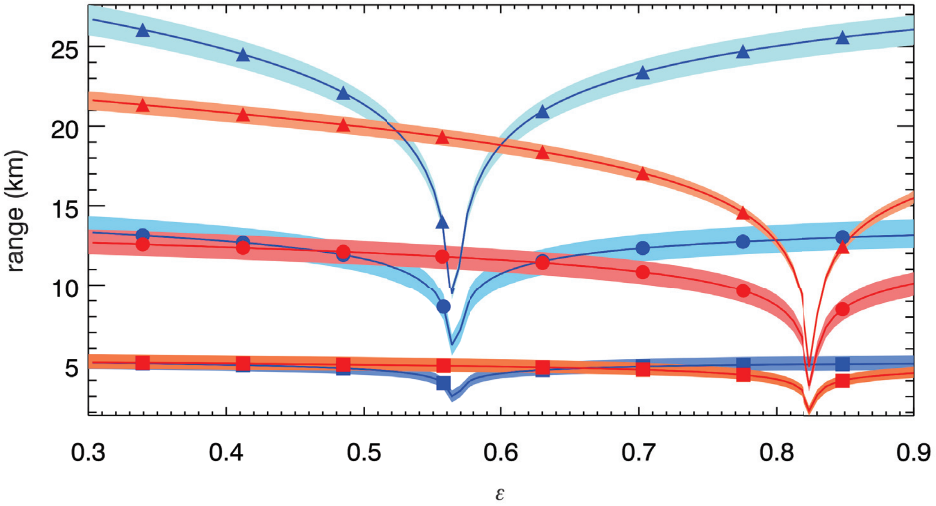

Figure 7.5 Detection range as a function of tent emissivity for the winter (blue) and summer (red) scenarios with meteorological visibility V = 2 km and no precipitation when using one of the 3 sensors: Safran Jim Compact WFOV (squares), Safran Jim Compact NFOV (circles), or Hensoldt Z:NightOwl$^{®}$ *(triangles).*

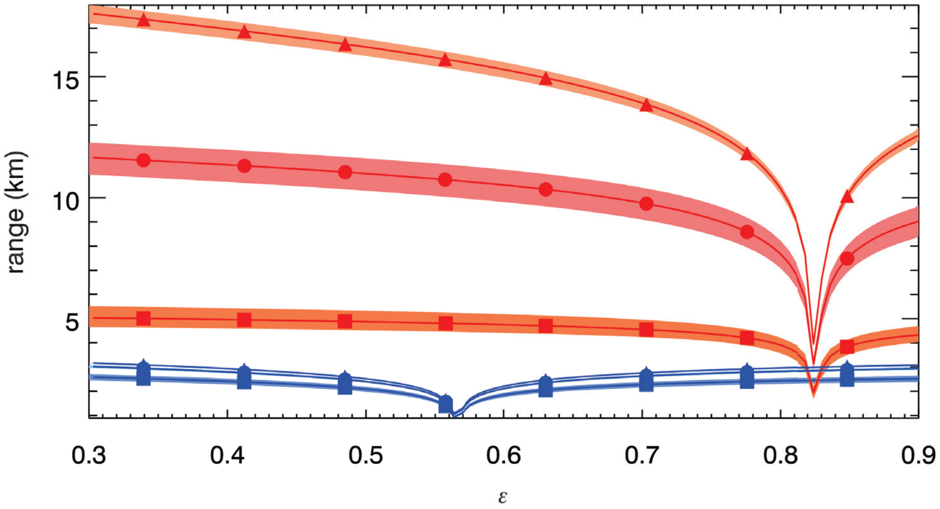

Figure 7.6 Detection range as a function of tent emissivity for the winter (blue) and summer (red) scenarios with meteorological visibility V = 20 km and 1 mm/hr precipitation when using one of the 3 sensors: Safran Jim Compact WFOV (squares), Safran Jim Compact NFOV (circles), or Hensoldt Z:NightOwl$^{®}$ *(triangles).*

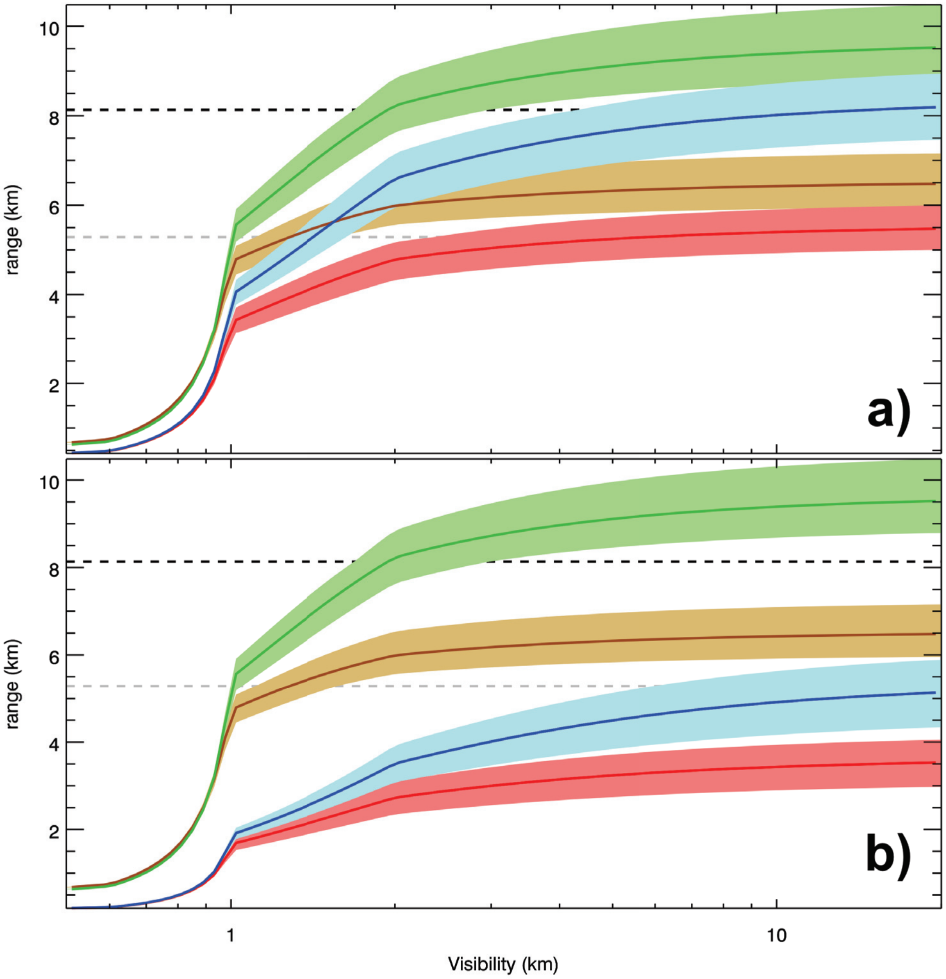

Figure 7.7 Estimated 50 % probability detection range as a function of visibility for a compact-sized BEV and a similar ICE vehicle. Range estimation is performed both for a daytime (panel **a***) and a nighttime (panel* **b***) scenario. The vehicles have either the front (red/brown curve for the BEV/ICE) or the side (blue/green curve for the BEV/ICE) towards the observer. The dashed lines show the POT estimate for the front (grey lines) and the side (black lines).*

8 Summary

This report serves as an introduction to the topic of thermal acquisition range estimation by discussing camera-dependent properties, atmospheric effects, and to a limited extent, target-specific factors. We discuss the simple **Pixels-on-target (POT)** estimation method, as well as the more elaborate **Parameterized Minimum Resolvable Temperature Difference (PMRTD)** method. The latter method represents, as far as the author is aware, a new approach to utilizing the concept of MRTD-curves in range estimation. The new method has advantages both when it comes to estimating the acquisition range itself as well as estimaging the uncertainty in the calculated range caused by uncertainties in the MRTD parameters. PMRTD, unlike POT, includes effects of atmospheric attenuation and requires a separate extinction model which has been constructed on the basis of experimental data from the literature (see Appendix A).

There are many different sources of errors and uncertainties which might affect the estimated aqcuisition range predicted by the PMRTD method in a given scenario. There are uncertainties associated with the model parameters which specify the MRTD-curve for the sensor being evaluated. There are also uncertainties associated with the atmospheric conditions and the target emissivity. Uncertainties in all these parameters can easily be reflected in the predicted acquisition range using the PMRTD method. In addition, there are uncertainties caused by spatial and temporal variations in the thermal properties of both the target and the background, as well as errors accumulated by the simplified radiation transfer model applied (see discussion on Beer’s law in section 5.3). It should also be stressed that all range estimates assume static targets being detected, identified or recognized by an observer with infinite observation time at his or her disposal. The effects that these uncertainties, or sources of errors, have on the predicted acquisition range cannot be estimated using PMRTD.

Unfortunately, we have not had access to data suitable for a rigorous validation and comparison of the two estimation methods presented in this report. However, practical examples were presented in section 7 which highlights the differences between the two methods in different scenarios. Typically, the POT method gives estimates consistent with the PMRTD estimates if the target-background temperature difference is large and the atmospheric conditions are reasonably good. If one of those conditions are not properly met, the POT method is likely to overestimate the acqusition range. However, the PMRTD estimated range can in some cases be larger than the POT estimated range. This is due to the difference between the practical and theoretical upper limit to detecting high-frequent targets.

References

Arquus Defense **Scarabee innovative prototype**, www.arquus-defense.com/scarabee-innovative-prototype, 2019

Baranov, Y.I. **Water-vapor continuum absorption in the 800-1250 cm^{-1} spectral region at temperatures from 311 to 363 K**, J. Quant. Spectrosc. Radiat. Transfer, 109, 2291-2302, 2008

Berk, A. & Hawes, F. **Validation of MODTRAN®6 and its line-by-line algorithm** , J. Quant. Spectrosc. Radiat. Transfer, 203, 542-556, 2017

Bisyarin, V.P. et al. **Attenuation of 10.6 and 0.63 μm laser radiation in atmospheric precipitation**, Radio Eng. Electron. Phys., 16, 1594-1597, 1971

Borcan, O.V. & Spulber, C. **A contribution to the estimation problem of the detection performance with a thermal camera in different conditions of meteorological visibility**, Applied Mech. Materials, 436, 326-333, 2013

Børve, S. & Selj, G.K. **(U) Thermal signatures of SOF patrols in arctic winter conditions during exercise LAPWING**, Norwegian Defence Research Establishment (FFI), FFI-eksternnotat, 19/01439 (KONFIDENSIELT) 2019

Brewster, M.C. **Thermal radiative transfer and properties**, John Wiley & Sons, New York, 56-57, 1992

Buck, A.L. **New equations for computing vapor pressure and enhancement factor**, J. Appl. Meteorol., 20, 1527-1532, 1981

Clough, S.A. et al. **Line shape and the water vapor continuum**, Atmos. Res., 23, 229-241, 1989

Clough, S.A. et al. **Atmospheric radiative transfer modeling: A summary of the AER codes**, J. Quant. Spectrosc. Radiat. Transfer, 91, 233-244, 2005

Chrzanowski, K. **Testing Thermal Imagers**, Military Univ. Tech. Rep., Warsaw, 2010

Chu, T.S. & Hogg, D.C. **Effects of Precipitation on Propagation at 0.63, 3.5, and 10.6 Microns**, Bell Syst. Tech. J., 47, 723-759, 1968 de Villiers, M.P. & van Heerden, J. **Dust storms and dust at Abu Dhabi international airport**, Weather, 62, 339-343, 2007

Dreyfuss, D.D. **The Measure of Man - Human Factors in Design**, Whitney Library of Design, New York, 1967

FLIR Systems, Inc. **Seeing through fog and rain with a thermal camera**, www.flirmedia.com/security/technical-notes/fog-technical-note.html, 2019

FLIR Systems, Inc. **FLIR ResearchIR product description**, www.flir.eu/products/researchir, 2020

Czerski, H., **EV vs ICE vehicles: how much energy is wasted?**, Fully Charged Live (fullycharged.show/episodes/flir-t1k-thermal-camera), Austin, Texas, 2019

Gavhed, D. et al. **Face temperature and cardiorespiratory responses to wind in thermoneutral and cool subjects exposed to -10 °C**, Eur. J. Appl. Physiol., 83, 449-456, 2000

Goodell, J.B. & Roberts, R.E. **Atmospheric effects on infrared systems**, in "The Fundamentals of Thermal maging Systems", F. Rosell & G. Harvey (Eds.), Naval Res. Lab. Rep. 8311, Washington D.C., 21-48, 1979

Griff Aviation **The Griff Fleet**, www.griffaviation.com/the-griff-fleet, 2020

Hall, M.S. **Thermal Signature Management**, Master thesis, North Carolina State Univ., Raleigh, 2017

Hill, R.W. et al. **Thermal Imaging and Physiological Analysis of Cold-Climate Caribou-Skin Clothing**, Arctic, 73, 40-52, 2020

Holst, G.C. **Infrared Imaging System Testing**, in "The Infrared & Electro-Optical Systems Handbook. Volume 4: Electro-Optical Systems Design, Analysis, and Testing", M.C. Dudzik (Ed.), SPIE Optical Engineering Press, Bellingham, USA, 195-243, 1993

Howe, J.D. **Electro-Optical Imaging System Performance Prediction**, in "The Infrared & Electro-Optical Systems Handbook. Volume 4: Electro-Optical Systems Design, Analysis, and Testing", M.C. Dudzik (Ed.), SPIE Optical Engineering Press, Bellingham, USA, 55-120, 1993

Johnson, J. **Analysis of Image Forming Systems**, Proc. Image Intensifier Symp.,U.S. Army Eng. Res. Development Lab, Ft. Belvoir, AD 220-160, 249-273, 1958

Krapels, K. et al. **Minimum resolvable temperature difference (MRT): procedure improvements and dynamic MRT**, Infrared Phys. & Tech., 43, 17-31, 2002

Longtin, D.R. et al. **A Wind Dependent Desert Aerosol Model: Radiative Propoerties**, Air Force Geophys. Lab., Hanscom AFB (MA), AFGL-TR-88-0112, 1-116, 1988

Love, J. **The truth about range data: how to assess thermal camera range capability for site design purposes**, White Paper, DRS Technologies, Ottawa, 2017

NATO, STANAG 4347 **Definition of Static Range Performance for Thermal Imaging Systems**, NATO STANAG 4347, Washington DC, USA (1995)

Perić, D., et al. **Thermal Imager Range: Predictions, Expectations, and Reality**, Sensors, 19, 3313-3325, 2019

Paynter, D.J. & Ramaswamy, V. **An assessment of recent water vapor continuum measurements upon longwave and shortwave radiative transfer**, J. Geophys. Res., 116, D20302/1-13, 2011

Radke, R.J. et al. **Image Change Detection Algorithms: A Systematic Survey**, IEEE Trans. Image Processing, 14, 294-307, 2005

Ratches, J.A. **Static Performance Model for Thermal Imaging Systems**, Optical Engineering, 15, 525-530, 1976

Seagraves, M.A. **Precipitation rate and extinction in falling snow**, J. Atmos. Sci., 11, 1827-1835, 1984

Shettle, E.P. & Fenn, R.W. **Models for Aerosols of the Lower Atmosphere and the Effects of Humidity Variations on Their Optical Propoerties**, Air Force Geophys. Lab., Hanscom AFB (MA), AFGL-TR-79-0214, 1-99, 1979

Sanders-Reed, J.N. & Fenley, S.J. **Visibility in Degraded Visual Environments (DVE)**, SPIE Proc., 10642, 1-12, 2018

Shenzhen DJI Sciences and Technologies Ltd. **Phantom 4 Pro**, www.dji.com, 2020

tec-science.com **How does a thermal camera work?**, www.tec-science.com/thermodynamics/temperature/how-does-a-thermal-camera-work, 2019

Thomas, M.E. & Duncan, D.D. **Atmospheric Transmission**, in “The Infrared & Electro-Optical Systems Handbook. Volume 2: Atmospheric Propagation of Radiation”, F. Smith (Ed.), SPIE Optical Engineering Press, Bellingham, USA, 1-156, 1993

van Rheenen, A.D. et al. **Measurements of the effect of falling snow on imaging with infrared cameras**, SPIE Proc., 6395, 6395071-10, 2006

van Rheenen, A.D. et al. **MRTD – Man vs. Machine**, SPIE Proc., 10625, 1062501-12, 2018

Vinson, J., Driggers, R. & Deep, R. **Techniques and errors for apparent differential temperature calculations**, SPIE Proc., 3377, 1-10, 1998

A An atmospheric attenuation model

In section 6, we looked at how the MRTD function can be used to improve on the estimated thermal sensor acquisition range provided by the simple Pixels-on-target (POT) method (see section 4). One of the main differences between the two approaches is that the PMRTD method, in contrast to the POT method, takes atmospheric attenuation into account. The discussion in section 6 assumes that the strength of atmospheric attenuation is known and thereby belies the fact that estimating the wavelength-dependent dampening of electromagnetic signals through the air is in itself a challenging task. The accuracy of the range estimates will be determined, not only by the uncertainties in the sensor properties and the errors associated with the use of Beer's law (see section 5.3), but also by how well we can estimate the atmospheric attenuation in the frequency band we are interested in. MODTRAN® is an example of a well-established, commercial software which provides high resolution, line-by-line radiative transfer calculations through a stratified atmosphere (Berk & Hawes, 2017). The model includes 6 standard atmospheres (tropical, mid-latitude summer/winter, sub-arctic summer/winter, and US standard 1976) and 4 aerosol classes (rural, urban, navy aerosol, and desert).

In order to produce the quantitative examples of real-world scenarios described in section 7, we developed a separate atmospheric attenuation model. The aim of the model was to provide reasonably accurate extinction coefficients in the MWIR and LWIR frequency bands based on easily observable weather parameters (air temperature, humidity and meteorological visibility), and the model includes attenuation due to both water vapour and aerosols, including rain and snow. Although much simpler than MODTRAN®[3] and with much lower spectral resolution, the new model is build on much of the same raw data as MODTRAN®. In this section, the attenuation model is explained. First, we look at the separate sub-models before discussing how the they are combined. Appendix B provides tables with extinction coefficient values for a wide range of atmospheric conditions calculated using this attenuation model.

A.1 Gas attenuation model

Gas attenuation in the MWIR and LWIR atmospheric windows is usually less important than aerosol attenuation unless the visibility is very good or the climate is hot and humid. But while the aerosol attenuation, at least as it pertains to fog, sand or precipitation, can be highly variable in time and space, the gas attenuation will typically have a more consistent effect on the range of thermal sensors. As such, the gas attenuation often represents a minimum attenuation level under given climatic conditions. As mentioned in section 5.1 and illustrated in Fig. 5.1, water vapour is the dominant contributor to gas attenuation. In the current attenuation model, we therefore only consider gas attenuation which involves water vapour.

Water vapour spectra is made from a combination of narrow absorption lines, arising from transitions between rotational and vibrational energy levels, and a relatively smooth, underlying continuum absorption caused by collisional broadening of the absorption lines. Given the complexity of modelling individual absorption lines, and the fact that we are not interested in calculating absorption in narrow frequency bands, absorption from individual lines is not treated explicitly in

---

[3] In contrast to the MODTRAN® model, the current model is restricted to sea level conditions and does not describe how atmospheric conditions change with altitude. This is a reasonable simplification as long as the observer and the target is located at roughly the same, not too high altitude (mountain region scenarios can be treated by choosing humidity and visibility appropriately) and the acqusition range does not exceed roughly 100 km.

the current model. Instead, we use a water vapour continuum model which is derived from line absorption properties. A commonly used model of this type is the CKD model (Clough et al., 1989) and the subsequent MT CKD model (Clough et al., 2005). In the current work, we have chosen a more recent model, known as the BPS model, which is said to be more correct in the MWIR and LWIR bands (Paynter & Ramaswamy, 2011). By not including the line absorption, we will underestimate the absorption coefficient not only locally, but also when integrating over a wider frequency band. Based on plotted spectra in e.g. Baranov et al. (2008) and comparing the integrated BPS absorption with LWIR band absorption levels in clear-sky conditions provided in Love (2017), we estimate the continuum fraction of the total water vapour absorption to be just under 60%. We compensate this in our model, by multiplying the BPS absorption by a factor, A_{line}, of about 1.6.

The continuum absorption has two contributions: absorption due to interactions between water vapour molecules only and absorption resulting from interactions with other gases. Absorption due to the former class of interactions is referred to as the "self-continuum", while interactions of the latter kind give rise to the "foreign continuum". In all spectral regions, the self-continuum absorption coefficient is greater than the foreign cotninuum coefficient. In addition, the self-continuum, as opposed to the foreign continuum, has a strong, negative exponential temperature dependence. The total extinction coefficient due to water vapour, σ_{gas} in our model can then be written as

$$\sigma_{\text{gas}}(\nu, T) = A_{\text{line}}[\sigma_s(\nu, T) + \sigma_f(\nu, T)], \tag{A.1}$$

where ν is the wavenumber (in units of 1/cm) and T is the temperature (in K). The self- and foreign continuum extinction coefficients can in turn be expressed as

$$\sigma_s(\nu, T) = \frac{P_w}{kT}\left(\frac{P_w}{P_0}\right)\left(\frac{T_0}{T}\right)C_s(\nu, T) \tag{A.2}$$

and

$$\sigma_f(\nu, T) = \frac{P_w}{kT}\left(\frac{P_f}{P_0}\right)\left(\frac{T_0}{T}\right)C_f(\nu). \tag{A.3}$$

P_0 is the reference atmospheric pressure (1 atm) and T_0 is the reference temperature (297 K). P_w is the partial pressure of water vapour, $P_f = P_0 - P_w$, and k is the Boltzmann constant. The partial pressure is the product of the relative humidity, ϕ, and the temperature-dependent saturation pressure, $P_s(T)$. A formula which manages to combine accuracy with simplicity is the Buck formula (Buck, 1981). According to this formula, the saturation pressure of water vapour can be written as

$$P_s(T) = P_B \exp\left[(A - \frac{T}{T_B})(\frac{T}{T_C + T})\right], \tag{A.4}$$

where P_B = 611.21 Pa = $6.032 \cdot 10^{-3}$ atm, A = 18.678, T_B = 234.5 °C, and T_C = 257.14 °C if the temperature T (given in Celsius) is non-negative. If $T < 0$ °C, the following parameter values are used in the Buck formula: P_B = 611.15 Pa = $6.032 \cdot 10^{-3}$ atm, A = 23.036, T_B = 333.7 °C, and T_C = 279.82 °C.

The foreign continuum coefficient, C_f, is only dependent on the wavenumber, and the logarithm of C_f is plotted in the top panel of Fig. A.1. The temperature-dependence of the self-continuum coefficient $C_s(\nu, T)$ can be expressed by the function $\theta_s(\nu)$ so that

$$C_s(\nu, T) = C_s(\nu)\exp\left[(T - T_0)\theta_s(\nu)\right]. \tag{A.5}$$

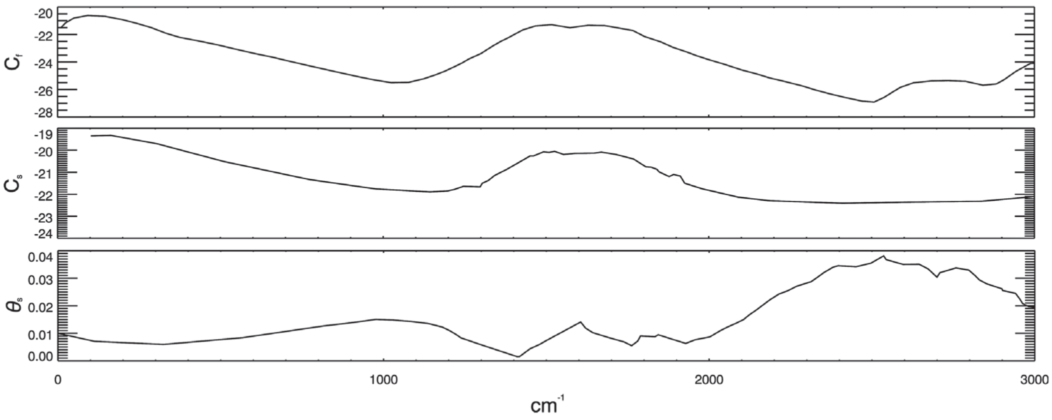

Figure A.1 Water vapour continuum according to the BPS model (Paynter & Ramaswamy, 2011). The top and middle panels show the logarithmic absorption coefficients of the foreign (C_f) and self (C_s) continuum coefficients, respectively, as functions of the wavenumber. C_f and C_s are given in unit of $cm^2atm^{-1}molecules^{-1}$. The bottom panel shows θ_s, the coefficient in the temperature dependent factor of the self-continuum, in units of 1/K.

The wavenumber-dependent functions $\log[C_s(\nu)]$ and $\theta_s(\nu)$ are plotted in the middle and bottom panels of Fig. A.1, respectively. The coefficients C_f and C_s are given in units of $\text{cm}^2\text{atm}^{-1}\text{molecules}^{-1}$, and θ_s is given in the unit $1/K$.

We use Eq. A.1 to calculate the water vapour absorption for varying air temperature and relative humidity. This is plotted as a function of wavelength in Fig. A.2. There are two blue, two green, and two red curves which show results corresponding to air temperatures of -10 °C, 10 °C, and 30 °C, respectively. The brighter shaded curve of each pair has been calculated assuming a relative humidity of 20%, which is similar to what you could expect to have in arid regions. The darker shaded curve of each pair is found by setting the humidity to 90%. For the 30 °C case this would correspond to a tropical climate. All 6 curves have roughly the same shape, with relatively low absorption levels in the MWIR (3-5 μm) and LWIR (8-12 μm) atmospheric windows and much higher levels of absorption in between. Absorption increases with increasing temperature and increasing relative humidity as expected. From Fig. A.2 we see that the gas absorption is roughly the same if the air temperature is -10 °C and the relative humidity is 90% or if the temperature was 10 °C with a relative humidity of only 20%. If the temperature is increased to 30 °C, the absorption levels are roughly 10 times larger at 20% humidity and roughly 100 times larger at 90% humidity. The absorption is slightly lower in the MWIR band than in the LWIR band. For a typical Norwegian summer scenario of 20 °C with 90% relative humidity, the band averaged absorption is about 0.12 for the MWIR band and 0.30 for the LWIR band.

A.2 Aerosol models

Scattering and absorption by droplets or aerosols suspended in the air is often the dominant attenuation effect in the lower the parts of the atmosphere, in particular under low visibility conditions. However, the aerosol concentration, size, and composition might vary greatly which

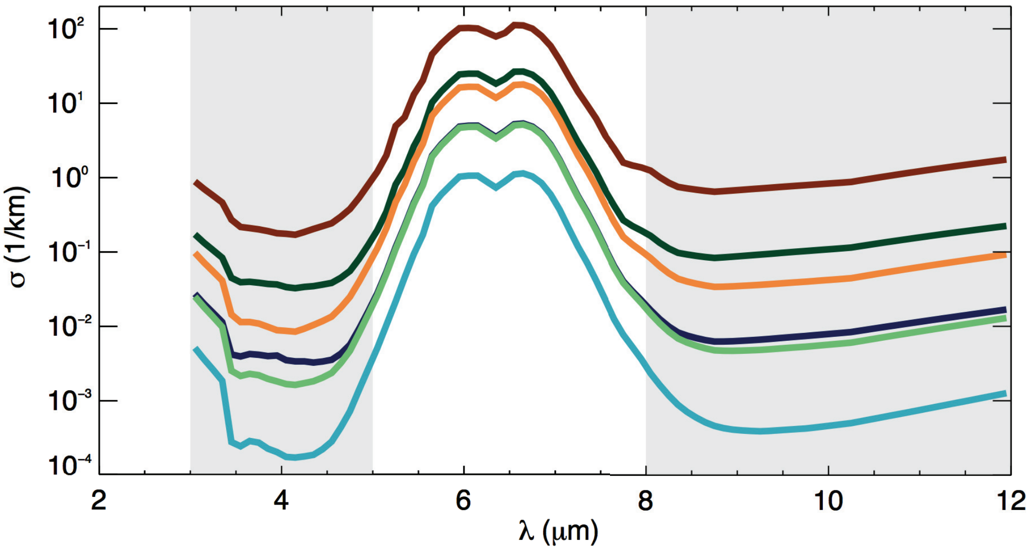

Figure A.2 Water vapour absorption according to the BPS model as a function of wavelength. Results are shown for air temperatures -10 °C (blue curves), 10 °C (green curves), and 30 °C (red curves). The relative humidity is either 20% (bright shading) or 90% (dark shading).

will have a huge impact on the aerosol contribution to the total atmospheric attenuation. The absorption and scattering of light due to the aerosols can be calculated from the size distribution and refractive index from Mie theory. Instead of performing these calculations from scratch, we base our aerosol models on the graphs presented in Shettle & Fenn (1979) and Longtin et al. (1988), which is also the foundation for the aerosol models in MODTRAN (Berk & Hawes, 2017). The aim has been to arrive at aerosol models which are only dependent on easily observable parameters such as humidity and meteorological visibility. The latter parameter is related to the total attenuation in the visible part of the spectrum, usually represented by the wavelength 0.55 μm. Assuming a contrast limit of detection of $\epsilon = 0.02$, the meteorological visibility V is given by Kochsmeider's relation as

$$V = -\frac{\ln \epsilon}{\gamma_{0.55}} = \frac{3.912}{\gamma_{0.55}}, \tag{A.6}$$

where $\gamma_{0.55}$ is the total attenuation at 0.55 μm. For a specific wavelength-dependent profile of the extinction coefficient, the assumed aerosol concentration is adjusted to produce a visibility in accordance with observations. In Shettle & Fenn (1979), the size distribution and refractive index as a function of humidity is presented for 4 moderate-to-high visibility aerosol models, rural, urban, maritime, and tropospheric, as well as 4 fog models for moderate-to-poor visibility scenarios. As the name suggests, the tropospheric model applies to the troposphere above the boundary layer and is therefore not of interest in the current setting. Furthermore, we only use one of the fog models in our description of poor visibility attenuation. A separate desert attenuation model is proposed in Longtin et al. (1988). In the following, the different aerosol models and how they are combined into a single aerosol attenuation model are described.

A.2.1 Rural aerosol model

The rural aerosol model describes land-based, naturally occurring aerosols with no influence from urban or industrial sources. The model, which would be appropriate to use for instance in woodland areas, assumes a mixture of 70% water soluble material and 30% dust particles. Fig. A.3 shows the aerosol attenuation according to the rural model for relative humidity equal to 0% (blue curve), 80% (turquoise curve), 95% (green curve), and 99% (red/yellow dashed curve) assuming a reference aerosol concentration of 15.000 particles per cm^3. The increase in attenuation with increasing humidity comes from a roughly doubling in reference particle radius as the relative humidity increases from 0% to 99%. The corresponding increase in the attenuation is about a factor 10. The dotted, vertical line indicates the 0.55 μm wavelength where the attenuation level is related to the visibility through Eq. A.6. With the chosen aerosol concentration, the visibility decreases from around 25 km to about 5 km as the humidity goes from 0% to 99%. Spectrally, the general trend is that the attenuation decreases with increasing wavelength although there are some locale spikes, most notably at roughly 3 μm and 10 μm. The attenuation is for instance nearly 4 times larger at 3 μm than at 8 μm according to the rural model.

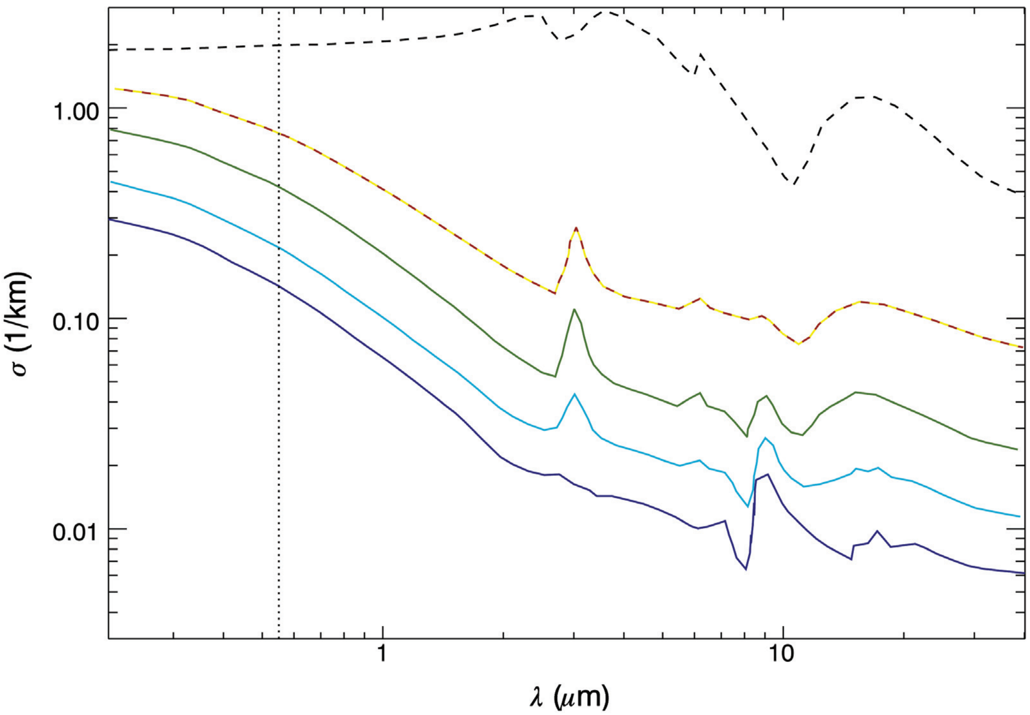

Figure A.3 Extinction coefficient as a function of wavelength according to the rural aerosol model with humidity equal to 0% (blue curve), 80% (turquoise curve), 95% (green curve), and 99% (red/yellow dashed curve). The yellow dashed curve shows the spectral variation in extinction under light fog conditions, while the black, dashed curve shows the same for moderate fog conditions.

A.2.2 Urban aerosol model

In urban areas the aerosols are assumed to be a combination of 80% rural aerosols and 20% sootlike particles from industrial or urban activities. The reference aerosol concentration is 20.000 particles per cm^3. We see from Fig. A.4 that the shape of the extinction curves in the urban model is similar to the corresponding curves of the rural model, but the attenuating effect is larger due to the addition of the sootlike particles. Even if we take into account the higher reference aerosol concentration, the visibility is almost double in the rural model compared to the urban model at 99% humidity.

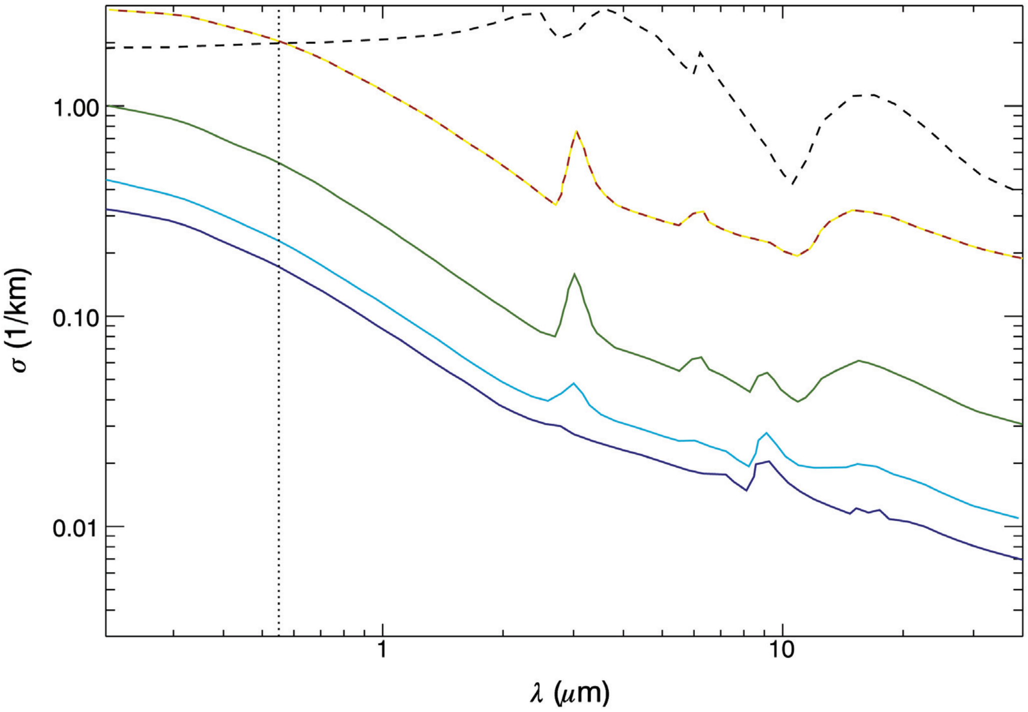

Figure A.4 Extinction coefficient as a function of wavelength according to the urban aerosol model with humidity equal to 0% (blue curve), 70% (turquoise curve), 90% (green curve), and 99% (red/yellow dashed curve). The yellow dashed curve shows the spectral variation in extinction under light fog conditions, while the black, dashed curve shows the same for moderate fog conditions.

A.2.3 Maritime aerosol model

Sea-salt particles are formed as sea-spray droplets evaporate and grow due to the air humidity. These make up an aerosol species of oceanic origin which is unique and which mixes with aerosols of continental origin. This causes the maritime aerosol mix to be distinctly different from the rural and urban mixes. The continental portion of the mix is assumed to be similar to the rural mix, but without the largest particles (assumed lost during transportation). The relative amount of the oceanic and continental aerosols will vary with wind conditions and distance to the coast, however the standard maritime model in Shettle & Fenn (1979) only has about 1% of oceanic aerosols. Fig.

A.5 shows the extinction coefficient as function of wavelength in the maritime model for relative humidity ranging from 0% to 99% for a reference aerosol concentration of 4000 particles per cm^3. A trend which is more pronounced in the maritime model than in the two other aerosol models is the reduction in the slope of the extinction coefficient with wavelength as the humidity increases. This is due to the growth of the aerosols, which increases with increasing particle size, and the corresponding increased contribution of scattering to the total extinction.

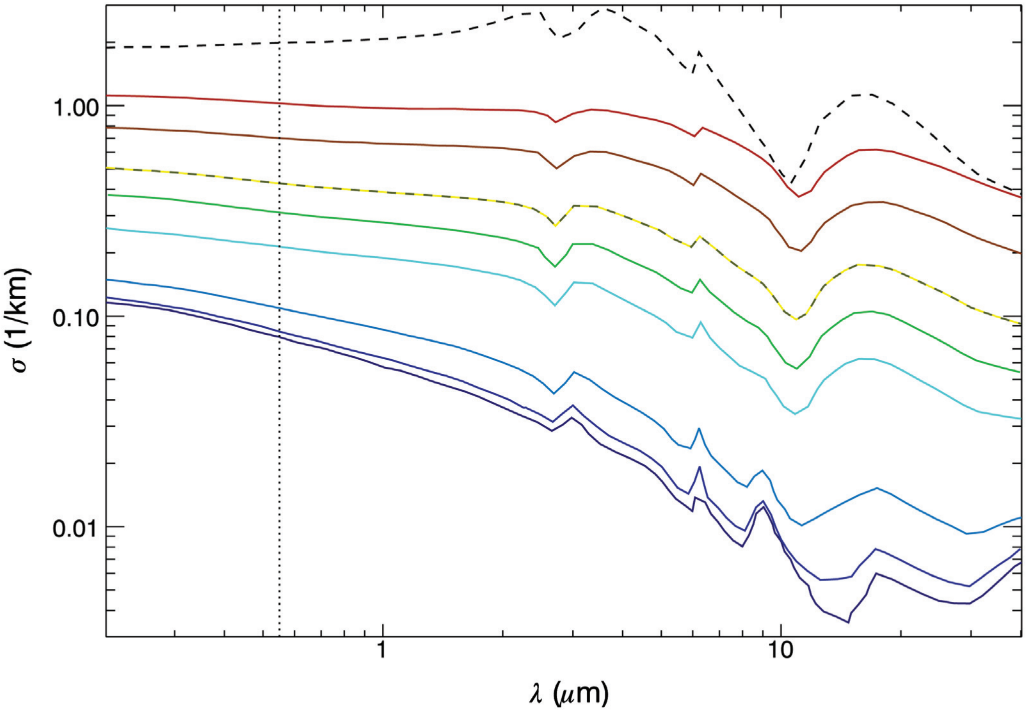

Figure A.5 Extinction coefficient as a function of wavelength according to the maritime aerosol model with humidity equal to 0% (navy blue curve), 50% (blue curve), 70% (light blue curve), 80% (turquoise curve), 90% (green curve), 95% (olive/yellow dashed curve), 98% (brown curve), and 99% (red curve). The yellow dashed curve shows the spectral variation in extinction under light fog conditions, while the black, dashed curve shows the same for moderate fog conditions.

A.2.4 Fog modelling

Haze, mist, and fog are terms indicating a reduced visible range due to an aggregate of small water droplets suspended in the atmosphere close to the ground. These phenomena can occur when the air is close to being saturated with water vapour. There are different types of fog, two of which are treated by models in Shettle & Fenn (1979). **Advection fog** arises from the often wind-induced movement of relatively warm, moist air over a colder ground, like warm air initially above sea moving in over land. **Radiation fog** on the other hand, requires little or no wind to form. It forms typically overnight as the air near the ground cools and stabilises. This type of fog is most easily formed in sheltered valleys with little wind. The 4 fog models in Shettle & Fenn (1979) cover the two fog types in conditions ranging from moderate to poor visibility. In addition, it is noted in Shettle & Fenn (1979) that

1. In heavy fog, with visibility less than 200-250 m, the extinction coefficient is more or less independent of wavelength.
2. In light to moderate fog, visibility from around 350 m up to 1000 m, the attenuation in the LWIR band is substantially less than in visible light and in the MWIR band.
3. In very light fog, with visibility greater than 1 km, the aerosol models with 99% humidity, and adjusted for visibility, can be used.

Regarding moderate fog levels, it is noted in FLIR Systems Inc. (2019) that calculationS with MODTRAN show the detection range is about 4 times larger in LWIR than in MWIR and in visible light when the meteorological visibility is around 600 m. As for heavy fog with visibility of 300 m or less, MODTRAN calculation referred to in FLIR Systems Inc. (2019) shows that the range in IR is even lower than in visible by about 4-5 %.

Based on these observations, we propose a simple extension to the aerosol models into the regime of fog-dominated weather conditions. It does not distinguish between different types of fog. This extension combines the various sub-models based on the meteorological visibility V. With heavy fog, $V \leq 0.3$ km, a common IR extinction coefficient, σ_{IR}, models the attenuation in both the MWIR and LWIR bands. Expressed as a modification to Kochsmeider's relation (see Eq. A.6), σ_{IR} is given as

$$\sigma_{\text{IR}}(V) = \frac{3.912 + 0.05/V}{V} \tag{A.7}$$

with V given in units of kilometre. With more moderate fog levels, the model utilises fog model 4 in Shettle & Fenn (1979) which originally was constructed for light to moderate fog conditions. This model is reproduced by the black, dashed line in Figs. A.3-A.5. We see that one characteristic of this model is that the extinction coefficient, which we denote $\sigma_4(\lambda, V)$ is indeed close to 4 times smaller in the LWIR band than in the visible and MWIR bands. For moderate fog visibility between 0.3 km and 0.6 km, a linear transition from σ_{IR} to σ_4 is created:

$$\sigma_{\text{mod}}(\lambda, V) = [1 - \omega_2(V)]\sigma_{\text{IR}}(V) + \omega_2(V)\sigma_4(\lambda, V), \tag{A.8}$$

where

$$\omega_2(V) = \frac{V - 0.3\text{ km}}{0.3\text{ km}}. \tag{A.9}$$

With visibility better than 0.6 km, we turn to the normal aerosol models in order to define a reference profile for light fog conditions. In the rural and urban aerosol models, we use the profiles corresponding to 99% relative humidity for this purpose, as suggested in Shettle & Fenn (1979). In the case of the maritime model, we instead use the 95% humidity profile for light fog modelling. The reason is that the difference between the extinction coefficient in the visible/MWIR bands and the LWIR band is too small in the 99% humidity maritime case. Since the attenuation level is scaled to match the observed visibility, it is only the relative spectral variation that is of importance. The light fog aerosol profile for each aerosol type is indicated in Figs. A.3-A.5 by the yellow, dashed curve. In the visibility range from 0.6 km to 1.0 km, the light fog regime, the extinction coefficient is calculated as a linear combination of the dedicated fog model 4 from Shettle & Fenn (1979), $\sigma_4(\lambda, V)$, and the aerosol-specific models hereafter referred to as $\sigma_{\text{fog}}^{\text{type}}(\lambda, V)$ (where type is rural, urban or maritime):

$$\sigma_{\text{light}}^{\text{type}}(\lambda, V) = [1 - \omega_1(V)]\sigma_4(\lambda, V) + \omega_1(V)\sigma_{\text{type}}^{\text{type}}(\lambda, V) \tag{A.10}$$

where

$$\omega_1(V) = \frac{V - 0.6\text{ km}}{0.4\text{ km}}. \tag{A.11}$$

As visibility increases beyond 1 km, the model should gradually transition into the regular aerosol models described in sections A.2.1-A.2.3. We have again chosen a linear transition which is completed at 2 km visibility. It represents a fog model under minimal fog conditions, denoted $\sigma_{\text{min}}^{\text{type}}$, which in addition to the visibility V and wavelength λ will depend on the relative humidity ϕ since the regular aerosol models, here referred to as $\sigma_{\text{reg}}^{\text{type}}(\lambda, V, \phi)$, depend on humidity. This minimal fog model can be expressed as

$$\sigma_{\text{min}}^{\text{type}}(\lambda, V, \phi) = [1 - \omega_0(V)]\sigma_{l}^{\text{type}}(\lambda, V) + \omega_0(V)\sigma_{\text{reg}}^{\text{type}}(\lambda, V, \phi) \tag{A.12}$$

where

$$\omega_0(V) = V - 1.0\text{ km}. \tag{A.13}$$

A.2.5 Complete humidity-dependent aerosol model

In the sections A.2.1-A.2.4, a comprehensive aerosol model has been described which depends on the type of aerosols (rural, urban or maritime), the wavelength (λ), the air humidity (ϕ), and meteorological visibility (V). This model includes the effects of fog, mist or haze due to extra high humidity. Here we summarise the model by expressing the extinction coefficient of the complete humidity-dependent aerosol model, $\sigma_{\text{type}}(\lambda, \phi, V)$, as

$$\sigma_{\text{type}}(\lambda, \phi, V) = \begin{cases} \sigma_{\text{IR}}(V) & \text{for } V \leq 0.3\text{ km;} \\ \sigma_{\text{mod}}(\lambda, V) & \text{for } 0.3\text{ km} < V \leq 0.6\text{ km;} \\ \sigma_{\text{light}}^{\text{type}}(\lambda, V) & \text{for } 0.6\text{ km} < V \leq 1.0\text{ km;} \\ \sigma_{\text{min}}^{\text{type}}(\lambda, V, \phi) & \text{for } 1.0\text{ km} < V < 2.0\text{ km;} \\ \sigma_{\text{reg}}^{\text{type}}(\lambda, V, \phi) & \text{otherwise,} \end{cases} \tag{A.14}$$

where σ_{IR} is defined by Eq. A.7, σ_{mod} is defined by Eq. A.8, $\sigma_{\text{light}}^{\text{type}}$ is defined by Eq. A.10, and $\sigma_{\text{min}}^{\text{type}}$ is defined by Eq. A.12. The extinction coefficient in the regular aerosol models, $\sigma_{\text{reg}}^{\text{type}}$, is determined from the profiles in Figs. A.3 (rural aerosols), A.4 (urban aerosols), or A.5 (maritime aerosols). Using linear interpolation, the extinction coefficients for specific wavelength and air humidity values are determined, and using scaling, the attenuation levels are adjusted so that the 0.55 μm extinction coefficient matches the specified visibility.

Fig. A.6 illustrates the humidity-dependent aerosol model for all 3 aerosol models. Panel **a** uses the rural aerosol type, panel **b** describes the urban aerosol type, while panel **c** illustrates the maritime aerosol type. The band-averaged extinction coefficients for the MWIR band (presented by blue curves) and the LWIR band (presented by red curves) is calculated assuming a relative humidity of 20% (light shading) and 90% (dark shading) and plotted as functions of visibility V. The vertical lines indicate transition between different fog regimes. We clearly see that the extinction coefficient only dependent on visibility when $V < 0.3$ km. The difference between the MWIR and LWIR attenuation grows in the visibility range 0.3 km $< V \leq 0.6$ km, but still without any dependence on the aerosol type of humidity. In the range 0.6 km $< V \leq 1.0$ km, the MWIR attenuation gets closer to the LWIR attenuation, but the aerosol type determines by how much.

From $V > 1$ km, the humidity starts to gradually play a role. For the LWIR band with the rural or urban aerosol types, the extinction coefficient for a given visibility is higher when the humidity is lower. This might seem counterintuitive since increased relative humidity will increase the attenuation caused by aerosols if the particle concentration is unchanged. However, in order to maintain the same meteorological visibility as humidity increases, the concentration of aerosol particles must go down. Therefore, it all depends on the type-specific aerosol attenuation model whether the extinction coefficient increases or decreases as the aerosol concentration drops and the humidity increases simultaneously in such as way that the visibility is kept constant.

If we instead focus on the urban aerosol model in the MWIR band, we see in Fig. A.6b that the two blue curves, representing widely different relative humidities, overlap almost perfectly even in the $V > 2$ km regime. This means that the shape of the urban aerosol extinction profiles (shown in Fig. A.4) are such that a shift in the $\lambda = 0.55\mu$m extinction coefficient (which is inversely proportional to the visibility) results in roughly the same shift in the corresponding 3-5 μm averaged extinction coefficient.

A.2.6 Desert aerosol model

The aerosol models considered so far, all depend on air humidity, either directly or indirectly (since fog, mist and haze as phenomena depend on high relative humidity). In arid regions, aerosols interacting with water vapour is not the most important contributing factor to aerosol attenuation. Instead, sand lifted into the atmosphere during dust storms can severely reduce the detection range both in visible and infrared light. The stronger a storm is, the more sand will it be able to lift into the air, and the stronger will the attenuation potentially be. For this reason, Longtin et al. (1988) proposed a desert aerosol model where the extinction coefficient depends on wind speed rather than air humidity. It is true that local wind conditions provide a mechanism for injecting and transporting sand. However, measurements show that the correlation between local wind speed and visibility is a lot weaker than one might expect, especially when looking at gentle to moderate wind speeds (de Villiers & van Heerden, 2007). This has to do with variation in vegetation, wind direction, effects of turbulence, and the fact that dust will remain suspended in the atmosphere for quite some time after the wind has dropped. Sand can also be brought high into the atmosphere at one location before being transported quite far by moderate winds.

With all these uncertainties regarding the quantitative effects of local wind speed on the concentration of sand particles in the atmosphere, we have chosen a desert aerosol model which only depends on the meteorological visibility, in addition to the wavelength. We still make use of the 4 extinction coefficient profiles provided in Longtin et al. (1988). But instead of relating the profiles to wind speeds, from 0 m/s to 30 m/s in increments of 10 m/s, we simply relate them to a decreasing visibility as given by the extinction coefficient at 0.55 μm. The visibility corresponding to the 4 profiles in Longtin et al. (1988) equals about 101 km, 68 km, 18 km, and 2.1 km. By interpolation (and extrapolation), we can estimate the spectral extinction coefficient for an arbitrary value of the visibility. In Fig. A.7, 10 extinction coefficient profiles are plotted for the spectral range 2-14 μm. As the curve colours indicate, the visibility corresponding to these profiles range from about 1.6 km to 100 km. It is evident from the spectral plots that the variation in extinction coefficient due to sand aerosols is quite small in the MWIR and LWIR bands. By transforming the extinction coefficient into an IR range using Kochsmeider's relation (Eq. A.6), it is also clear that the detection range in IR will be at least as good as in visible light, and even larger than the meteorological visibility when the seeing is good and the visibility is more than 20 km or so.

A.3 Precipitation models

So far, we've covered atmospheric attenuation of infrared light due to water vapour and aerosols of various kind. Another source of atmospheric attenuation is precipitation, most commonly rain or snow. The effects of precipitation on radiative transfer in the visible and infrared frequency range have been studied for more than 50 years (Chu & Hogg, 1968). Precipitation could be considered to be special cases of aerosols, but since it is natural to consider the attenuating effect as a function of precipitation rate, a parameter easily observable, we will regard it as a separate attenuation class. With snow, we could also foresee the need of an additional aerosol model similar to the desert aerosol model described in section A.2.6 to describe attenuation in snow storm conditions. A wind speed dependent attenuation model would probably make more sense when we are considering snow storms rather than sand storms, however the characteristics of the snow would also be very important in a snow storm attenuation model. It is beyond the scope of the current work to develop a detailed snow model, and we will only consider attenuation due to snowfall (and rainfall) when no wind is present.

A.3.1 Rain model

We base our rain model on studies presented in a recent review paper (Sanders-Reed & Fenley, 2018). It contains information about wavelength-dependent visibility (which is translated into extinction coefficient using Eq. A.6) in the range 0.55-15 μm for 4 different rain rate levels: 0.25 mm/hr (light rain), 4.0 mm/hr (moderate rain), 25 mm/hr (heavy rain), and 150 mm/hr (violent rain). From these 4 spectral visibility profiles, we can interpolate to estimate the extinction coefficient at an arbitrary rain rate. The extinction coefficient as a function of wavelength in the spectral range 2-14 μm is plotted in Fig. A.8 for rain rates from 0.1 mm/hr to 100 mm/hr. In light rain, the attenuation decreases slightly with increasing wavelength. But as the rain rate increases beyond 1 mm/hr, this trend has shifted. When the rate rain is about 4.5 mm/hr, the extinction coefficient is nearly 2.0 1/km at $\lambda = 14\mu$m but only 1.0 1/km at $\lambda = 3\mu$m. If the rain rate increases even further, the difference in attenuation in the MWIR and LWIR bands grows smaller, however the trend is qualitatively the same.

A.3.2 Snow model

Snowflakes can vary greatly in both in size and in water content. It is therefore not surprising that it is difficult to quantify the attenuating effects of falling snow on electromagnetic wave propagation. Early studies, most of which focus on visible light, show for instance more than a factor 2 difference in estimated exponent when fitting data to a power-law dependence of attenuation on snow rate (Seagraves, 1984). A more recent study uses two digital IR cameras on targets at three different distances to record the visibility in MWIR (3-5 μm) and LWIR (8-10 μm) bands, respectively (van Rheenen et al., 2006). We base our IR snow model on the findings from this study. Assuming the extinction coefficient related to snowfall has a power-law depends on the snow rate, we can write

$$\sigma_{\text{snow}}(b) = C_b p^{k_b}, \tag{A.15}$$

where p is the snow rate in mm/hr and C_b and k_b are constants determined from the experimental data for frequency band b, which is either MWIR, LWIR or visible. For MWIR we find $C_{\text{MWIR}} = 2.3$ and $k_{\text{MWIR}} = 0.50$, while for LWIR we get $C_{\text{LWIR}} = 3.3$ and $k_{\text{LWIR}} = 0.43$. This means that the attenuation is slightly smaller in the MWIR band than in the LWIR band, which is slightly surprising but seems to be consistent with earlier findings (Seagraves, 1984). In visible light, we use the model constants presented in Bisyarin et al. (1971) for 0.63μm where $C_{\text{MWIR}} = 2.5$ and $k_{\text{MWIR}} = 0.50$. Fig. A.9 shows the extinction coefficient as a function of the snow rate for LWIR (red curve), MWIR (blue curve), and visible light (black curve).

A.4 Complete attenuation model

After having presented each of the different sub-models that make up the currently used attenuation model, it only remains to combine the sub-models into one comprehensive and consistent attenuation model. Let γ denote the complete atmospheric extinction coefficient due to all the considered effects. This coefficient will depend on:

- Wavelength (λ)
- Air temperature (T)
- Meteorological visibility (V)
- Air humidity (ϕ)
- Aerosol type (rural, urban, maritime or desert)
- Precipitation rate (p)
- Precipitation type (snow or rain)

Expressing γ as the combined attenuation from water vapour, aerosols, and precipitation, we get

$$\gamma = \sigma_{\text{gas}} + \sigma_{\text{aero}} + \sigma_{\text{precip}}, \tag{A.16}$$

where σ_{gas} is given by Eq. A.1. If there is precipitation, σ_{precip} is positive and given either by Fig. A.8 (in case of rain) of by Eq. A.15 (in case of snow). The aerosol contribution, σ_{aero}, is either given by Eq. A.14 or, if desert is the appropriate aerosol type, by Fig. A.7. In any case, meteorological visibility is an input parameter when calculating the aerosol attenuation. In case of precipitation, the observed visibility will be a result of the combined attenuation of aerosols and precipitation. Since the aerosol models were made assuming no precipitation, we have to subtract the effect of the precipitation on the visibility before calculating the aerosol attenuation.

Let us first calculate the attenuation due to precipitation at 0.55μm (in case of snow, the attenuation in visible light is taken at 0.63μm), $\sigma^{0.55}_{\text{precip}}$, and let V_{tot} denote the observed (total) visibility. Once again turning to Kochsmeider's relation (Eq. A.6), we have

$$V_{\text{tot}} = \frac{C_\epsilon}{\sigma^{0.55}_{\text{aero}} + \sigma^{0.55}_{\text{precip}}}, \tag{A.17}$$

where $C_\epsilon = -\ln\epsilon = 3.912$ if $\epsilon = 0.02$. Assuming the precipitation is removed, the finite visibility would only depend on the aerosol attenuation. The visibility in this case, V_{aero}, would be

$$V_{\text{aero}} = \frac{C_\epsilon}{\sigma^{0.55}_{\text{aero}}}. \tag{A.18}$$

The tables of calculated extinction coefficients provided in Appendix B uses the observable visibility as a main parameter, while the visibility required as input to the aerosol models is V_{aero}. Since we need to know V_{aero} in order to calculate $\sigma_{\text{aero}}(\lambda)$, we want to combine Eqs. A.17 and A.18 to find

$$V_{\text{aero}} = V_{\text{tot}}\frac{C_\epsilon}{C_\epsilon - V_{\text{tot}}\sigma^{0.55}_{\text{precip}}}. \tag{A.19}$$

When discussing hypothetical scenarios, it might be more useful to specify the visibility for the zero precipitation case and then add rain or snow as an additional effect, if relevant. In order to make use of the tables in Appendix B, it can therefore be useful to rewrite Eq. A.19 as

$$V_{\mathrm{tot}} = V_{\mathrm{aero}} \frac{C_\epsilon}{C_\epsilon + V_{\mathrm{aero}} \sigma_{\mathrm{precip}}^{0.55}} . \tag{A.20}$$

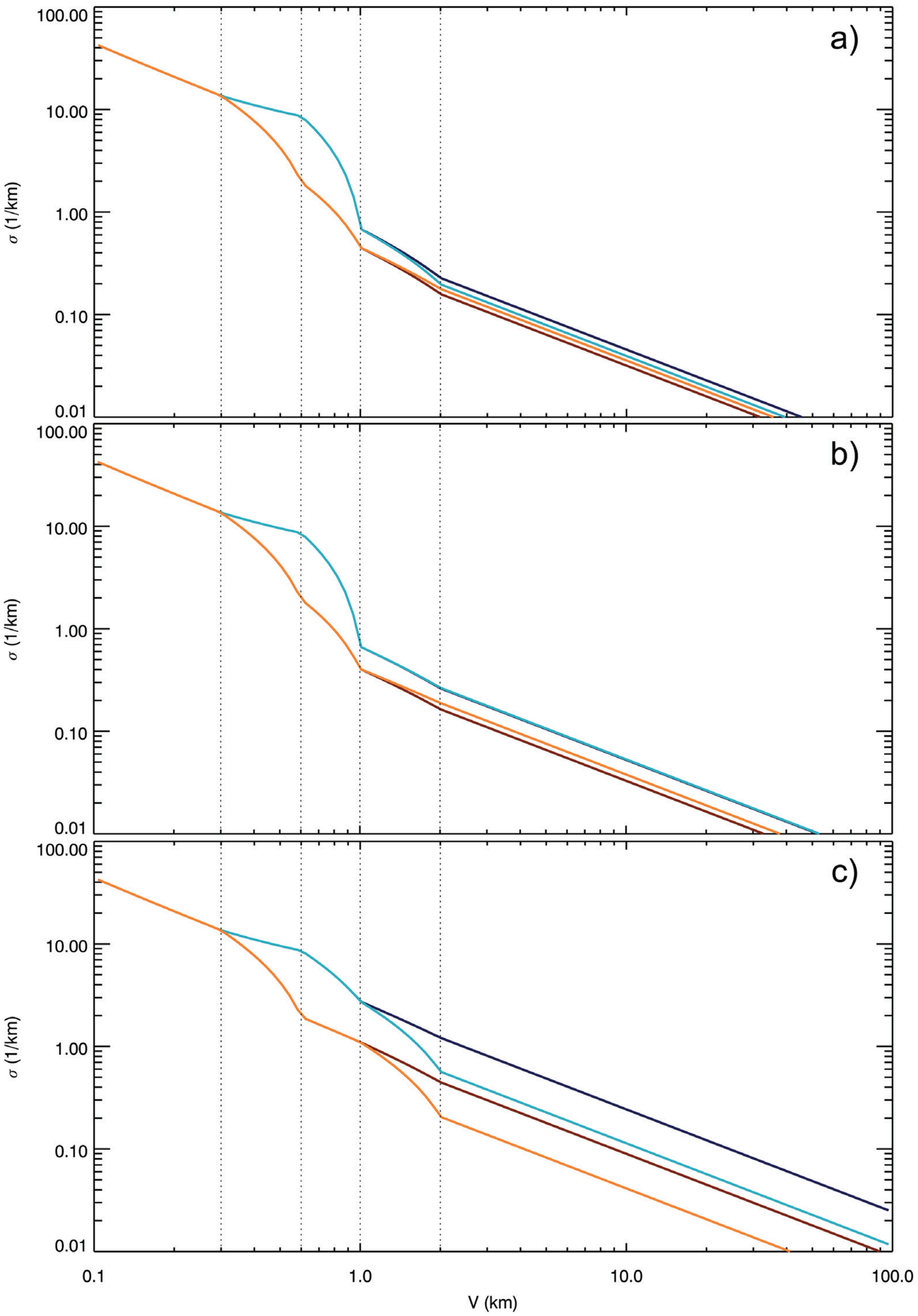

*Figure A.6 Aerosol extinction coefficient as a function of visibility for the rural (**a**), urban (**b**), and maritime (**c**) models. Results are shown for the MWIR (blue curves) and LWIR (red curves) bands with 20% (light shading) and 90% (dark shading) relative humidity. The dotted, vertical lines indicate transitions between different fog regimes.*

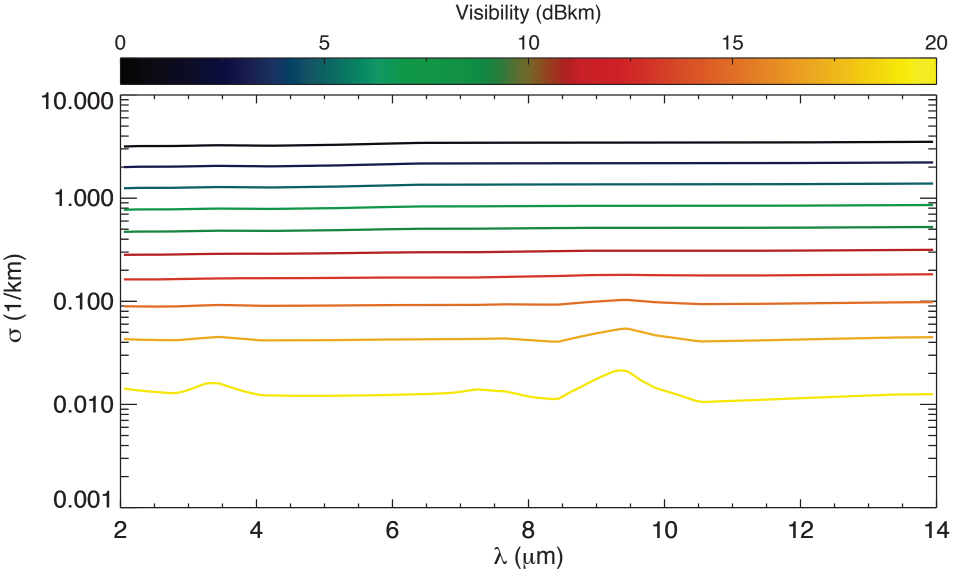

Figure A.7 Extinction coefficient as a function of wavelength according to the desert aerosol model. The colours indicate the visibility on a dB-scale for visibility up to 100 km.

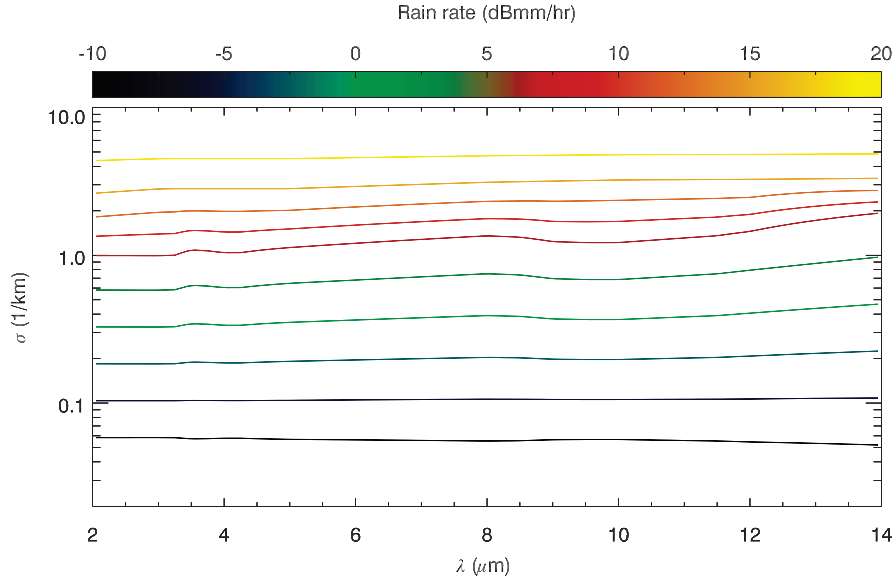

Figure A.8 *Attenuation as function of wavelength due to rain. The colours indicate the rain rate in mm/hr on a dB-scale.*

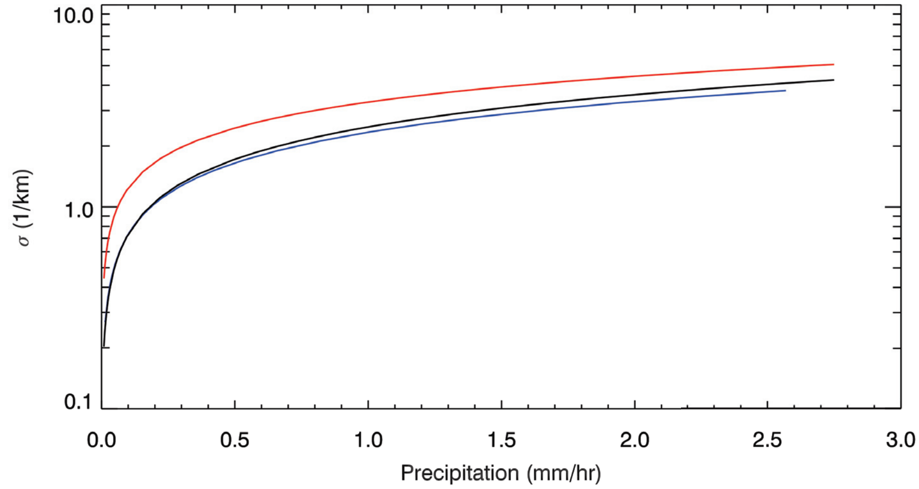

Figure A.9 *Attenuation due to snowfall as a function of the precipitation rate. The attenuation is integrated over the LWIR (red curve), MWIR (blue curve) and visible (0.63 μm) frequency bands (black curve).*

B Tabulated atmospheric attenuation

In order to predict the acquistion range of a sensor using the PMRTD method, described in section 6.3 and expressed by Eq. 6.10, one needs to estimate the atmospheric extinction, γ, for the appropriate frequency band. In the following section, we list the γ, relevant for sensors operating in the MWIR and LWIR frequency bands for various atmospheric conditions using the atmospheric attenuation model described in section A and expressed by Eq. A.16. The extinction coefficient is given in look-up tables as a function of meteorological visibility (V) and air temperature (T) when no precipitation is present. In the case of rain, rain rate is an additional variable. For both the no precipitation case and the rainfall case, each table is made under the assumption of a specific frequency band, aerosol model and air humidity. In the case of snow, tables are made for a specific frequency band, aerosol model and a reference air temperature, expressing γ as a function of visibility, snowfall rate, and air humidity.

This section is split into two main sub-sections: section B.1 focuses on the MWIR frequency band, while section B.2 pertains to the LWIR frequency band. For each of these frequency bands, there are sub-sections for each of the 4 aerosol models. There are 8 tables for each of the rural, urban, and maritime aerosol models. These tables cover air the humidity levels 50-80-90-95 % for the no precipitation cases and the humidity levels 50-80-90 % for the rainfall case, in addition to a single snowfall table. In the case of the desert aerosol model, there is a single table for each frequency band assuming 20 % air humidity.

B.1 MWIR ($3 - 5\mu$m)

This section lists the atmospheric extinction coefficient, γ, in the MWIR frequency band according to the atmospheric attenuation model described in section A sorted according to: (i) the aerosol model (ii) no precipitation/rainfall/snowfall (iii) air humidity.

B.1.1 Rural aerosol model

Tables B.1-B.8 list the atmospheric extinction coefficient, γ, in the MWIR frequency band assuming the rural aerosol model according to the atmospheric attenuation model described in section A.

		Visibility (km)								
		0.20	0.50	1.00	2.00	5.00	10.00	20.00	40.00	80.00
Temperature (°C)	-30	20.8	9.35	0.74	0.22	0.088	0.044	0.022	0.011	$5.9 \cdot 10^{-3}$
	-20	20.8	9.35	0.74	0.22	0.089	0.045	0.023	0.012	$6.6 \cdot 10^{-3}$
	-10	20.8	9.35	0.74	0.22	0.091	0.047	0.025	0.014	$8.8 \cdot 10^{-3}$
	0	20.8	9.36	0.75	0.23	0.097	0.054	0.032	0.021	0.015
	10	20.8	9.37	0.76	0.24	0.11	0.067	0.045	0.035	0.029
	20	20.9	9.40	0.79	0.27	0.14	0.099	0.077	0.066	0.061
	30	20.9	9.47	0.86	0.34	0.21	0.17	0.15	0.13	0.13

Table B.1 Extinction coefficient (1/km) in the **MWIR** *band assuming the* **rural** *aerosol model with* **50% humidity** *but* **no precipitation** *as a function of temperature (°C) and meteorological visibility (km).*

		Visibility (km)								
		0.20	0.50	1.00	2.00	5.00	10.00	20.00	40.00	80.00
Temperature (°C)	-30	20.8	9.35	0.74	0.24	0.095	0.048	0.024	0.013	$6.6 \cdot 10^{-3}$
	-20	20.8	9.35	0.74	0.24	0.097	0.049	0.026	0.014	$8.0 \cdot 10^{-3}$
	-10	20.8	9.36	0.74	0.24	0.10	0.054	0.030	0.018	0.012
	0	20.8	9.37	0.76	0.26	0.11	0.067	0.044	0.032	0.026
	10	20.9	9.40	0.79	0.29	0.15	0.098	0.075	0.063	0.057
	20	20.9	9.47	0.86	0.36	0.22	0.17	0.15	0.14	0.13
	30	21.1	9.64	1.02	0.52	0.38	0.33	0.31	0.30	0.29

Table B.2 *Extinction coefficient (1/km) in the* **MWIR** *band assuming the* **rural** *aerosol model with* **80% humidity** *but* **no precipitation** *as a function of temperature (°C) and meteorological visibility (km).*

		Visibility (km)								
		0.20	0.50	1.00	2.00	5.00	10.00	20.00	40.00	80.00
Temperature (°C)	-30	20.8	9.35	0.74	0.25	0.099	0.050	0.025	0.013	$6.9 \cdot 10^{-3}$
	-20	20.8	9.35	0.74	0.25	0.10	0.051	0.027	0.015	$8.6 \cdot 10^{-3}$
	-10	20.8	9.36	0.74	0.25	0.11	0.057	0.032	0.020	0.014
	0	20.8	9.37	0.76	0.27	0.12	0.073	0.049	0.036	0.030
	10	20.9	9.41	0.80	0.31	0.16	0.11	0.087	0.075	0.069
	20	21.0	9.50	0.89	0.40	0.25	0.20	0.18	0.17	0.16
	30	21.2	9.70	1.09	0.60	0.45	0.40	0.38	0.37	0.36

Table B.3 *Extinction coefficient (1/km) in the* **MWIR** *band assuming the* **rural** *aerosol model with* **90% humidity** *but* **no precipitation** *as a function of temperature (°C) and meteorological visibility (km).*

		Visibility (km)								
		0.20	0.50	1.00	2.00	5.00	10.00	20.00	40.00	80.00
Temperature (°C)	-30	20.8	9.35	0.74	0.25	0.10	0.051	0.026	0.013	$7.0 \cdot 10^{-3}$
	-20	20.8	9.35	0.74	0.25	0.10	0.052	0.027	0.015	$8.9 \cdot 10^{-3}$
	-10	20.8	9.36	0.74	0.26	0.11	0.058	0.033	0.021	0.015
	0	20.8	9.38	0.76	0.27	0.13	0.076	0.051	0.039	0.033
	10	20.9	9.42	0.80	0.32	0.17	0.12	0.093	0.081	0.075
	20	21.0	9.52	0.90	0.42	0.27	0.22	0.19	0.18	0.18
	30	21.2	9.74	1.13	0.64	0.49	0.44	0.42	0.41	0.40

Table B.4 *Extinction coefficient (1/km) in the* **MWIR** *band assuming the* **rural** *aerosol model with* **95% humidity** *but* **no precipitation** *as a function of temperature (°C) and meteorological visibility (km).*

T (°C)	p (mm/hr)	Visibility (km)				
		0.50	1.00	2.00	5.00	10.00
0	0.2	9.38	0.80	0.30	0.17	0.12
	1.0	9.43	0.97	0.50	0.37	0.33
	4.0	9.63	1.50	1.13	-	-
	8.0	9.81	1.81	1.48	-	-
10	0.2	9.39	0.82	0.31	0.18	0.14
	1.0	9.45	0.99	0.52	0.39	0.34
	4.0	9.65	1.52	1.14	-	-
	8.0	9.82	1.82	1.49	-	-
20	0.2	9.42	0.85	0.34	0.21	0.17
	1.0	9.48	1.02	0.55	0.42	0.37
	4.0	9.68	1.55	1.18	-	-
	8.0	9.85	1.85	1.52	-	-
30	0.2	9.49	0.92	0.41	0.28	0.24
	1.0	9.55	1.09	0.62	0.49	0.44
	4.0	9.75	1.62	1.24	-	-
	8.0	9.92	1.92	1.59	-	-

Table B.5 Extinction coefficient (1/km) in the **MWIR** *band assuming the* **rural** *aerosol model with* **50% humidity** *and rain as a function of temperature (°C), rain rate (mm/hr), and meteorological visibility (km).*

T (°C)	p (mm/hr)	Visibility (km)				
		0.50	1.00	2.00	5.00	10.00
0	0.2	9.39	0.81	0.32	0.18	0.14
	1.0	9.44	0.99	0.53	0.39	0.34
	4.0	9.64	1.52	1.15	-	-
	8.0	9.82	1.83	1.49	-	-
10	0.2	9.42	0.84	0.36	0.21	0.17
	1.0	9.48	1.02	0.56	0.42	0.37
	4.0	9.67	1.55	1.18	-	-
	8.0	9.85	1.86	1.52	-	-
20	0.2	9.49	0.92	0.43	0.29	0.24
	1.0	9.55	1.09	0.63	0.49	0.44
	4.0	9.75	1.63	1.25	-	-
	8.0	9.92	1.93	1.60	-	-
30	0.2	9.65	1.08	0.59	0.45	0.40
	1.0	9.71	1.25	0.79	0.65	0.61
	4.0	9.91	1.79	1.42	-	-
	8.0	10.1	2.10	1.76	-	-

Table B.6 Extinction coefficient (1/km) in the **MWIR** *band assuming the* **rural** *aerosol model with* **80% humidity** *and rain as a function of temperature (°C), rain rate (mm/hr), and meteorological visibility (km).*

T (°C)	p (mm/hr)	Visibility (km)				
		0.50	1.00	2.00	5.00	10.00
0	0.2	9.39	0.82	0.34	0.19	0.14
	1.0	9.45	0.99	0.54	0.39	0.34
	4.0	9.65	1.53	1.16	-	-
	8.0	9.82	1.84	1.50	-	-
10	0.2	9.43	0.86	0.37	0.23	0.18
	1.0	9.49	1.03	0.58	0.43	0.38
	4.0	9.69	1.57	1.20	-	-
	8.0	9.86	1.88	1.54	-	-
20	0.2	9.52	0.95	0.47	0.32	0.27
	1.0	9.58	1.12	0.67	0.52	0.47
	4.0	9.78	1.66	1.29	-	-
	8.0	9.95	1.97	1.63	-	-
30	0.2	9.72	1.15	0.67	0.52	0.47
	1.0	9.78	1.32	0.87	0.72	0.67
	4.0	9.98	1.86	1.49	-	-
	8.0	10.15	2.17	1.83	-	-

Table B.7 Extinction coefficient (1/km) in the **MWIR** *band assuming the* **rural** *aerosol model with* **90% humidity** *and rain as a function of temperature (°C), rain rate (mm/hr), and meteorological visibility (km).*

ϕ (%)	p (mm/hr)	Visibility (km)			
		0.50	1.00	2.00	4.00
50	0.1	9.52	1.28	0.87	0.76
	0.3	9.59	1.67	1.35	-
	1.0	7.23	2.50	-	-
	3.0	4.67	-	-	-
90	0.1	9.52	1.29	0.89	0.77
	0.3	9.59	1.69	1.36	-
	1.0	7.23	2.53	-	-
	3.0	4.68	-	-	-

Table B.8 Extinction coefficient (1/km) in the **MWIR** *band assuming the* **rural** *aerosol model as a function of relative humidity (%), snow rate (mm/hr), and meteorological visibility (km). Calculations made at reference temperature -10°C).*

		Visibility (km)								
		0.20	0.50	1.00	2.00	5.00	10.00	20.00	40.00	80.00
Temperature (°C)	-30	20.8	9.35	0.73	0.28	0.11	0.055	0.028	0.014	$7.3 \cdot 10^{-3}$
	-20	20.8	9.35	0.73	0.28	0.11	0.056	0.029	0.015	$8.0 \cdot 10^{-3}$
	-10	20.8	9.35	0.73	0.28	0.11	0.058	0.031	0.017	0.010
	0	20.8	9.36	0.74	0.28	0.12	0.065	0.037	0.023	0.017
	10	20.8	9.37	0.75	0.30	0.13	0.079	0.051	0.037	0.030
	20	20.9	9.40	0.79	0.33	0.17	0.11	0.083	0.069	0.062
	30	20.9	9.47	0.85	0.40	0.23	0.18	0.15	0.14	0.13

Table B.9 Extinction coefficient (1/km) in the **MWIR** *band assuming the* **urban** *aerosol model with* **50% humidity** *but* **no precipitation** *as a function of temperature (°C) and meteorological visibility (km).*

		Visibility (km)								
		0.20	0.50	1.00	2.00	5.00	10.00	20.00	40.00	80.00
Temperature (°C)	-30	20.8	9.35	0.73	0.28	0.11	0.057	0.029	0.015	$7.7 \cdot 10^{-3}$
	-20	20.8	9.35	0.73	0.28	0.12	0.059	0.030	0.016	$9.2 \cdot 10^{-3}$
	-10	20.8	9.36	0.74	0.29	0.12	0.063	0.035	0.021	0.014
	0	20.8	9.37	0.75	0.30	0.13	0.076	0.048	0.034	0.027
	10	20.9	9.40	0.78	0.33	0.16	0.11	0.079	0.065	0.058
	20	20.9	9.47	0.85	0.41	0.24	0.18	0.15	0.14	0.13
	30	21.1	9.64	1.02	0.57	0.40	0.34	0.31	0.30	0.29

Table B.10 Extinction coefficient (1/km) in the **MWIR** *band assuming the* **urban** *aerosol model with* **80% humidity** *but* **no precipitation** *as a function of temperature (°C) and meteorological visibility (km).*

B.1.2 Urban aerosol model

Tables B.9-B.16 list the atmospheric extinction coefficient, γ, in the MWIR frequency band assuming the urban aerosol model according to the atmospheric attenuation model described in section A.

		Visibility (km)								
		0.20	0.50	1.00	2.00	5.00	10.00	20.00	40.00	80.00
Temperature (°C)	-30	20.8	9.35	0.73	0.29	0.11	0.058	0.029	0.015	$7.9 \cdot 10^{-3}$
	-20	20.8	9.35	0.73	0.29	0.12	0.060	0.031	0.017	$9.6 \cdot 10^{-3}$
	-10	20.8	9.36	0.74	0.29	0.12	0.065	0.036	0.022	0.015
	0	20.8	9.37	0.75	0.31	0.14	0.081	0.053	0.038	0.031
	10	20.9	9.41	0.79	0.35	0.18	0.12	0.091	0.077	0.070
	20	21.0	9.50	0.88	0.44	0.27	0.21	0.18	0.17	0.16
	30	21.2	9.70	1.09	0.64	0.47	0.41	0.38	0.37	0.36

Table B.11 Extinction coefficient (1/km) in the **MWIR** *band assuming the* **urban** *aerosol model with* **90% humidity** *but* **no precipitation** *as a function of temperature (°C) and meteorological visibility (km).*

		Visibility (km)								
		0.20	0.50	1.00	2.00	5.00	10.00	20.00	40.00	80.00
Temperature (°C)	-30	20.8	9.35	0.73	0.33	0.13	0.067	0.034	0.017	$9.1 \cdot 10^{-3}$
	-20	20.8	9.35	0.73	0.33	0.14	0.069	0.036	0.019	0.011
	-10	20.8	9.36	0.74	0.34	0.14	0.075	0.042	0.025	0.017
	0	20.8	9.38	0.76	0.36	0.16	0.093	0.060	0.043	0.035
	10	20.9	9.42	0.80	0.40	0.20	0.13	0.10	0.085	0.077
	20	21.0	9.52	0.90	0.50	0.30	0.24	0.20	0.19	0.18
	30	21.2	9.74	1.12	0.73	0.53	0.46	0.43	0.41	0.40

Table B.12 Extinction coefficient (1/km) in the **MWIR** *band assuming the* **urban** *aerosol model with* **95% humidity** *but* **no precipitation** *as a function of temperature (°C) and meteorological visibility (km).*

T (°C)	p (mm/hr)	Visibility (km)				
		0.50	1.00	2.00	5.00	10.00
0	0.2	9.38	0.80	0.35	0.19	0.13
	1.0	9.43	0.98	0.55	0.39	0.33
	4.0	9.63	1.53	1.16	-	-
	8.0	9.81	1.84	1.50	-	-
10	0.2	9.39	0.81	0.37	0.20	0.15
	1.0	9.45	0.99	0.56	0.40	0.34
	4.0	9.65	1.54	1.17	-	-
	8.0	9.82	1.85	1.51	-	-
20	0.2	9.42	0.84	0.40	0.23	0.18
	1.0	9.48	1.02	0.60	0.43	0.38
	4.0	9.68	1.57	1.20	-	-
	8.0	9.85	1.89	1.54	-	-
30	0.2	9.49	0.91	0.47	0.30	0.25
	1.0	9.55	1.09	0.66	0.50	0.44
	4.0	9.75	1.64	1.27	-	-
	8.0	9.92	1.95	1.61	-	-

Table B.13 Extinction coefficient (1/km) in the **MWIR** *band assuming the* **urban** *aerosol model with* **50% humidity** *and rain as a function of temperature (°C), rain rate (mm/hr), and meteorological visibility (km).*

T (°C)	p (mm/hr)	Visibility (km)				
		0.50	1.00	2.00	5.00	10.00
0	0.2	9.39	0.81	0.37	0.20	0.14
	1.0	9.44	0.99	0.57	0.40	0.34
	4.0	9.64	1.54	1.17	-	-
	8.0	9.82	1.86	1.51	-	-
10	0.2	9.42	0.84	0.40	0.23	0.17
	1.0	9.48	1.02	0.60	0.43	0.37
	4.0	9.67	1.57	1.20	-	-
	8.0	9.85	1.89	1.54	-	-
20	0.2	9.49	0.91	0.47	0.30	0.25
	1.0	9.55	1.09	0.67	0.50	0.45
	4.0	9.75	1.65	1.28	-	-
	8.0	9.92	1.96	1.61	-	-
30	0.2	9.65	1.08	0.64	0.47	0.41
	1.0	9.71	1.26	0.83	0.66	0.61
	4.0	9.91	1.81	1.44	-	-
	8.0	10.08	2.12	1.78	-	-

Table B.14 Extinction coefficient (1/km) in the **MWIR** *band assuming the* **urban** *aerosol model with* **80% humidity** *and rain as a function of temperature (°C), rain rate (mm/hr), and meteorological visibility (km).*

T (°C)	p (mm/hr)	Visibility (km)				
		0.50	1.00	2.00	5.00	10.00
0	0.2	9.39	0.81	0.38	0.20	0.15
	1.0	9.45	0.99	0.57	0.40	0.35
	4.0	9.65	1.55	1.18	-	-
	8.0	9.82	1.86	1.52	-	-
10	0.2	9.43	0.85	0.41	0.24	0.19
	1.0	9.49	1.03	0.61	0.44	0.38
	4.0	9.69	1.58	1.22	-	-
	8.0	9.86	1.90	1.55	-	-
20	0.2	9.52	0.94	0.50	0.33	0.28
	1.0	9.58	1.12	0.70	0.53	0.47
	4.0	9.78	1.68	1.31	-	-
	8.0	9.95	1.99	1.64	-	-
30	0.2	9.72	1.15	0.71	0.54	0.48
	1.0	9.78	1.33	0.91	0.73	0.68
	4.0	9.98	1.88	1.51	-	-
	8.0	10.15	2.19	1.85	-	-

Table B.15 Extinction coefficient (1/km) in the **MWIR** *band assuming the* **urban** *aerosol model with* **90% humidity** *and rain as a function of temperature (°C), rain rate (mm/hr), and meteorological visibility (km).*

ϕ (%)	p (mm/hr)	Visibility (km)			
		0.50	1.00	2.00	4.00
50	0.1	9.52	1.30	0.91	0.77
	0.3	9.59	1.70	1.37	-
	1.0	7.23	2.55	-	-
	3.0	4.68	-	-	-
90	0.1	9.52	1.30	0.92	0.78
	0.3	9.59	1.71	1.38	-
	1.0	7.23	2.56	-	-
	3.0	4.69	-	-	-

Table B.16 Extinction coefficient (1/km) in the **MWIR** *band assuming the* **urban** *aerosol model as a function of relative humidity (%), snow rate (mm/hr), and meteorological visibility (km). Calculations made at reference temperature -10°C.*

		Visibility (km)								
		0.20	0.50	1.00	2.00	5.00	10.00	20.00	40.00	80.00
Temperature (°C)	-30	20.8	9.35	2.73	0.61	0.24	0.12	0.061	0.031	0.016
	-20	20.8	9.35	2.73	0.61	0.24	0.12	0.061	0.031	0.016
	-10	20.8	9.35	2.73	0.61	0.25	0.12	0.064	0.034	0.019
	0	20.8	9.36	2.74	0.62	0.25	0.13	0.070	0.040	0.025
	10	20.8	9.37	2.75	0.63	0.27	0.14	0.084	0.054	0.039
	20	20.9	9.40	2.78	0.66	0.30	0.18	0.12	0.085	0.070
	30	20.9	9.47	2.85	0.73	0.37	0.24	0.18	0.15	0.14

Table B.17 Extinction coefficient (1/km) in the **MWIR** *band assuming the* **maritime** *aerosol model with* **50% humidity** *but* **no precipitation** *as a function of temperature (°C) and meteorological visibility (km).*

		Visibility (km)								
		0.20	0.50	1.00	2.00	5.00	10.00	20.00	40.00	80.00
Temperature (°C)	-30	20.8	9.35	2.73	1.12	0.45	0.22	0.11	0.056	0.029
	-20	20.8	9.35	2.73	1.12	0.45	0.23	0.11	0.058	0.030
	-10	20.8	9.36	2.73	1.12	0.45	0.23	0.12	0.062	0.034
	0	20.8	9.37	2.75	1.13	0.47	0.24	0.13	0.076	0.048
	10	20.9	9.40	2.78	1.17	0.50	0.27	0.16	0.11	0.079
	20	20.9	9.47	2.85	1.24	0.57	0.35	0.24	0.18	0.15
	30	21.1	9.64	3.01	1.40	0.73	0.51	0.40	0.34	0.31

Table B.18 Extinction coefficient (1/km) in the **MWIR** *band assuming the* **maritime** *aerosol model with* **80% humidity** *but* **no precipitation** *as a function of temperature (°C) and meteorological visibility (km).*

B.1.3 Maritime aerosol model

Tables B.17-B.24 list the atmospheric extinction coefficient, γ, in the MWIR frequency band assuming the maritime aerosol model according to the atmospheric attenuation model described in section A.

		Visibility (km)								
		0.20	0.50	1.00	2.00	5.00	10.00	20.00	40.00	80.00
Temperature (°C)	-30	20.8	9.35	2.73	1.21	0.48	0.24	0.12	0.061	0.031
	-20	20.8	9.35	2.73	1.21	0.49	0.24	0.12	0.063	0.033
	-10	20.8	9.36	2.74	1.22	0.49	0.25	0.13	0.068	0.038
	0	20.8	9.37	2.75	1.23	0.51	0.27	0.14	0.085	0.054
	10	20.9	9.41	2.79	1.27	0.55	0.30	0.18	0.12	0.093
	20	21.0	9.50	2.88	1.36	0.64	0.39	0.27	0.21	0.18
	30	21.2	9.70	3.08	1.56	0.84	0.60	0.48	0.42	0.39

Table B.19 Extinction coefficient (1/km) in the **MWIR** *band assuming the* **maritime** *aerosol model with* **90%** **humidity** *but* **no precipitation** *as a function of temperature (°C) and meteorological visibility (km).*

		Visibility (km)								
		0.20	0.50	1.00	2.00	5.00	10.00	20.00	40.00	80.00
Temperature (°C)	-30	20.8	9.35	2.73	1.37	0.55	0.28	0.14	0.069	0.035
	-20	20.8	9.35	2.73	1.38	0.55	0.28	0.14	0.071	0.037
	-10	20.8	9.36	2.74	1.38	0.56	0.28	0.15	0.077	0.043
	0	20.8	9.38	2.75	1.40	0.58	0.30	0.16	0.095	0.061
	10	20.9	9.42	2.80	1.44	0.62	0.34	0.21	0.14	0.10
	20	21.0	9.52	2.90	1.54	0.72	0.44	0.31	0.24	0.20
	30	21.2	9.74	3.12	1.77	0.94	0.67	0.53	0.46	0.43

Table B.20 Extinction coefficient (1/km) in the **MWIR** *band assuming the* **maritime** *aerosol model with* **95%** **humidity** *but* **no precipitation** *as a function of temperature (°C) and meteorological visibility (km).*

T (°C)	p (mm/hr)	Visibility (km)				
		0.50	1.00	2.00	5.00	10.00
0	0.2	9.38	2.73	0.67	0.31	0.18
	1.0	9.43	2.72	0.83	0.47	0.35
	4.0	9.63	2.72	1.33	-	-
	8.0	9.81	2.81	1.62	-	-
10	0.2	9.39	2.74	0.68	0.32	0.20
	1.0	9.45	2.74	0.84	0.48	0.36
	4.0	9.65	2.73	1.34	-	-
	8.0	9.82	2.82	1.64	-	-
20	0.2	9.42	2.78	0.71	0.35	0.23
	1.0	9.48	2.77	0.88	0.51	0.39
	4.0	9.68	2.76	1.38	-	-
	8.0	9.85	2.85	1.67	-	-
30	0.2	9.49	2.84	0.78	0.42	0.30
	1.0	9.55	2.84	0.94	0.58	0.46
	4.0	9.75	2.83	1.44	-	-
	8.0	9.92	2.92	1.74	-	-

Table B.21 *Extinction coefficient (1/km) in the* **MWIR** *band assuming the* **maritime** *aerosol model with* **50% humidity** *and rain as a function of temperature (°C), rain rate (mm/hr), and meteorological visibility (km).*

T (°C)	p (mm/hr)	Visibility (km)				
		0.50	1.00	2.00	5.00	10.00
0	0.2	9.39	2.76	1.17	0.50	0.28
	1.0	9.44	2.81	1.27	0.60	0.38
	4.0	9.64	2.97	1.60	-	-
	8.0	9.82	3.13	1.83	-	-
10	0.2	9.42	2.79	1.20	0.53	0.31
	1.0	9.48	2.84	1.30	0.63	0.41
	4.0	9.67	3.00	1.63	-	-
	8.0	9.85	3.16	1.86	-	-
20	0.2	9.49	2.87	1.27	0.60	0.38
	1.0	9.55	2.91	1.38	0.71	0.48
	4.0	9.75	3.08	1.71	-	-
	8.0	9.92	3.24	1.93	-	-
30	0.2	9.65	3.03	1.43	0.77	0.54
	1.0	9.71	3.08	1.54	0.87	0.65
	4.0	9.91	3.24	1.87	-	-
	8.0	10.08	3.40	2.09	-	-

Table B.22 *Extinction coefficient (1/km) in the* **MWIR** *band assuming the* **maritime** *aerosol model with* **80% humidity** *and rain as a function of temperature (°C), rain rate (mm/hr), and meteorological visibility (km).*

T (°C)	p (mm/hr)	Visibility (km)				
		0.50	1.00	2.00	5.00	10.00
0	0.2	9.39	2.77	1.26	0.54	0.30
	1.0	9.45	2.83	1.36	0.63	0.39
	4.0	9.65	3.02	1.65	-	-
	8.0	9.82	3.19	1.87	-	-
10	0.2	9.43	2.81	1.30	0.58	0.33
	1.0	9.49	2.87	1.39	0.67	0.43
	4.0	9.69	3.06	1.69	-	-
	8.0	9.86	3.23	1.91	-	-
20	0.2	9.52	2.90	1.39	0.67	0.42
	1.0	9.58	2.96	1.48	0.76	0.52
	4.0	9.78	3.15	1.78	-	-
	8.0	9.95	3.32	2.00	-	-
30	0.2	9.72	3.10	1.59	0.87	0.63
	1.0	9.78	3.16	1.69	0.96	0.72
	4.0	9.98	3.35	1.99	-	-
	8.0	10.15	3.53	2.20	-	-

Table B.23 Extinction coefficient (1/km) in the **MWIR** *band assuming the* **maritime** *aerosol model with* **90% humidity** *and rain as a function of temperature (°C), rain rate (mm/hr), and meteorological visibility (km).*

ϕ (%)	p (mm/hr)	Visibility (km)			
		0.50	1.00	2.00	4.00
50	0.1	9.52	2.67	1.12	0.81
	0.3	9.60	2.58	1.48	-
	1.0	8.13	2.79	-	-
	3.0	6.21	-	-	-
90	0.1	9.52	2.90	1.50	0.89
	0.3	9.60	2.99	1.68	-
	1.0	8.14	3.23	-	-
	3.0	6.39	-	-	-

Table B.24 Extinction coefficient (1/km) in the **MWIR** *band assuming the* **maritime** *aerosol model as a function of relative humidity (%), snow rate (mm/hr), and meteorological visibility (km). Calculations made at reference temperature* $-10°C$.

		Visibility (km)								
		0.20	0.50	1.00	2.00	5.00	10.00	20.00	40.00	80.00
Temperature (°C)	-10	20.42	8.17	4.09	2.04	0.79	0.38	0.17	0.065	0.014
	0	20.42	8.17	4.09	2.04	0.79	0.38	0.17	0.066	0.016
	10	20.43	8.17	4.09	2.05	0.80	0.38	0.17	0.070	0.019
	20	20.43	8.18	4.10	2.06	0.81	0.39	0.18	0.077	0.026
	30	20.45	8.20	4.11	2.07	0.82	0.40	0.19	0.091	0.040
	40	20.48	8.22	4.14	2.10	0.85	0.43	0.22	0.12	0.068
	50	20.53	8.27	4.19	2.15	0.90	0.48	0.27	0.17	0.12

Table B.25 *Extinction coefficient (1/km) in the* **MWIR** *band assuming the* **desert** *aerosol model with* **20% humidity** *as a function of temperature (°C) and meteorological visibility (km).*

B.1.4 Desert aerosol model

Table B.25 lists the atmospheric extinction coefficient, γ, in the MWIR frequency band assuming the desert aerosol model according to the atmospheric attenuation model described in section A.

		Visibility (km)								
		0.20	0.50	1.00	2.00	5.00	10.00	20.00	40.00	80.00
Temperature (°C)	-30	20.8	4.25	0.45	0.17	0.069	0.035	0.017	$8.8 \cdot 10^{-3}$	$4.5 \cdot 10^{-3}$
	-20	20.8	4.25	0.45	0.17	0.070	0.035	0.018	$9.4 \cdot 10^{-3}$	$5.1 \cdot 10^{-3}$
	-10	20.8	4.26	0.45	0.18	0.072	0.038	0.021	0.012	$7.7 \cdot 10^{-3}$
	0	20.8	4.27	0.46	0.19	0.082	0.048	0.031	0.022	0.018
	10	20.9	4.29	0.49	0.21	0.11	0.076	0.059	0.050	0.046
	20	20.9	4.37	0.57	0.29	0.19	0.15	0.14	0.13	0.12
	30	21.1	4.57	0.77	0.49	0.38	0.35	0.33	0.32	0.32

Table B.26 *Extinction coefficient (1/km) in the* **LWIR** *band assuming the* **rural** *aerosol model with* **50% humidity** *but* **no precipitation** *as a function of temperature (°C) and meteorological visibility (km).*

		Visibility (km)								
		0.20	0.50	1.00	2.00	5.00	10.00	20.00	40.00	80.00
Temperature (°C)	-30	20.8	4.25	0.45	0.17	0.069	0.035	0.018	$9.0 \cdot 10^{-3}$	$4.7 \cdot 10^{-3}$
	-20	20.8	4.25	0.45	0.17	0.070	0.036	0.019	0.010	$6.1 \cdot 10^{-3}$
	-10	20.8	4.26	0.46	0.18	0.077	0.042	0.025	0.016	0.012
	0	20.8	4.29	0.48	0.20	0.10	0.067	0.050	0.041	0.037
	10	20.9	4.36	0.55	0.28	0.17	0.14	0.12	0.11	0.11
	20	21.1	4.55	0.75	0.47	0.37	0.33	0.32	0.31	0.30
	30	21.6	5.05	1.25	0.97	0.87	0.83	0.81	0.81	0.80

Table B.27 *Extinction coefficient (1/km) in the* **LWIR** *band assuming the* **rural** *aerosol model with* **80% humidity** *but* **no precipitation** *as a function of temperature (°C) and meteorological visibility (km).*

B.2 LWIR ($8 - 12\mu$m)

This section lists the atmospheric extinction coefficient, γ, in the LWIR frequency band according to the atmospheric attenuation model described in section A sorted according to: (i) the aerosol model (ii) no precipitation/rainfall/snowfall (iii) air humidity.

B.2.1 Rural aerosol model

Tables B.26-B.33 list the atmospheric extinction coefficient, γ, in the LWIR frequency band assuming the rural aerosol model according to the atmospheric attenuation model described in section A.

		Visibility (km)								
		0.20	0.50	1.00	2.00	5.00	10.00	20.00	40.00	80.00
Temperature (°C)	-30	20.8	4.25	0.45	0.16	0.064	0.032	0.016	$8.5 \cdot 10^{-3}$	$4.5 \cdot 10^{-3}$
	-20	20.8	4.26	0.45	0.16	0.066	0.034	0.018	0.010	$6.2 \cdot 10^{-3}$
	-10	20.8	4.26	0.46	0.17	0.073	0.042	0.026	0.018	0.014
	0	20.8	4.29	0.49	0.20	0.10	0.073	0.057	0.049	0.045
	10	20.9	4.38	0.58	0.29	0.19	0.16	0.15	0.14	0.13
	20	21.2	4.63	0.83	0.54	0.44	0.41	0.39	0.39	0.38
	30	21.8	5.26	1.46	1.16	1.07	1.04	1.02	1.01	1.01

Table B.28 *Extinction coefficient (1/km) in the* **LWIR** *band assuming the* **rural** *aerosol model with* **90% humidity** *but* **no precipitation** *as a function of temperature (°C) and meteorological visibility (km).*

		Visibility (km)								
		0.20	0.50	1.00	2.00	5.00	10.00	20.00	40.00	80.00
Temperature (°C)	-30	20.8	4.25	0.45	0.15	0.062	0.031	0.016	$8.2 \cdot 10^{-3}$	$4.4 \cdot 10^{-3}$
	-20	20.8	4.26	0.45	0.16	0.064	0.033	0.018	0.010	$6.3 \cdot 10^{-3}$
	-10	20.8	4.26	0.46	0.16	0.072	0.041	0.026	0.019	0.015
	0	20.9	4.30	0.50	0.20	0.11	0.076	0.061	0.053	0.049
	10	21.0	4.40	0.60	0.30	0.21	0.18	0.16	0.15	0.15
	20	21.2	4.67	0.87	0.57	0.48	0.45	0.44	0.43	0.42
	30	21.9	5.37	1.57	1.27	1.18	1.15	1.13	1.13	1.12

Table B.29 *Extinction coefficient (1/km) in the* **LWIR** *band assuming the* **rural** *aerosol model with* **95% humidity** *but* **no precipitation** *as a function of temperature (°C) and meteorological visibility (km).*

T (°C)	p (mm/hr)	Visibility (km)				
		0.50	1.00	2.00	5.00	10.00
0	0.2	4.21	0.53	0.26	0.15	0.12
	1.0	4.08	0.76	0.50	0.40	0.36
	4.0	3.84	1.56	1.33	-	-
	8.0	3.82	1.96	1.75	-	-
10	0.2	4.23	0.56	0.28	0.18	0.15
	1.0	4.11	0.79	0.53	0.43	0.39
	4.0	3.86	1.59	1.36	-	-
	8.0	3.84	1.99	1.77	-	-
20	0.2	4.31	0.64	0.36	0.26	0.22
	1.0	4.19	0.87	0.61	0.50	0.47
	4.0	3.94	1.67	1.44	-	-
	8.0	3.92	2.07	1.85	-	-
30	0.2	4.51	0.83	0.56	0.45	0.42
	1.0	4.39	1.07	0.80	0.70	0.66
	4.0	4.14	1.86	1.63	-	-
	8.0	4.12	2.26	2.05	-	-

Table B.30 Extinction coefficient (1/km) in the **LWIR** *band assuming the* **rural** *aerosol model with* **50% humidity** *and rain as a function of temperature (°C), rain rate (mm/hr), and meteorological visibility (km).*

T (°C)	p (mm/hr)	Visibility (km)				
		0.50	1.00	2.00	5.00	10.00
0	0.2	4.23	0.55	0.27	0.17	0.14
	1.0	4.10	0.78	0.52	0.42	0.38
	4.0	3.85	1.58	1.35	-	-
	8.0	3.83	1.98	1.77	-	-
10	0.2	4.30	0.62	0.35	0.24	0.21
	1.0	4.17	0.85	0.59	0.49	0.45
	4.0	3.93	1.65	1.42	-	-
	8.0	3.91	2.05	1.84	-	-
20	0.2	4.49	0.82	0.54	0.44	0.40
	1.0	4.37	1.05	0.79	0.68	0.65
	4.0	4.12	1.85	1.62	-	-
	8.0	4.10	2.24	2.03	-	-
30	0.2	4.99	1.31	1.04	0.94	0.90
	1.0	4.87	1.55	1.28	1.18	1.15
	4.0	4.62	2.34	2.11	-	-
	8.0	4.60	2.74	2.53	-	-

Table B.31 Extinction coefficient (1/km) in the **LWIR** *band assuming the* **rural** *aerosol model with* **80% humidity** *and rain as a function of temperature (°C), rain rate (mm/hr), and meteorological visibility (km).*

T (°C)	p (mm/hr)	Visibility (km)				
		0.50	1.00	2.00	5.00	10.00
0	0.2	4.23	0.56	0.27	0.18	0.14
	1.0	4.11	0.79	0.52	0.42	0.39
	4.0	3.86	1.58	1.35	-	-
	8.0	3.84	1.98	1.77	-	-
10	0.2	4.32	0.65	0.36	0.26	0.23
	1.0	4.20	0.88	0.61	0.51	0.48
	4.0	3.95	1.67	1.44	-	-
	8.0	3.93	2.07	1.86	-	-
20	0.2	4.57	0.89	0.61	0.51	0.48
	1.0	4.45	1.13	0.85	0.76	0.73
	4.0	4.20	1.92	1.69	-	-
	8.0	4.18	2.32	2.11	-	-
30	0.2	5.20	1.52	1.24	1.14	1.11
	1.0	5.08	1.75	1.48	1.39	1.35
	4.0	4.83	2.55	2.32	-	-
	8.0	4.81	2.94	2.73	-	-

Table B.32 Extinction coefficient (1/km) in the **LWIR** *band assuming the* **rural** *aerosol model with* **90% humidity** *and rain as a function of temperature (°C, rain rate (mm/hr), and meteorological visibility (km).*

ϕ (%)	p (mm/hr)	Visibility (km)			
		0.50	1.00	2.00	4.00
50	0.1	4.21	1.59	1.35	1.26
	0.3	3.95	2.25	2.04	-
	1.0	4.58	3.43	-	-
	3.0	5.64	-	-	-
90	0.1	4.21	1.59	1.35	1.27
	0.3	3.95	2.24	2.04	-
	1.0	4.59	3.43	-	-
	3.0	5.64	-	-	-

Table B.33 Extinction coefficient (1/km) in the **LWIR** *band assuming the* **rural** *aerosol model as a function of relative humidity (%), snow rate (mm/hr), and meteorological visibility (km). Calculations made at reference temperature* $-10°C$*.*

		Visibility (km)								
		0.20	0.50	1.00	2.00	5.00	10.00	20.00	40.00	80.00
Temperature (°C)	-30	20.8	4.25	0.41	0.19	0.076	0.038	0.019	$9.7 \cdot 10^{-3}$	$4.9 \cdot 10^{-3}$
	-20	20.8	4.25	0.41	0.19	0.076	0.039	0.020	0.010	$5.6 \cdot 10^{-3}$
	-10	20.8	4.26	0.41	0.19	0.079	0.041	0.022	0.013	$8.1 \cdot 10^{-3}$
	0	20.8	4.27	0.42	0.20	0.089	0.051	0.032	0.023	0.018
	10	20.8	4.29	0.45	0.23	0.12	0.079	0.061	0.051	0.046
	20	20.9	4.37	0.53	0.31	0.19	0.16	0.14	0.13	0.12
	30	21.1	4.57	0.72	0.50	0.39	0.35	0.33	0.32	0.32

Table B.34 *Extinction coefficient (1/km) in the* **LWIR** *band assuming the* **urban** *aerosol model with* **50% humidity** *but* **no precipitation** *as a function of temperature (°C) and meteorological visibility (km).*

		Visibility (km)								
		0.20	0.50	1.00	2.00	5.00	10.00	20.00	40.00	80.00
Temperature (°C)	-30	20.8	4.25	0.41	0.18	0.071	0.036	0.018	$9.3 \cdot 10^{-3}$	$4.8 \cdot 10^{-3}$
	-20	20.8	4.25	0.41	0.18	0.073	0.037	0.019	0.011	$6.2 \cdot 10^{-3}$
	-10	20.8	4.26	0.41	0.18	0.079	0.043	0.026	0.017	0.012
	0	20.8	4.29	0.44	0.21	0.10	0.068	0.050	0.042	0.037
	10	20.9	4.36	0.51	0.28	0.17	0.14	0.12	0.11	0.11
	20	21.1	4.55	0.71	0.48	0.37	0.33	0.32	0.31	0.30
	30	21.6	5.05	1.20	0.97	0.87	0.83	0.81	0.81	0.80

Table B.35 *Extinction coefficient (1/km) in the* **LWIR** *band assuming the* **urban** *aerosol model with* **80% humidity** *but* **no precipitation** *as a function of temperature (°C) and meteorological visibility (km).*

B.2.2 Urban aerosol model

Tables B.34-B.41 list the atmospheric extinction coefficient, γ, in the LWIR frequency band assuming the urban aerosol model according to the atmospheric attenuation model described in section A.

		Visibility (km)								
		0.20	0.50	1.00	2.00	5.00	10.00	20.00	40.00	80.00
Temperature (°C)	-30	20.8	4.25	0.41	0.17	0.067	0.034	0.017	$8.7 \cdot 10^{-3}$	$4.6 \cdot 10^{-3}$
	-20	20.8	4.26	0.41	0.17	0.068	0.035	0.019	0.010	$6.4 \cdot 10^{-3}$
	-10	20.8	4.26	0.42	0.17	0.076	0.043	0.026	0.018	0.014
	0	20.9	4.29	0.45	0.21	0.11	0.074	0.057	0.049	0.045
	10	20.9	4.38	0.54	0.30	0.20	0.16	0.15	0.14	0.13
	20	21.2	4.63	0.78	0.54	0.44	0.41	0.39	0.39	0.38
	30	21.8	5.26	1.41	1.17	1.07	1.04	1.02	1.01	1.01

Table B.36 Extinction coefficient (1/km) in the **LWIR** *band assuming the* **urban** *aerosol model with* **90% humidity** *but* **no precipitation** *as a function of temperature (°C) and meteorological visibility (km).*

		Visibility (km)								
		0.20	0.50	1.00	2.00	5.00	10.00	20.00	40.00	80.00
Temperature (°C)	-30	20.8	4.25	0.41	0.19	0.076	0.038	0.019	$9.9 \cdot 10^{-3}$	$5.2 \cdot 10^{-3}$
	-20	20.8	4.26	0.41	0.19	0.078	0.040	0.021	0.012	$7.1 \cdot 10^{-3}$
	-10	20.8	4.26	0.42	0.20	0.086	0.048	0.030	0.020	0.016
	0	20.9	4.30	0.45	0.23	0.12	0.083	0.064	0.055	0.050
	10	21.0	4.40	0.55	0.33	0.22	0.18	0.16	0.15	0.15
	20	21.2	4.67	0.83	0.61	0.50	0.46	0.44	0.43	0.42
	30	21.9	5.37	1.53	1.31	1.19	1.16	1.14	1.13	1.12

Table B.37 Extinction coefficient (1/km) in the **LWIR** *band assuming the* **urban** *aerosol model with* **95% humidity** *but* **no precipitation** *as a function of temperature (°C) and meteorological visibility (km).*

T (°C)	p (mm/hr)	Visibility (km)				
		0.50	1.00	2.00	5.00	10.00
0	0.2	4.21	0.49	0.27	0.16	0.12
	1.0	4.08	0.73	0.52	0.40	0.36
	4.0	3.84	1.54	1.34	-	-
	8.0	3.82	1.95	1.75	-	-
10	0.2	4.23	0.52	0.30	0.19	0.15
	1.0	4.11	0.76	0.54	0.43	0.39
	4.0	3.86	1.57	1.37	-	-
	8.0	3.84	1.98	1.78	-	-
20	0.2	4.31	0.59	0.38	0.26	0.23
	1.0	4.19	0.83	0.62	0.51	0.47
	4.0	3.94	1.65	1.45	-	-
	8.0	3.92	2.06	1.86	-	-
30	0.2	4.51	0.79	0.57	0.46	0.42
	1.0	4.39	1.03	0.82	0.70	0.67
	4.0	4.14	1.85	1.64	-	-
	8.0	4.12	2.25	2.05	-	-

Table B.38 Extinction coefficient (1/km) in the **LWIR** *band assuming the* **urban** *aerosol model with* **50% humidity** *and rain as a function of temperature (°C), rain rate (mm/hr), and meteorological visibility (km).*

T (°C)	p (mm/hr)	Visibility (km)				
		0.50	1.00	2.00	5.00	10.00
0	0.2	4.23	0.51	0.28	0.17	0.14
	1.0	4.10	0.75	0.52	0.42	0.38
	4.0	3.85	1.56	1.35	-	-
	8.0	3.83	1.96	1.77	-	-
10	0.2	4.30	0.58	0.35	0.24	0.21
	1.0	4.17	0.82	0.59	0.49	0.45
	4.0	3.93	1.63	1.42	-	-
	8.0	3.91	2.04	1.84	-	-
20	0.2	4.49	0.77	0.55	0.44	0.40
	1.0	4.37	1.01	0.79	0.68	0.65
	4.0	4.12	1.82	1.62	-	-
	8.0	4.10	2.23	2.03	-	-
30	0.2	4.99	1.27	1.04	0.94	0.90
	1.0	4.87	1.51	1.29	1.18	1.15
	4.0	4.62	2.32	2.12	-	-
	8.0	4.60	2.73	2.53	-	-

Table B.39 Extinction coefficient (1/km) in the **LWIR** *band assuming the* **urban** *aerosol model with* **80% humidity** *and rain as a function of temperature (°C), rain rate (mm/hr), and meteorological visibility (km).*

T (°C)	p (mm/hr)	Visibility (km)				
		0.50	1.00	2.00	5.00	10.00
0	0.2	4.23	0.52	0.28	0.18	0.14
	1.0	4.11	0.75	0.52	0.42	0.39
	4.0	3.86	1.56	1.36	-	-
	8.0	3.84	1.97	1.77	-	-
10	0.2	4.32	0.60	0.37	0.27	0.23
	1.0	4.20	0.84	0.61	0.51	0.48
	4.0	3.95	1.65	1.45	-	-
	8.0	3.93	2.05	1.86	-	-
20	0.2	4.57	0.85	0.61	0.51	0.48
	1.0	4.45	1.09	0.86	0.76	0.73
	4.0	4.20	1.90	1.69	-	-
	8.0	4.18	2.30	2.11	-	-
30	0.2	5.20	1.48	1.24	1.14	1.11
	1.0	5.08	1.72	1.49	1.39	1.35
	4.0	4.83	2.53	2.32	-	-
	8.0	4.81	2.93	2.74	-	-

Table B.40 Extinction coefficient (1/km) in the **LWIR** *band assuming the* **urban** *aerosol model with* **90% humidity** *and rain as a function of temperature (°C), rain rate (mm/hr), and meteorological visibility (km).*

ϕ (%)	p (mm/hr)	Visibility (km)			
		0.50	1.00	2.00	4.00
50	0.1	4.21	1.57	1.36	1.27
	0.3	3.95	2.24	2.04	-
	1.0	4.56	3.44	-	-
	3.0	5.61	-	-	-
90	0.1	4.22	1.57	1.35	1.27
	0.3	3.95	2.23	2.04	-
	1.0	4.57	3.43	-	-
	3.0	5.61	-	-	-

Table B.41 Extinction coefficient (1/km) in the **LWIR** *band assuming the* **urban** *aerosol model as a function of relative humidity (%), snow rate (mm/hr), and meteorological visibility (km). Calculations made at reference temperature* $-10°$*C.*

		Visibility (km)								
		0.20	0.50	1.00	2.00	5.00	10.00	20.00	40.00	80.00
Temperature (°C)	-30	20.8	4.25	1.11	0.21	0.084	0.042	0.021	0.011	$5.5 \cdot 10^{-3}$
	-20	20.8	4.25	1.11	0.21	0.085	0.043	0.022	0.011	$6.1 \cdot 10^{-3}$
	-10	20.8	4.26	1.11	0.21	0.087	0.045	0.024	0.014	$8.6 \cdot 10^{-3}$
	0	20.8	4.27	1.12	0.22	0.098	0.055	0.034	0.024	0.019
	10	20.9	4.29	1.15	0.25	0.13	0.084	0.063	0.052	0.047
	20	20.9	4.37	1.23	0.33	0.20	0.16	0.14	0.13	0.12
	30	21.1	4.57	1.42	0.53	0.40	0.36	0.34	0.33	0.32

Table B.42 Extinction coefficient (1/km) in the **LWIR** *band assuming the* **maritime** *aerosol model with* **50% humidity** *but* **no precipitation** *as a function of temperature (°C) and meteorological visibility (km).*

		Visibility (km)								
		0.20	0.50	1.00	2.00	5.00	10.00	20.00	40.00	80.00
Temperature (°C)	-30	20.8	4.25	1.11	0.39	0.16	0.079	0.040	0.020	0.010
	-20	20.8	4.25	1.11	0.40	0.16	0.081	0.041	0.022	0.012
	-10	20.8	4.26	1.11	0.40	0.17	0.087	0.047	0.028	0.018
	0	20.8	4.29	1.14	0.43	0.19	0.11	0.072	0.052	0.043
	10	20.9	4.36	1.21	0.50	0.26	0.18	0.14	0.12	0.11
	20	21.1	4.55	1.41	0.69	0.46	0.38	0.34	0.32	0.31
	30	21.6	5.05	1.90	1.19	0.95	0.88	0.84	0.82	0.81

Table B.43 Extinction coefficient (1/km) in the **LWIR** *band assuming the* **maritime** *aerosol model with* **80% humidity** *but* **no precipitation** *as a function of temperature (°C) and meteorological visibility (km).*

B.2.3 Maritime aerosol model

Tables B.42-B.49 list the atmospheric extinction coefficient, γ, in the LWIR frequency band assuming the maritime aerosol model according to the atmospheric attenuation model described in section A.

		Visibility (km)								
		0.20	0.50	1.00	2.00	5.00	10.00	20.00	40.00	80.00
Temperature (°C)	-30	20.8	4.25	1.11	0.45	0.18	0.091	0.046	0.023	0.012
	-20	20.8	4.26	1.11	0.45	0.18	0.092	0.047	0.025	0.013
	-10	20.8	4.26	1.12	0.46	0.19	0.10	0.055	0.032	0.021
	0	20.9	4.29	1.15	0.49	0.22	0.13	0.086	0.064	0.052
	10	20.9	4.38	1.24	0.58	0.31	0.22	0.18	0.15	0.14
	20	21.2	4.63	1.48	0.83	0.56	0.47	0.42	0.40	0.39
	30	21.8	5.26	2.11	1.46	1.19	1.10	1.05	1.03	1.02

Table B.44 Extinction coefficient (1/km) in the **LWIR** *band assuming the* **maritime** *aerosol model with* **90% humidity** *but* **no precipitation** *as a function of temperature (°C) and meteorological visibility (km).*

		Visibility (km)								
		0.20	0.50	1.00	2.00	5.00	10.00	20.00	40.00	80.00
Temperature (°C)	-30	20.8	4.25	1.11	0.56	0.22	0.11	0.056	0.028	0.014
	-20	20.8	4.26	1.11	0.56	0.23	0.11	0.058	0.030	0.016
	-10	20.8	4.26	1.12	0.57	0.23	0.12	0.067	0.039	0.025
	0	20.9	4.30	1.15	0.60	0.27	0.16	0.10	0.073	0.059
	10	21.0	4.40	1.25	0.70	0.37	0.26	0.20	0.17	0.16
	20	21.2	4.67	1.53	0.98	0.64	0.53	0.48	0.45	0.43
	30	21.9	5.37	2.22	1.68	1.34	1.23	1.17	1.15	1.13

Table B.45 Extinction coefficient (1/km) in the **LWIR** *band assuming the* **maritime** *aerosol model with* **95% humidity** *but* **no precipitation** *as a function of temperature (°C) and meteorological visibility (km).*

T (°C)	p (mm/hr)	Visibility (km)				
		0.50	1.00	2.00	5.00	10.00
0	0.2	4.21	1.16	0.29	0.17	0.12
	1.0	4.08	1.32	0.53	0.41	0.36
	4.0	3.84	1.91	1.35	-	-
	8.0	3.82	2.23	1.76	-	-
10	0.2	4.23	1.19	0.32	0.19	0.15
	1.0	4.11	1.35	0.56	0.44	0.39
	4.0	3.86	1.94	1.38	-	-
	8.0	3.84	2.26	1.79	-	-
20	0.2	4.31	1.27	0.40	0.27	0.23
	1.0	4.19	1.43	0.64	0.51	0.47
	4.0	3.94	2.02	1.46	-	-
	8.0	3.92	2.34	1.87	-	-
30	0.2	4.51	1.46	0.59	0.47	0.43
	1.0	4.39	1.63	0.83	0.71	0.67
	4.0	4.14	2.22	1.65	-	-
	8.0	4.12	2.53	2.06	-	-

Table B.46 Extinction coefficient (1/km) in the **LWIR** *band assuming the* **maritime** *aerosol model with* **50% humidity** *and rain as a function of temperature (°C), rain rate (mm/hr), and meteorological visibility (km).*

T (°C)	p (mm/hr)	Visibility (km)				
		0.50	1.00	2.00	5.00	10.00
0	0.2	4.23	1.19	0.49	0.25	0.17
	1.0	4.10	1.37	0.71	0.47	0.39
	4.0	3.85	2.02	1.47	-	-
	8.0	3.83	2.36	1.85	-	-
10	0.2	4.30	1.26	0.56	0.32	0.24
	1.0	4.17	1.44	0.78	0.54	0.46
	4.0	3.93	2.09	1.54	-	-
	8.0	3.91	2.44	1.92	-	-
20	0.2	4.49	1.45	0.75	0.52	0.44
	1.0	4.37	1.64	0.97	0.74	0.66
	4.0	4.12	2.29	1.73	-	-
	8.0	4.10	2.63	2.12	-	-
30	0.2	4.99	1.95	1.25	1.02	0.94
	1.0	4.87	2.14	1.47	1.24	1.16
	4.0	4.62	2.79	2.23	-	-
	8.0	4.60	3.13	2.61	-	-

Table B.47 Extinction coefficient (1/km) in the **LWIR** *band assuming the* **maritime** *aerosol model with* **80% humidity** *and rain as a function of temperature (°C), rain rate (mm/hr), and meteorological visibility (km).*

T (°C)	p (mm/hr)	Visibility (km)				
		0.50	1.00	2.00	5.00	10.00
0	0.2	4.23	1.20	0.55	0.28	0.19
	1.0	4.11	1.39	0.76	0.49	0.40
	4.0	3.86	2.06	1.50	-	-
	8.0	3.84	2.41	1.88	-	-
10	0.2	4.32	1.29	0.64	0.37	0.28
	1.0	4.20	1.48	0.85	0.58	0.49
	4.0	3.95	2.15	1.59	-	-
	8.0	3.93	2.50	1.97	-	-
20	0.2	4.57	1.53	0.89	0.62	0.53
	1.0	4.45	1.72	1.10	0.83	0.74
	4.0	4.20	2.40	1.84	-	-
	8.0	4.18	2.74	2.22	-	-
30	0.2	5.20	2.16	1.51	1.24	1.15
	1.0	5.08	2.35	1.73	1.46	1.37
	4.0	4.83	3.02	2.47	-	-
	8.0	4.81	3.37	2.84	-	-

Table B.48 Extinction coefficient (1/km) in the **LWIR** *band assuming the* **maritime** *aerosol model with* **90% humidity** *and rain as a function of temperature (°C), rain rate (mm/hr), and meteorological visibility (km).*

ϕ (%)	p (mm/hr)	Visibility (km)			
		0.50	1.00	2.00	4.00
50	0.1	4.21	2.01	1.37	1.27
	0.3	3.95	2.49	2.05	-
	1.0	4.88	3.46	-	-
	3.0	6.12	-	-	-
90	0.1	4.22	2.11	1.53	1.31
	0.3	3.96	2.65	2.14	-
	1.0	4.89	3.64	-	-
	3.0	6.20	-	-	-

Table B.49 Extinction coefficient (1/km) in the **LWIR** *band assuming the* **maritime** *aerosol model as a function of relative humidity (%), snow rate (mm/hr), and meteorological visibility (km). Calculations made at reference temperature* $-10°$*C.*

		Visibility (km)								
		0.20	0.50	1.00	2.00	5.00	10.00	20.00	40.00	80.00
Temperature (°C)	-10	21.78	8.71	4.36	2.18	0.85	0.40	0.18	0.068	0.014
	0	21.78	8.71	4.36	2.18	0.85	0.40	0.18	0.069	0.016
	10	21.79	8.72	4.36	2.19	0.85	0.41	0.19	0.074	0.021
	20	21.80	8.73	4.38	2.20	0.87	0.42	0.20	0.087	0.034
	30	21.83	8.77	4.41	2.23	0.90	0.45	0.23	0.12	0.066
	40	21.91	8.84	4.48	2.31	0.97	0.53	0.31	0.19	0.14
	50	22.07	9.00	4.64	2.47	1.13	0.69	0.47	0.36	0.30

Table B.50 Extinction coefficient (1/km) in the **LWIR** *band assuming the* **desert** *aerosol model with* **20% humidity** *as a function of temperature (°C) and meteorological visibility (km).*

B.2.4 Desert aerosol model

Table B.50 lists the atmospheric extinction coefficient, γ, in the LWIR frequency band assuming the desert aerosol model according to the atmospheric attenuation model described in section A.

About FFI

The Norwegian Defence Research Establishment (FFI) was founded 11th of April 1946. It is organised as an administrative agency subordinate to the Ministry of Defence.

FFI's mission

FFI is the prime institution responsible for defence related research in Norway. Its principal mission is to carry out research and development to meet the requirements of the Armed Forces. FFI has the role of chief adviser to the political and military leadership. In particular, the institute shall focus on aspects of the development in science and technology that can influence our security policy or defence planning.

FFI's vision

FFI turns knowledge and ideas into an efficient defence.

FFI's characteristics

Creative, daring, broad-minded and responsible.

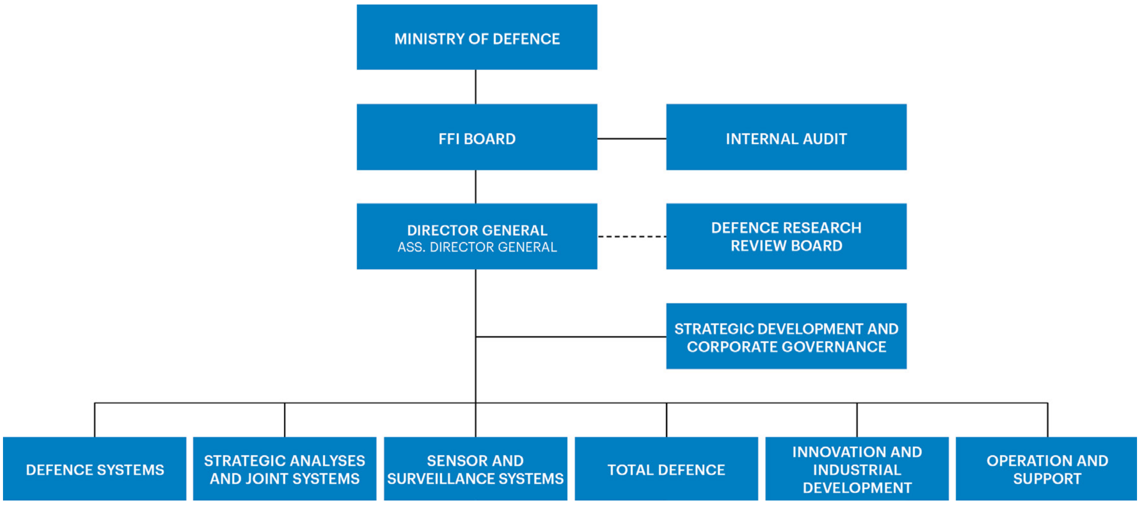

Forsvarets forskningsinstitutt
Postboks 25
2027 Kjeller

Besøksadresse:
Instituttveien 20
2007 Kjeller

Telefon: 63 80 70 00
Telefaks: 63 80 71 15
Epost: post@ffi.no

Norwegian Defence Research Establishment (FFI)
P.O. Box 25
NO-2027 Kjeller

Office address:
Instituttveien 20
N-2007 Kjeller

Telephone: +47 63 80 70 00
Telefax: +47 63 80 71 15
Email: post@ffi.no